1-1-2012

Developing High-Density Diffuse Optical Tomography for Neuroimaging

Brian White

Washington University in St. Louis

Recommended Citation

White, Brian, "Developing High-Density Diffuse Optical Tomography for Neuroimaging" (2012). *All Theses and Dissertations (ETDs)*. 665.
https://openscholarship.wustl.edu/etd/665

WASHINGTON UNIVERSITY IN ST. LOUIS

Department of Physics

Dissertation Examination Committee:
Joseph P. Culver, Chair
Mark S. Conradi
Timothy E. Holy
James G. Miller
Bradley L. Schlaggar
Ralf Wessel

Developing High-Density Diffuse Optical Tomography for Neuroimaging

by

Brian Richard White

A dissertation presented to the
Graduate School of Arts and Sciences
of Washington University in
partial fulfillment of the
requirements for the degree
of Doctor of Philosophy

May 2012
Saint Louis, Missouri

Abstract of the Dissertation

Developing High-Density Diffuse Optical Tomography for Neuroimaging

by

Brian Richard White

Doctor of Philosophy in Physics

Washington University in St. Louis, 2012

Professor Joseph P. Culver, Chairperson

Clinicians who care for brain-injured patients and premature infants desire a bedside monitor of brain function. A decade ago, there was hope that optical imaging would be able to fill this role, as it combined fMRI's ability to construct cortical maps with EEG's portable, cap-based systems. However, early optical systems had poor imaging performance, and the momentum for the technique slowed. In our lab, we develop diffuse optical tomography (DOT), which is a more advanced method of performing optical imaging. My research has been to pioneer the *in vivo* use of DOT for advanced neuroimaging by (1) quantifying the advantages of DOT through both *in silico* simulation and *in vivo* performance metrics, (2) restoring confidence in the technique with the first retinotopic mapping of the visual cortex (a benchmark for fMRI and PET), and (3) creating concepts and methods for the clinical translation of DOT. Hospitalized patients are unable to perform complicated neurological tasks, which has motivated us to develop the first DOT methods for resting-state brain mapping with functional connectivity. Finally, in collaboration with neonatologists, I have extended these methods with proof-of-principle imaging of brain-injured premature infants. This work establishes DOT's improvements in imaging performance and readies it for multiple clinical and research roles.

Acknowledgements

I would to thank the support (moral and financial) of the Medical Scientist Training Program and it's administrators, past and present. This work was also financially supported by the Imaging Sciences Fellowship. My progress has been possible due to the guidance of Joe Culver as well as lessons learned from Howard Stone and Johannes de Boer. Thank you to Ben Zeff for building an amazing system that I have been able to show off. And thank you to the many others that helped bring these projects to fruition, especially Nick Gregg, Steve Liao, and Silvina Ferradal with BabyDOT, Avi Snyder with fcDOT, Adam Bauer with fcOIS, and Marty Olevitch and Hamid Dehghani with software. And, of course, many thanks are due to family and friends for their extensive support.

Contents

List of Figures

List of Tables

Chapter 1

Introduction

Improvements in critical care medicine have allowed many more patients to survive than in years past. Physicians in the intensive care unit can now accurately monitor lung, heart, kidney, and liver function, enabling a better understanding of disease conditions and the development of more effective treatment. However, there is still no tool for easy, bedside monitoring of brain function. When assessing the condition of an unconscious patient, doctors must rely on either crude metrics of brain integrity (e.g., reflexes) or indirect measures of brain health (e.g., intracranial pressure or systemic hemodynamics). While generally successful, these techniques leave many questions unanswered. For example, can pharmacological intervention improve brain development and prevent injury in premature infants? Currently, such a study would require follow-up over a decade to evaluate neuro-developmental outcomes through childhood. A neuroimaging system able to assess brain function in real-time, longitudinally, safely, and at the bedside would thus satisfy a great clinical need.

Traditional neuroimaging modalities can provide valuable information about the brain, but none has been able to satisfy all the requirements of a routine diagnostic tool (Table 1.1). Routine electroencephalography (EEG) monitoring is far from being a standard of care and often requires specialized training for proper interpretation. In addition, its spatial resolution is too poor to be able to resolve regional brain activity. Positron emission tomography (PET) can directly measure brain metabolism, but it's temporal resolution is very low. In addition, it requires exposure to radioactive isotopes. This risk might be acceptable for single scans, but it restricts the ability to perform longitudinal scans (especially in infants). Magnetic resonance imaging (MRI) can detect large structural anatomic injuries, but anatomy is an indirect measure of brain function.

Currently, the gold standard for functional neuroimaging research is functional magnetic resonance imaging (fMRI) with blood oxygenation level dependent (BOLD) contrast. BOLD-fMRI has revolutionized the field of cognitive neuroscience research, and recently has provided important insight into clinical conditions (especially those in mobile patients, such as Alzheimer's and schizophrenia). However, fixed scanners and strong magnetic fields make it difficult to transport critically ill intensive care unit patients for scans. While occasional scanning is possible, a single snap-shot is a poor diagnostic tool in a rapidly evolving clinical environment, especially as one can not predict the crucial moment of injury. Thus, for lack of useful tools for assessment, it is hard to determine how treatments affect brain function and development or to detect injury early enough for treatment to be an effective.

Near-infrared spectroscopy (NIRS) is a neuroimaging methodology uniquely suited to the clinical environment, as it is a mobile system that uses a small, flexible imaging cap [Obrig and Villringer, 2003, Zeff et al., 2007]. NIRS measures neuronal activity indirectly through hemodynamic contrasts similar to BOLD-fMRI. However, NIRS can measure changes in oxygenated hemoglobin (ΔHbO_2), deoxygenated hemoglobin (ΔHbR), and total hemoglobin (ΔHbT), whereas the BOLD signal mostly measures the absolute amount HbR (thus, it is sensitive to a mixture of volume changes and

Table 1.1: Overview of current functional neuroimaging modalities.

	Pros	**Cons**
fMRI	Good spatial resolution Concurrent anatomic information Whole-brain coverage	Low temporal resolution Unknown relationship with metabolism Not portable Magnetic field Loud / Requires stillness
PET	Direct measure of metabolism Many metabolic variables accessible	Very low temporal resolution Low spatial resolution Not portable
EEG	Direct measure of neuronal activity Portable Very high temporal resolution	Difficult to interpret Very low spatial resolution

oxygenation changes [Obata et al., 2004, Raichle and Mintun, 2006, Heeger and Ress, 2002]). The ability to simultaneously image these contrasts allows NIRS to distinguish differences in their magnitude [Meek et al., 1998, Fujiwara et al., 2004, Culver et al., 2003], timing [Meek et al., 1998, Wolf et al., 2002, Jasdzewski et al., 2003, Boden et al., 2007], and localization [Franceschini et al., 2003, Culver et al., 2005, Toronov et al., 2007], forming a more complete picture of neurovascular function. Additionally, the measurement of multiple contrasts is of use in situations in which the neurovascular coupling either is not mature (such as in neonates and very young infants [Anderson et al., 2001, Born et al., 1997, Meek et al., 1998]) or is altered due to injury or illness [Fujiwara et al., 2004, D'Esposito et al., 2003]. In contrast to the ionizing radiation of PET, NIRS uses safe, infrared light for imaging.

It may seem that light would make a poor tool for deep tissue imaging. While light microscopy methods that require only a small depth-of-penetration are well-known, from our daily experience, we expect that light does not penetrate far enough into human tissue to allow measurement of the brain. However, the appearance of opaqueness is primarily due to light scattering; absorption (due primarily to hemoglobin) is much weaker, especially in the near-infrared where one can expect about 100 scattering events per cm versus only 0.1 absorption event per cm. This phenomenon allowing the penetration of highly scattered diffuse light is known as the optical window (Fig. 1.1). Thus, if a light source is held to the head, the light will be highly scattered, but the absorption will be lower than one might expect, allowing photons to be detected at distant positions. Due to the high scattering, the most probable path followed by detected photons is curved (Fig. 1.2).

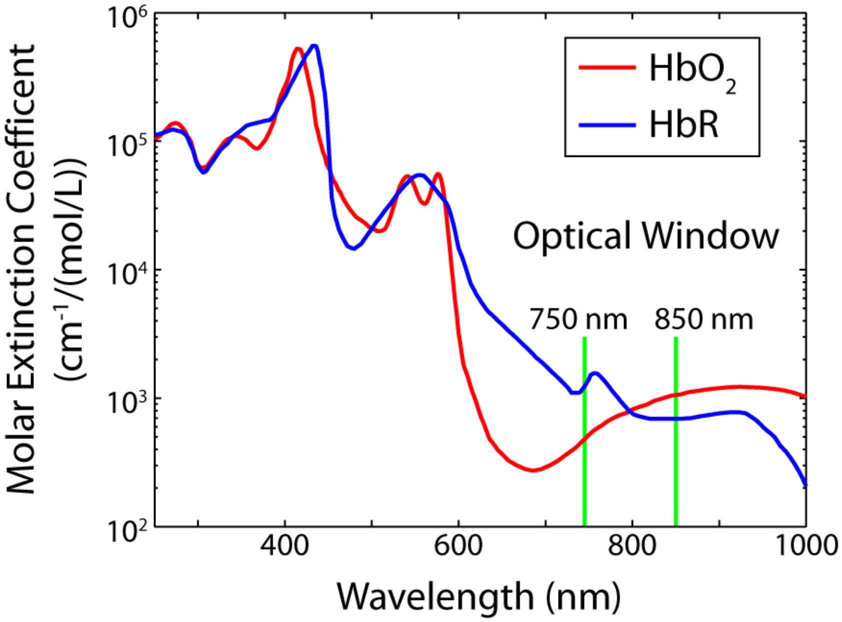

Figure 1.1: Hemoglobin absorption spectra and the optical window. Absorption in the near-infrared "optical window" is two orders of magnitude lower than in the visible, allowing deeper light penetration. Additionally, oxy- and deoxyhemoglobin have divergent spectra, meaning that measurements of absorption at two wavelengths can be used to determine concentrations of both chromophores. The use of wavelengths on either side of the isobesic point (the point of equal extinction coefficient) yields the most mathematically stable spectroscopy.

The principles that underly NIRS have been around for almost a century. In the 1930's visible light was first used to measure blood oxygenation [Pole, 2002]. As the

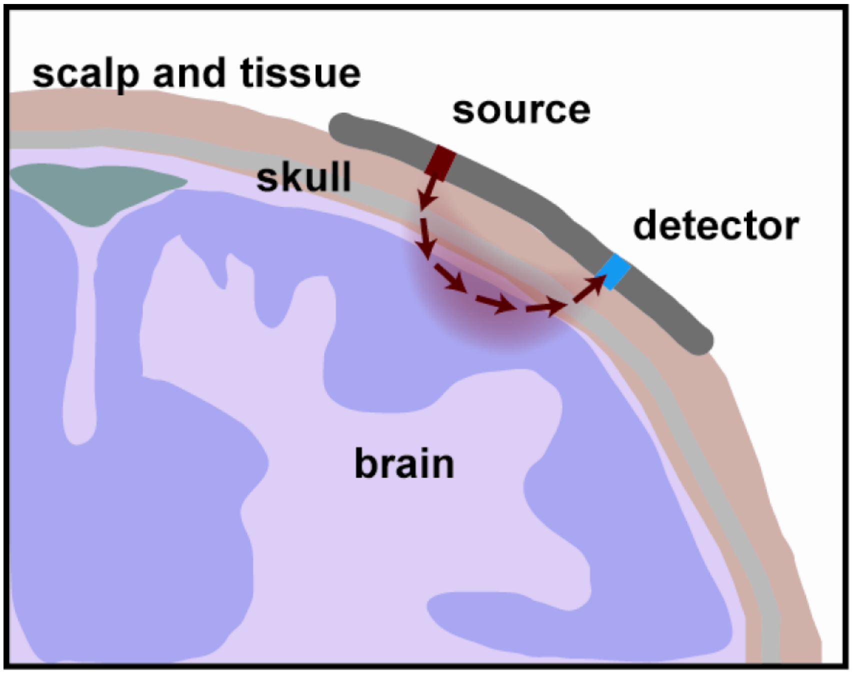

Figure 1.2: Schematic of a NIRS measurement. Light from an exterior source scatters through multiple tissue layers into the brain. Some of this light is detected by distant detectors, resulting in a curved sensitivity profile.

spectra of oxy- and deoxyhemoglobin are different, measurement at two wavelengths allows the determination of the concentrations of the separate hemoglobin species, an observations that enabled the first pulse oximeters, which are now a routine clinical tool. In the 1970's, these ideas were extended to deep tissue measurements of oximetry in the brain [Jöbsis, 1977].

The ability to image brain function through hemodynamic contrasts was first discovered in MRI with the development of the BOLD contrast [Ogawa et al., 1990, Belliveau et al., 1991]. These ideas quickly led to the invention of functional NIRS [Villringer et al., 1993] (Fig. 1.3). However, while fMRI has rapidly become an almost standard neuroscience tool, NIRS, despite it's unique strengths, has remained a seemingly promising modality without widespread acceptance. This is due to two main methodological limitations. First, as is evident from Fig. 1.2, every measurement is a mixture of hemodynamics occurring in multiple tissue layers. Second, NIRS measurements are often conducted using individual channels (e.g., one source-detector pair over the right visual cortex and one over the left). Such discrete sampling has difficulty comparing to fMRI's high-resolution, whole-brain maps overlaid on anatomy. Even when many NIRS measurements are combined to create images (diffuse optical imaging, DOI), the large gaps between measurements should heuristically be expected to result in low spatial resolution and a decreased ability to correctly localize activations.

In order to overcome these limitations, our lab develops diffuse optical tomography (DOT) systems. DOT is a more advanced optical method that uses improved instrumentation to create measurements that overlap both laterally and in depth (see Section 2.2). The entire set of measurements can be inverted to create a 3D reconstruction of hemodynamic changes (in much the same way as a CT scan is derived from multiple X-rays; Section 2.1).[a]

---

[a] In some literature the terms NIRS and DOT are used loosely. Usually, DOT is considered a

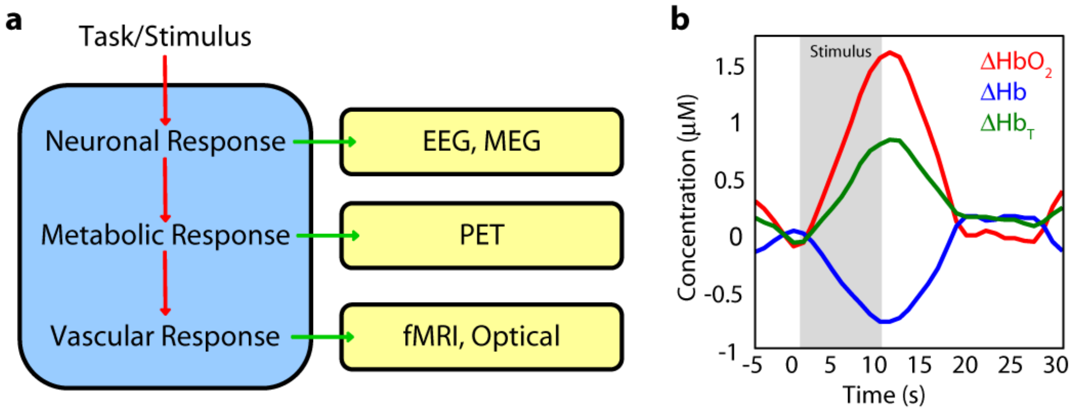

Figure 1.3: Functional neuroimaging through neurovascular coupling. (a) Applying a task or stimulus to the brain causes a neuronal response. This activity triggers a metabolic response, through an unknown mechanism, which in turn leads to a vascular response (again the mechanism is unknown). Each of these stages can be detected non-invasively. (b) Neuronal activity due to a stimulus leads to a delayed vascular response (termed an activation) characterized by an increase in blood volume (positive $\Delta\mathrm{HbT}$) and an increase in oxygenation (increased $\Delta\mathrm{HbO}_2$ and decreased $\Delta\mathrm{HbR}$). While BOLD-fMRI can only measure the $\Delta\mathrm{HbR}$ curve, NIRS (as shown here in response to a visual activation) can measure changes in all three variables.

One method to create such overlapping measurements is time-resolved DOT, which relies on very high temporal resolution to gate detected photons into groups that have traveled to different depths [Benaron et al., 2000, Steinbrink et al., 2001, Hebden et al., 2002, Selb et al., 2005]. These systems require complex electronics and photomultiplier tubes, resulting in a particular set of trade-offs between measurement density, frame-rate, and field-of-view.

The alternative DOT strategy that our lab has followed is to use high-density grids of sources and detectors with each detector sensing light from many sources at different distances [Boas et al., 2004, Zeff et al., 2007, Bluestone et al., 2001]. Such measurements allow the construction of an inversion problem [Yodh and Boas, 2003, Arridge, 1999] (Section 2.1.4), which enables tomographic image reconstructions of brain activity [Zeff et al., 2007, Heiskala et al., 2009, Joseph et al., 2006]. While detecting light over many orders of magnitude places stringent requirements on the system hardware (Section 2.2), overall, such high-density diffuse optical tomography (HD-DOT) systems provide simple, robust instrumentation.

My research has been to develop the *in vivo* use of DOT for advanced neuroimaging. This goal entailed three major aims. First, while the it might seem qualitatively intuitive that a denser grid produces better imaging results, the advantages had not been evaluated specifically for neuroimaging. Thus, I start with an *in silico* evaluation showing quantitatively how HD-DOT advances beyond previous NIRS techniques (Chapter 3).

---

subset of NIRS, but in other cases the two terms are (improperly) used interchangeably. I prefer to separate the two terms more distinctly (again the X-Ray/CT analogy is relevant). Thus, in this work, NIRS will refer to the use of source-detector measurements with the Beer-Lambert Law. NIRS measurements can be analyzed in isolation (usually presented as time traces, as in EEG) or back-projected onto a two-dimensional figure (sometimes referred to as diffuse optical imaging, DOI). DOT will refer to 3D tomographic image reconstructions made from overlapping NIRS measurements. From now on, when I need to refer to the two methods together, I will either do so explicitly ("NIRS and DOT") or use "optical neuroimaging".

Second, it is important to validate DOT advances against the fMRI literature. Many optical research groups take NIRS into new settings (e.g., subjects performing tasks that wouldn't be possible inside an MRI scanner) without first showing the performance of their system against previous neuroscience benchmarks. This limitation makes it difficult to determine the significance of any new neuroscience findings. In part, this mindset is due to trying to take advantage of the unique capabilities of optical techniques. But, it also stems from a desire to avoid the weaknesses of NIRS (especially in terms of spatial resolution) relative to fMRI. The result of this practice is that much of the (non-optical) cognitive neuroscience research community has lost confidence in the technique.

Thus, the second aim was to show that gains in performance from DOT allow us to perform neuroimaging tasks not previously accessible to optical techniques. As a proving ground, we have chosen the visual cortex due to it's high level of organization. Adjacent areas in the visual field activate adjacent areas of the cortex (a property termed retinotopy). Creating maps of this organization was the original validation for both PET and fMRI, showing they could compete with invasive electrophysiology. However, for optical imaging, the spatial resolution of previous systems prevented anything beyond differentiating the right and left hemispheres. This failure to perform what had become a reasonably routine fMRI task was prime evidence of the limitation of optical imaging. Thus, more than many other imaging tasks, the ability to perform retinotopic mapping would restore confidence among researchers and clinicians.

I, thus, demonstrate results that are the first use of optical mapping to differentiate multiple eccentricities and visual angles within each hemisphere and to construct detailed phase-encoded retinotopic maps (Chapter 4). These experiments are the first use of optical neuroimaging to move beyond single activation studies to construct continuous maps of cortical organization. I also show that such a paradigm is not possible with earlier NIRS techniques.

Third, beyond image quality, another obstacle limiting optical imaging's translational progress to bedside imaging is that traditional task-based neuroimaging is ill-suited to clinical populations that may be unable to perform any task. To resolve this dilemma, we looked to recent advances in fMRI where researchers have discovered that even during the absence of overt tasks, fluctuations in brain activity are correlated across functionally-related cortical regions [Biswal et al., 1995]. The spatial and temporal evaluation of spontaneous neuronal activity allows mapping of these resting-state networks [Fox and Raichle, 2007]. Translating these advances to optical techniques would enable new clinical and developmental studies. Still, mapping spontaneous activity with optical measurements presents significant challenges due to the obscuring influences of superficial signals, systemic physiology, and autoregulation. I developed techniques to remove noise and artifacts in order to map functional networks with resting-state measurements (fcDOT, Chapter 5).

The ability to non-invasively assess brain function in premature infants and intensive care patients with traumatic brain injury is a promising clinical application of fcDOT. Because transporting these patients for MRI sessions often raises safety concerns, portable optical imaging methods could fill this valuable clinical niche. Thus, in our current research we collaborate with neonatologists to apply the resting-state methods described above to the bedside imaging of hospitalized infants in the first days of life as a first test of clinical fcDOT. I present our proof-of-principle results in healthy term and preterm neonates, as well as the relevant clinical example of an infant with a stroke (Chapter 6).

In it's entirety, this work shows the advantages of DOT, it's power in performing new neuroimaging paradigms, and a possible future clinical role. Our lab hopes that these results help DOT and functional connectivity methods move forward as important tools in diagnosing and monitoring the progress of brain-injured patients.

Chapter 2

Methods for Diffuse Optical Tomography

2.1 Theory

2.1.1 Overview of the Imaging Problem

The goal of optical neuroimaging is to detect changes in hemoglobin concentrations (presumably induced by neuronal activity) through the measurement of light intensities with sources and detectors around the exterior of the head. Determining the absolute concentration of hemoglobin is difficult; thus, we rely on differential measurements relative to a pre-stimulus or average baseline[a].

As we can model how light flows in a scattering and absorbing medium, we will be able to answer the question: "Given volumetric changes in the absorption coefficient, what changes in measured light intensity do we expect?" However, the more inter-

---

[a] This follows the norm in BOLD-fMRI imaging, where the vast the majority of studies are differential in nature. In fact, the question of whether the absolute value of the BOLD signal can be meaningfully interpreted is still an active field of research.

esting and relevant question is: “Given a set of differential light intensities, what set of absorption changes do we expect produced those changes?” What separates DOT from NIRS is how one approaches the latter question. In NIRS, one simply divides the measured value by a constant based on the expected mean path length of the photons in the tissue (i.e., the assumption is that the absorption change was evenly distributed over the photon’s path). This analysis (known as the Beer-Lambert Law) can be made more involved through constraints and assumptions about partial volume effects, but at it’s core there is no ability to distinguish changes that happen at different locations along the measurement path

The mindset of DOT is to attempt to use our ability to answer the first question–that is we can construct a “forward model” of light propagation in tissue–to generate an “inverse model” that allows us to answer the second question. This is analogous to the problem of computed tomography (CT). In that setting, individual measurements (X-rays) create projections of the density distribution within the body. Thus the forward model is straight-forward. Given a density distribution, the X-ray measurement is simply the integral of density along the incident axis. After taking projections from many angles, the assemblage of these measurements is inverted to create the most likely three-dimensional density distribution that would have created all the projections (Fig. 2.1a). We wish to construct a similar formulation for DOT (Fig. 2.1b). Our forward model is provided by the physics of diffuse light flow (Section 2.1.2) and finite element modeling (Section 2.1.3). We will then use this knowledge to create an inverse problem that can be efficiently solved (Section 2.1.4).

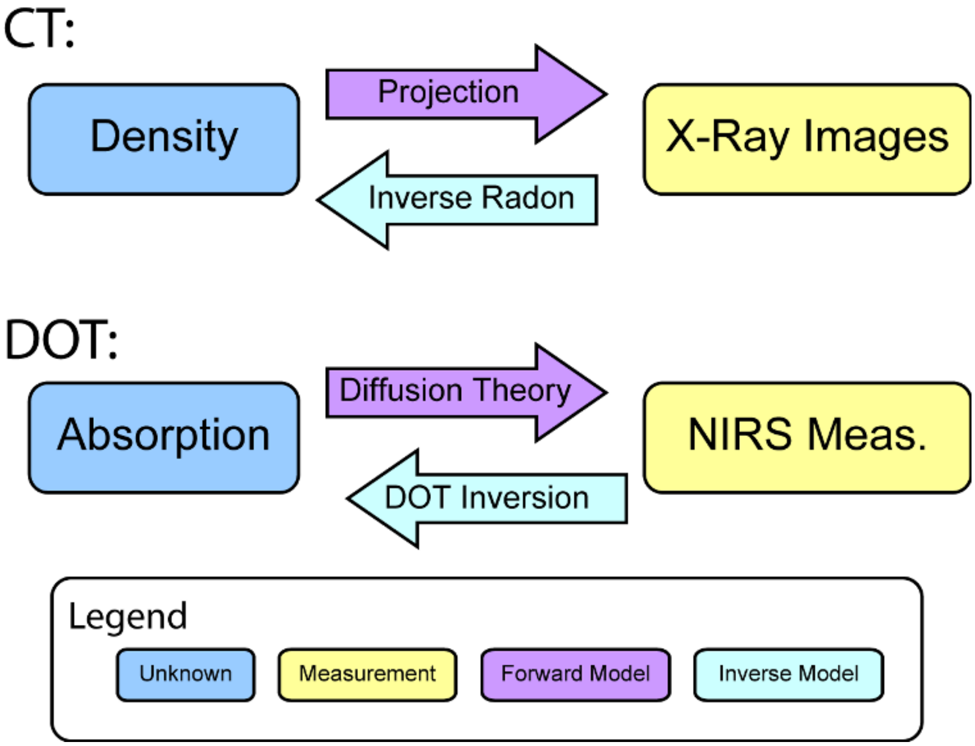

Figure 2.1: Forward and inverse models in CT and DOT. In both CT and DOT, we wish to know the 3D distribution of a physical quantity (density and absorption changes, respectively). However, the only measurements we have are projections (linear X-rays with CT, and diffuse photon paths with DOT). By mathematical modeling of the forward process, we can generate effective inverse models that allow accurate reconstruction of 3D images from an assemblage of 2D measurements.

2.1.2 The Forward Model for Diffuse Light Flow

The flow of near-infrared light through the human head is governed by the diffuse approximation to the radiative transport equation[b] (RTE) [Wang and Hsin-I, 2007]:

$$D\nabla^2\Phi(\mathbf{r}) - v\mu_a(\mathbf{r})\Phi(\mathbf{r}) = -vS(\mathbf{r}) \tag{2.1}$$

Here, Φ is the photon fluence (light intensity), v is the speed of light in the medium, S is a source distribution, and D is the diffusion coefficient[c]:

$$D = \frac{v}{3(\mu_s' + \mu_a)} \tag{2.2}$$

μ_a is the absorption coefficient. μ_s' is the reduced scattering coefficient, which is related to the scattering coefficient, μ_s, by the tissue scattering anisotropy, g, by:

$$\mu_s' = (1 - g)\mu_s \tag{2.3}$$

This correction results in a longer effective scattering mean free path due to the biased forward scattering of tissue. In biological tissue, g is approximately 0.9; so, a photon can be considered isotropically scattered after 10 scattering events.

---

[b] This is the time-independent differential equation, as all the systems we will consider are "continuous wave", where any variations in light intensity occur on a time-scale much longer than the mean transit time of light.

[c] Sometimes D is defined without v in the numerator. This changes the form of constant in front of the equation and solutions but not their content or form.

The Born Approximation

We can solve this differential equation (2.1) using the Born Approximation:

$$\Phi(\mathbf{r}) = \Phi_0(\mathbf{r}) + \Phi_1(\mathbf{r}) \quad \text{with} \quad \Phi_0(\mathbf{r}) \gg \Phi_1(\mathbf{r}) \tag{2.4}$$

$$\mu_a(\mathbf{r}) = \mu_{a,0}(\mathbf{r}) + \mu_{a,1}(\mathbf{r}) \quad \text{with} \quad \mu_{a,0}(\mathbf{r}) \gg \mu_{a,1}(\mathbf{r}) \tag{2.5}$$

We make the assumption that since $\mu_s' \gg \mu_{a,0} \gg \mu_{a,1}$, D is unperturbed, despite changes in μ_a. Inserting these perturbation series into Eq. 2.1, yields:

$$\left[\nabla^2 - \frac{v}{D}\left(\mu_{a,0}(\mathbf{r}) + \mu_{a,1}(\mathbf{r})\right)\right]\left[\Phi_0(\mathbf{r}) + \Phi_1(\mathbf{r})\right] = -\frac{v}{D}S(\mathbf{r}) \tag{2.6}$$

Gathering all the zeroth- and first-order terms together gives two differential equations (we neglect higher-order terms).

$$\left(\nabla^2 - \frac{v}{D}\mu_{a,0}(\mathbf{r})\right)\Phi_0(\mathbf{r}) = -\frac{v}{D}S(\mathbf{r}) \tag{2.7}$$

$$\left(\nabla^2 - \frac{v}{D}\mu_{a,0}(\mathbf{r})\right)\Phi_1(\mathbf{r}) = \frac{v}{D}\mu_{a,1}(\mathbf{r})\Phi_0(\mathbf{r}) \tag{2.8}$$

Note that the operator on the left-hand side of both of these equations is the same. The only difference is in the inhomogeneous "source" term on the right-hand side. Also, the zeroth-order term depends only on the baseline optical properties, and the first-order term has a source term dependent on the zeroth-order solution and the perturbation in the optical properties.

Both differential equations can be solved with the method of Green's functions. Assume that we can find the solution to the differential equation:

$$\left(\nabla^2 - \frac{v}{D}\mu_{a,0}(\mathbf{r})\right)G(\mathbf{r}', \mathbf{r}) = -\delta(\mathbf{r} - \mathbf{r}') \tag{2.9}$$

Then, the solution to Equation 2.7 is given by:

$$\Phi_0(\mathbf{r}) = \frac{v}{D}\int G(\mathbf{r}', \mathbf{r})S(\mathbf{r}')d\mathbf{r}' \tag{2.10}$$

This can be easily verified with substitution:

$$\begin{aligned}
\left(\nabla^2 - \frac{v}{D}\mu_{a,0}(\mathbf{r})\right)\Phi_0(\mathbf{r}) &= \left(\nabla^2 - \frac{v}{D}\mu_{a,0}(\mathbf{r})\right)\left[\frac{v}{D}\int G(\mathbf{r}', \mathbf{r})S(\mathbf{r}')d\mathbf{r}'\right] \\
&= \frac{v}{D}\int\left[\left(\nabla^2 - \frac{v}{D}\mu_{a,0}(\mathbf{r})\right)G(\mathbf{r}', \mathbf{r})\right]S(\mathbf{r}')d\mathbf{r}' \\
&= -\frac{v}{D}\int \delta(\mathbf{r} - \mathbf{r}')S(\mathbf{r}')d\mathbf{r}' \\
&= -\frac{v}{D}S(\mathbf{r}) \qquad (2.11)
\end{aligned}$$

Similarly, the solution to Equation 2.8 is:

$$\Phi_1(\mathbf{r}) = -\int G(\mathbf{r}', \mathbf{r})\frac{v}{D}\mu_{a,1}(\mathbf{r}')\Phi_0(\mathbf{r}')d\mathbf{r}' \tag{2.12}$$

Since we already know the solution to Φ_0 (Eq. 2.10), we can expand this as:

$$\begin{aligned}
\Phi_1(\mathbf{r}) &= -\int G(\mathbf{r}', \mathbf{r})\frac{v}{D}\mu_{a,1}(\mathbf{r}')\int \frac{v}{D}G(\mathbf{r}'', \mathbf{r}')S(\mathbf{r}'')d\mathbf{r}''d\mathbf{r}' \\
&= -\left(\frac{v}{D}\right)^2\int\int G(\mathbf{r}', \mathbf{r})G(\mathbf{r}'', \mathbf{r}')S(\mathbf{r}'')\mu_{a,1}(\mathbf{r}')d\mathbf{r}''d\mathbf{r}' \qquad (2.13)
\end{aligned}$$

We now know the measured change in light intensity at point $\mathbf{r}$, $\Phi_1(\mathbf{r})$, due to the perturbation distribution of intensity changes, $\mu_{a,1}(\mathbf{r}')$.

Now, we will make a few substitutions for clarity. Since, we will not deal with perturbations higher than first order, we will simply define: $\Delta\mu_a(\mathbf{r}) \equiv \mu_{a,1}(\mathbf{r})$. For convenience we relabel the $\mathbf{r}$'s: $\mathbf{r}_s \equiv \mathbf{r}''$ (source position), $\mathbf{r}_d \equiv \mathbf{r}$ (detector position), and $\mathbf{r}_v \equiv \mathbf{r}'$ (voxel position). Additionally, when we detect light, we do so with a detector that has some spatial sensitivity distribution, $D(\mathbf{r})$. So, the actual measured change in light intensity in source-detector measurement, i is: $\Delta\Phi_i = \int \Phi_1(\mathbf{r}_d)D(\mathbf{r}_d)d\mathbf{r}_d$.

$$\Delta\Phi_i = -\left(\frac{v}{D}\right)^2 \int\int\int G(\mathbf{r}_v,\mathbf{r}_d)G(\mathbf{r}_s,\mathbf{r}_v)S(\mathbf{r}_s)D(\mathbf{r}_d)\Delta\mu_a(\mathbf{r}_v)d\mathbf{r}_s d\mathbf{r}_v d\mathbf{r}_d \qquad (2.14)$$

Often, when we solve for the Green's functions, we explicitly include the source and detector geometries rather than integrating them in later. Thus, we can define the effective Green's functions:

$$\begin{aligned} \tilde{G}_s(\mathbf{r}_v) &= \int G(\mathbf{r}_s,\mathbf{r}_v)S(\mathbf{r}_s)d\mathbf{r}_s & (2.15)\\ \tilde{G}_d(\mathbf{r}_v) &= \int G(\mathbf{r}_v,\mathbf{r}_d)D(\mathbf{r}_d)d\mathbf{r}_d & (2.16)\end{aligned}$$

We can simplify Equation 2.14 to:

$$\Delta\Phi_i = -\left(\frac{v}{D}\right)^2 \int \tilde{G}_s(\mathbf{r}_v)\tilde{G}_d(\mathbf{r}_v)\Delta\mu_a(\mathbf{r}_v)d\mathbf{r}_v \qquad (2.17)$$

We can break down this equation into three heuristic parts: (1) light propagation from the source to the voxel, $\tilde{G}_s(\mathbf{r}_v)$; (2) an interaction at the voxel, $\Delta\mu_a(\mathbf{r}_v)$; and (3) light propagation from the voxel to the detector, $\tilde{G}_d(\mathbf{r}_v)$. We then integrate these effects over all voxels in the volume.

Equivalently, we can rewrite Equation 2.10 as:

$$\Phi_{0,i} = \frac{v}{D}\int\int G(\mathbf{r}_s,\mathbf{r}_d)S(\mathbf{r}_s)D(\mathbf{r}_d)d\mathbf{r}_s d\mathbf{r}_d \equiv \frac{v}{D}\tilde{G}_{sd} \qquad (2.18)$$

Thus, the entire photon fluence solution (for source-detector combination, i) is (using Equations 2.18 and 2.17 in Equation 2.4):

$$\Phi_i = \frac{v}{D}\tilde{G}_{sd} - \left(\frac{v}{D}\right)^2 \int \tilde{G}_s(\mathbf{r}_v)\tilde{G}_d(\mathbf{r}_v)\Delta\mu_a(\mathbf{r}_v)d\mathbf{r}_v \tag{2.19}$$

The Rytov Approximation

Note that Equation 2.19 assumes a difference measurement: the measurement we will work with ($\Delta\Phi_i$, the integrated piece) will be equal to a measurement taken after the perturbation (Φ_i) minus a baseline measurement ($\tilde{G}_{sd}$). (Rewriting, Eq. 2.4: $\Delta\Phi = \Phi - \Phi_0$.) It is often more convenient to work with ratiometric measurements. Thus, we consider the Rytov approximation[d]:

$$\Phi(\mathbf{r}) = \Phi_0(\mathbf{r})e^{\Phi_1(\mathbf{r})} \quad \text{with} \quad \Phi_0(\mathbf{r}) \gg \Phi_1(\mathbf{r}) \tag{2.20}$$

Note, that now we will now have:

$$\Delta\Phi_i = \ln(\Phi/\Phi_0) \tag{2.21}$$

---

[d] This derivation follows the outline from [Kak and Slaney, 1988], although the differential equation is of slightly different form.

We can use Eq. 2.20 (along with Eq. 2.5) in the original differential equation (2.1):

$$\begin{aligned}
-vS(\mathbf{r}) &= D\nabla^2\Phi_0(\mathbf{r})e^{\Phi_1(\mathbf{r})} - v\left(\mu_{a,0}(\mathbf{r}) + \mu_{a,1}(\mathbf{r})\right)\Phi_0(\mathbf{r})e^{\Phi_1(\mathbf{r})} \\
-vS(\mathbf{r}) &= D\left[\nabla^2\Phi_0(\mathbf{r}) + 2\nabla\Phi_0(\mathbf{r})\cdot\nabla\Phi_1(\mathbf{r})\right. \\
&\quad \left. + \Phi_0(\mathbf{r})\nabla^2\Phi_1(\mathbf{r}) + \Phi_0(\mathbf{r})\left(\nabla\Phi_1(\mathbf{r})\right)^2\right] e^{\Phi_1(\mathbf{r})} \\
&\quad -v\left(\mu_{a,0}(\mathbf{r}) + \mu_{a,1}(\mathbf{r})\right)\Phi_0(\mathbf{r})e^{\Phi_1(\mathbf{r})} \\
-vS(\mathbf{r})e^{-\Phi_1(\mathbf{r})} &= D\left[\nabla^2\Phi_0(\mathbf{r}) + 2\nabla\Phi_0(\mathbf{r})\cdot\nabla\Phi_1(\mathbf{r})\right. \\
&\quad \left. +\Phi_0(\mathbf{r})\nabla^2\Phi_1(\mathbf{r}) + \Phi_0(\mathbf{r})\left(\nabla\Phi_1(\mathbf{r})\right)^2\right] \\
&\quad -v\left(\mu_{a,0}(\mathbf{r}) + \mu_{a,1}(\mathbf{r})\right)\Phi_0(\mathbf{r}) \qquad (2.22)
\end{aligned}$$

We now group zeroth- and first-order terms (note that $[\nabla\Phi_1(\mathbf{r})]^2$ is a second-order term, which we neglect):

$$\begin{aligned}
-vS(\mathbf{r}) &= D\nabla^2\Phi_0(\mathbf{r}) - v\mu_{a,0}(\mathbf{r})\Phi_0(\mathbf{r}) \qquad (2.23) \\
vS(\mathbf{r})\Phi_1(\mathbf{r}) + v\mu_{a,1}(\mathbf{r})\Phi_0(\mathbf{r}) &= 2D\nabla\Phi_0(\mathbf{r})\cdot\nabla\Phi_1(\mathbf{r}) + D\Phi_0(\mathbf{r})\nabla^2\Phi_1(\mathbf{r}) \qquad (2.24)
\end{aligned}$$

Note that Eq. 2.23 is the same as Eq. 2.7; so, the solution is Eq. 2.10. To solve Eq. 2.24, note that:

$$\nabla^2(\Phi_0(\mathbf{r})\Phi_1(\mathbf{r})) = \Phi_1(\mathbf{r})\nabla^2\Phi_0(\mathbf{r}) + 2\nabla\Phi_0(\mathbf{r})\cdot\nabla\Phi_1(\mathbf{r}) + \Phi_0\nabla^2\Phi_1(\mathbf{r}) \qquad (2.25)$$

So, we can rewrite Eq. 2.24 as:

$$vS(\mathbf{r})\Phi_1(\mathbf{r}) + v\mu_{a,1}(\mathbf{r})\Phi_0(\mathbf{r}) = D\nabla^2(\Phi_0(\mathbf{r})\Phi_1(\mathbf{r})) - D\Phi_1(\mathbf{r})\nabla^2\Phi_0(\mathbf{r})$$

$$\Phi_1(\mathbf{r})\left\{vS(\mathbf{r}) + D\nabla^2\Phi_0(\mathbf{r})\right\} + v\mu_{a,1}(\mathbf{r})\Phi_0(\mathbf{r}) = D\nabla^2(\Phi_0(\mathbf{r})\Phi_1(\mathbf{r})) \qquad (2.26)$$

Note that piece of Equation 2.26 in braces is simply part of Equation 2.7. Thus, we can now make the substitution to get:

$$v\mu_{a,0}(\mathbf{r})\Phi_0(\mathbf{r})\Phi_1(\mathbf{r}) + v\mu_{a,1}(\mathbf{r})\Phi_0(\mathbf{r}) = D\nabla^2(\Phi_0(\mathbf{r})\Phi_1(\mathbf{r})) \tag{2.27}$$

This reduces to the original differential equation that we know how to solve (Eq. 2.7):

$$\left(D\nabla^2 - v\mu_{a,0}(\mathbf{r})\right)[\Phi_0(\mathbf{r})\Phi_1(\mathbf{r})] = v\mu_{a,1}(\mathbf{r})\Phi_0(\mathbf{r}) \tag{2.28}$$

This has the Green's function solution:

$$\Phi_0(\mathbf{r})\Phi_1(\mathbf{r}) = -\frac{v}{D}\int G(\mathbf{r}', \mathbf{r})\mu_{a,1}(\mathbf{r}')\Phi_0(\mathbf{r}')d\mathbf{r}' \tag{2.29}$$

Rearranging for $\Phi_1(\mathbf{r})$ and using our earlier definitions:

$$\Delta\Phi_i = -\frac{v}{D}\int \frac{\tilde{G}_s(\mathbf{r}_v)\Delta\mu_a(\mathbf{r}_v)\tilde{G}_d(\mathbf{r}_v)}{\tilde{G}_{sd}}d\mathbf{r}_v \tag{2.30}$$

Since $\Phi_1(\mathbf{r}) = \ln(\Phi(\mathbf{r})/\Phi_0(\mathbf{r}))$ (Eq. 2.20), we have:

$$-\ln\left(\frac{\Phi}{\Phi_0}\right) = \frac{v}{D}\int \frac{\tilde{G}_s(\mathbf{r}_v)\tilde{G}_d(\mathbf{r}_v)}{\tilde{G}_{sd}}\Delta\mu_a(\mathbf{r}_v)d\mathbf{r}_v \tag{2.31}$$

We can easily convert from the Born solution to the Rytov solution by dividing by Φ_0 and using the Taylor series approximation $\ln(1+x) \approx 1-x$ for $x \ll 1$. Similarly, using the Taylor series for e^x for small x and multiplying by Φ_0 will convert the Rytov solution into the Born solution.

While Eq. 2.31 is a solution to the original differential equation (Eq. 2.1), we have still not shown how to solve Eq. 2.9 (i.e., we still have to derive an expression for the Green's function). In a limited number of circumstances, we can solve this equation analytically (specifically in infinite and semi-infinite media with homogeneous baseline optical properties, μ_a and D) [Wang and Hsin-I, 2007]. However, in most circumstances, we will have to resort to numerical methods (Section 2.3.3).

2.1.3 Discretization

The next step in getting a voxel map of absorption changes from our measurements is to discretize our model. We convert our integral (Eq. 2.31) to a summation over voxels:

$$-\ln\left(\frac{\Phi}{\Phi_0}\right) = \frac{vV_{vox}}{D} \sum_{j \in \text{voxels}} \frac{\tilde{G}_s(\mathbf{r}_j)\tilde{G}_d(\mathbf{r}_j)}{\tilde{G}_{sd}} \Delta\mu_a(\mathbf{r}_j) \tag{2.32}$$

Here, V_{vox} is the volume of a voxel.

We can write in matrix format (M is the number of measurements and N is the number of voxels):

$$\begin{bmatrix} y_1 \\ \vdots \\ y_M \end{bmatrix} = -\frac{vV_{vox}}{D} \begin{bmatrix} A_{1,1} & \cdots & A_{1,N} \\ \vdots & \ddots & \vdots \\ A_{M,1} & \cdots & A_{M,N} \end{bmatrix} \begin{bmatrix} \Delta\mu_a(\mathbf{r}_1) \\ \vdots \\ \Delta\mu_a(\mathbf{r}_N) \end{bmatrix} \tag{2.33}$$

Here, y_i is the i^{th} source-detector measurement (associated with source s_i and detector d_i) and $A_{i,j}$ is the sensitivity of measurement i in voxel j:

$$A_{i,j} = \frac{\tilde{G}_{s_i}(\mathbf{r}_j)\tilde{G}_{d_i}(\mathbf{r}_j)}{\tilde{G}_{s_i d_i}} \tag{2.34}$$

Thus, we define the A-matrix:

$$\mathbf{A} \equiv -\frac{vV_{vox}}{D}\begin{bmatrix} A_{1,1} & \cdots & A_{1,N} \\ \vdots & \ddots & \vdots \\ A_{M,1} & \cdots & A_{M,N} \end{bmatrix} \tag{2.35}$$

And we can rewrite Equation 2.33 as:

$$\mathbf{y} = \mathbf{A}\mathbf{x} \tag{2.36}$$

Where $\mathbf{x}$ is the vector of absorption changes. This is the summation of the "forward model": given a set of absorption changes in the head, $\mathbf{x}$, and our model of light propagation, $\mathbf{A}$, we can predict the expected changes in our measurements, $\mathbf{y}$.

2.1.4 Inversion

The problem of DOT now reduces to inverting Equation 2.36. It would seem that we could just assert that $\mathbf{x} = \mathbf{A}^{-1}\mathbf{y}$. However, $\mathbf{A}$ is non-square, and so such an inverse does not exist. We can instead construct a pseudo-inverse: $\mathbf{x} = \mathbf{A}^{\#}\mathbf{y}$ where $\mathbf{A}^{\#} = (\mathbf{A}^T\mathbf{A})^{-1}\mathbf{A}^T$; since $\mathbf{A}^T\mathbf{A}$ is square, it's inverse is defined.

However, this inverse method is unstable, which is clear if we use singular value decomposition (SVD) to analyze $\mathbf{A}$. The SVD of $\mathbf{A}$ is $\mathbf{A} = \mathbf{U}\mathbf{S}\mathbf{V}^T$, where $\mathbf{U}$ is matrix of measurement modes, $\mathbf{V}$ is a matrix of spatial modes, and $\mathbf{S}$ is a diagonal matrix of singular values that ranks the order of importance of the singular vectors in $\mathbf{U}$ and $\mathbf{V}$ by their contribution to $\mathbf{A}$. In practice, since diffuse light follows a highly scattered path, the sensitivity functions are blurred, and only singular values corresponding to low-frequency spatial modes (Fig. 2.2) are important. Thus, the diagonal of $\mathbf{S}$ is a rapidly decreasing function (Fig. 2.3).

Using this knowledge, let's examine the pseudo-inverse (Note that $\mathbf{U}^{-1} = \mathbf{U}^T$ and

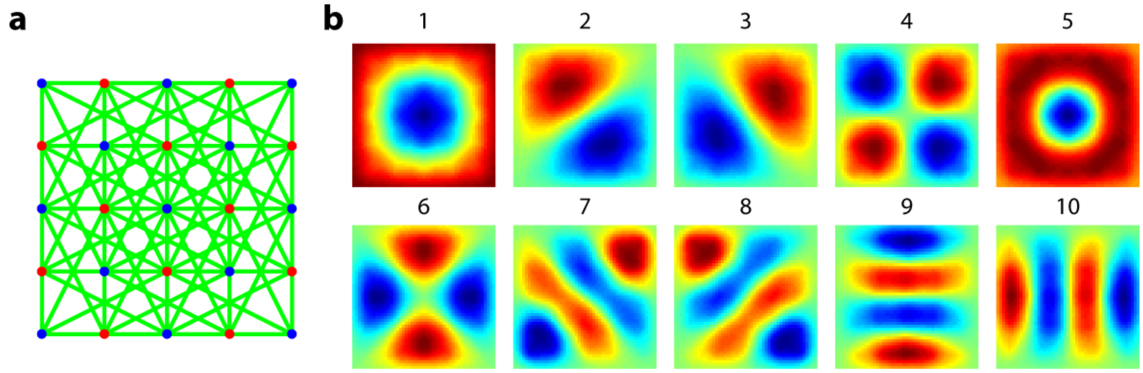

Figure 2.2: Spatial modes of a sensitivity matrix. (a) Sources (red), detectors (blue), and measurements (green) in a square high-density DOT array simulated over a semi-infinite geometry with optical properties similar to those in the brain. (b) The first 10 singular modes in the A-matrix from the optode grid in (a) averaged over depths of 5 to 15 mm. Note that as the singular vector index increases, the spatial frequencies increase.

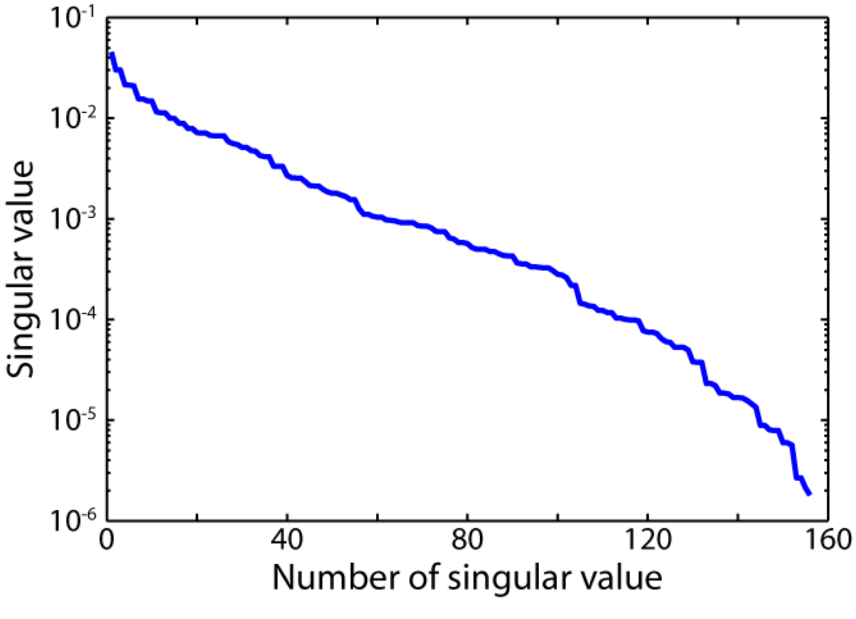

Figure 2.3: Singular values of a sensitivity matrix (same as in Fig. 2.2). As we move along the diagonal of the matrix of singular values (the x-axis), the singular values decrease rapidly.

equivalently for $\mathbf{V}$).

$$\begin{aligned}
\mathbf{A}^{\#} &= (\mathbf{A}^T\mathbf{A})^{-1}\mathbf{A}^T \\
&= (\mathbf{VSU}^T\mathbf{USV}^T)^{-1}\mathbf{VSU}^T \\
&= (\mathbf{VS}^2\mathbf{V}^T)^{-1}\mathbf{VSU}^T \\
&= \mathbf{V}(\mathbf{S}^2)^{-1}\mathbf{V}^T\mathbf{VSU}^T \\
&= \mathbf{V}(\mathbf{S}^2)^{-1}\mathbf{SU}^T \\
&= \mathbf{VS}^{-1}\mathbf{U}^T \qquad (2.37)
\end{aligned}$$

The smallest singular values in $\mathbf{S}$ assume out-sized importance, as their inverses are very large numbers.

Thus, it is important to regularize the inverse, which provides a cut-off along the diagonal of $\mathbf{S}$. This limit determines the number of spatial modes that we will allow in the reconstruction. This procedure is called Tikhonov regularization, and we instead invert:

$$\mathbf{A}^{\#} = \left[\mathbf{A}^T\mathbf{A} + \lambda_1 \max\{\mathrm{diag}(\mathbf{S})\}\mathbf{I}\right]^{-1}\mathbf{A}^T \qquad (2.38)$$

Here, $\mathbf{I}$ is the identity matrix, λ_1 is the "regularization constant" that determines how many modes to include, and $\max\{\mathrm{diag}(\mathbf{S})\}$ is a normalization term so that λ_1 can be set independently of the absolute values in $\mathbf{A}$. If λ_1 is 10^{-2}, then that means that all modes with singular values within 10^{-2} of the maximum singular value will be included in the reconstruction.

As $\mathbf{A}^T\mathbf{A}$ is an $N \times N$ matrix (with N the number of voxels), it is usually more memory-efficient to use the equivalent formulation:

$$\mathbf{A}^{\#} = \mathbf{A}^{T}\left[\mathbf{A}\mathbf{A}^{T} + \lambda_1 \max\{\mathrm{diag}(\mathbf{S})\}\mathbf{I}\right]^{-1} \tag{2.39}$$

Thus, we only need to invert something of size $M \times M$ (where M is the number of measurements), since $M \ll N$.

An additional consideration is that the sensitivity of measurements drop off very quickly into the head due to the exponential attenuation of light. Thus, the reconstruction preferentially places absorption changes on the surface of the head, nearest the optodes. This effect results in changes in the brain being reconstructed artificially shallowly. To remove this artifact, we apply spatially-variant regularization to normalize the sensitivity within each voxel. We could simply divide each column of $\mathbf{A}$ (corresponding to a voxel) by it's norm. However, there are areas of the reconstructed volume with almost no sensitivity (e.g., deep in the head or on the periphery of the optode array), and equally normalizing every voxel would result to an equivalent problem to that in Equation 2.37.

Thus, we apply a second regularization to keep the normalization within reasonable limits. We construct the diagonal matrix $\mathbf{L}$ with:

$$\mathrm{diag}(\mathbf{L}) = \sqrt{\mathrm{diag}(\mathbf{A}^{T}\mathbf{A}) + \lambda_2 \mathrm{max}\{\mathrm{diag}(\mathbf{A}^{T}\mathbf{A})\}} \tag{2.40}$$

We, now, create the spatially-normalized A-matrix:

$$\tilde{\mathbf{A}} = \mathbf{L}^{-1}\mathbf{A} \tag{2.41}$$

As long as the sensitivity in a voxel is greater than λ_2 times the maximum sensitivity, then the first term in Eq. 2.40 dominates and this formulation is equivalent to dividing the column by its norm. However, if the norm of the column is small, the second term dominates. Thus, no matter how small diag($\mathbf{A}^T\mathbf{A}$), the column will always be normalized by approximately $\sqrt{\lambda_2}$ times the maximum sensitivity. This regularization thus prevents division by overly small numbers, which would create artificially high reconstruction values in regions with very low measurement sensitivity.

To balance the original equation (2.36), we have to multiply the left-hand side by $\mathbf{L}^{-1}$ as well:

$$\mathbf{L}^{-1}\mathbf{y} = \tilde{\mathbf{A}}\mathbf{x} \tag{2.42}$$

We now invert $\tilde{\mathbf{A}}$ as in Equation 2.39 (where $\mathbf{S}$ now comes from the SVD of $\tilde{\mathbf{A}}$):

$$\tilde{\mathbf{A}}^{\#} = \tilde{\mathbf{A}}^T \left[\tilde{\mathbf{A}}\tilde{\mathbf{A}}^T + \lambda_1 \max\{\mathrm{diag}(\mathbf{S})\}\mathbf{I}\right]^{-1} \tag{2.43}$$

We can then undo the spatial regularization:

$$\hat{\mathbf{A}}^{\#} = \tilde{\mathbf{A}}^{\#}\mathbf{L}^{-1} \tag{2.44}$$

And, our final reconstruction equation is:

$$\mathbf{x} = \hat{\mathbf{A}}^{\#}\mathbf{y} \tag{2.45}$$

Or, combining all the above equations:

$$\mathbf{x} = \left(\mathbf{L}^{-1}\mathbf{A}\right)^T \left[\mathbf{L}^{-1}\mathbf{A}\left(\mathbf{L}^{-1}\mathbf{A}\right)^T + \lambda_1 \max\{\mathrm{diag}(\mathbf{S})\}\mathbf{I}\right]^{-1} \mathbf{L}^{-1}\mathbf{y} \tag{2.46}$$

This method is known as direct inversion and is used for all of our neuroimaging reconstructions. It's advantage is that a single inversion procedure creates a matrix which can be multiplied against a matrix, $\mathbf{y}(t)$ (measurements by time), to create a times series of absorption changes, $\mathbf{x}(t)$ (voxels by time), all in a single step. In contrast, iterative procedures would yield more accurate reconstructions at each time point, but would be inefficient to perform for every time point analyzed.

2.2 DOT Imaging System

A DOT system needs to satisfy two goals. First, the sensitivity functions of source-detector measurements need to penetrate deeply enough into the head in order to be able to detect brain activations. Second, we need an arrangement with overlapping measurements, both laterally and in depth, to allow us to perform a 3D reconstruction with reasonable spatial resolution. In order to accomplish these objectives, we have designed high-density optode arrangements (Fig. 2.4). From each source, light is detected at multiple source-detector distances (Fig. 2.5a); we define the closest separation as "first-nearest neighbors", and increasing discrete distances are known as second-, third-, and fourth-nearest neighbors. We call the set of all 1st-nearest neighbors nn_1 (and similarly for nn_2, nn_3, etc.). For imaging, we will wish (for example) to use 1st- through 4th-nearest neighbors; these unions will be called nn_{12}, nn_{123}, etc.

The ability to detect light at multiple distances means that measurements overlap in depth: the 1st-nearest neighbors (1.3 cm in the adult systems) are primarily sensitive to scalp and skull, while 2nd-nearest neighbors sample into the brain (Fig. 2.5b). The use of increasing source-detector separations should allow deeper brain sensitivity (Fig. 2.6) [Dehghani et al., 2009].

In order to distinguish which detected light came from which source, we use a combination of temporal, frequency, and spatial encoding. Temporal encoding means that nearby sources are illuminated sequentially. At each source location, we illuminate with the two wavelengths of light simultaneously, but modulate at different

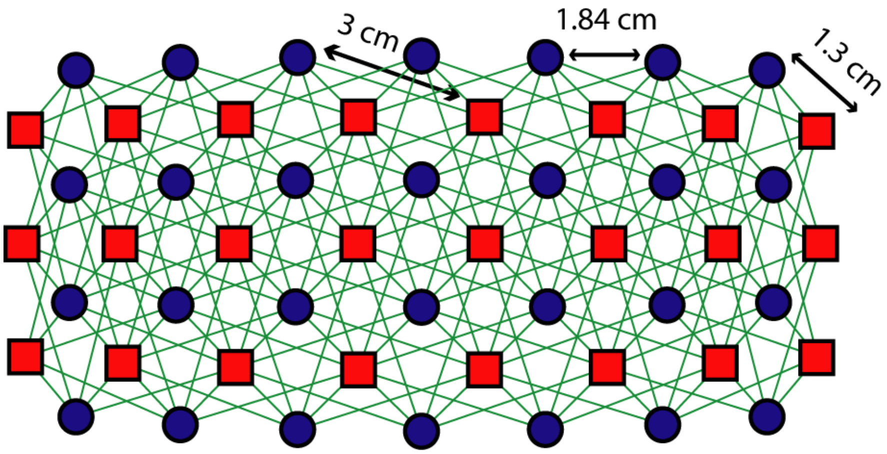

Figure 2.4: Example of an optode grid for neuroimaging. Sources are in red, detectors in blue, and measurements in green (1^{st}- and 2^{nd}-nearest neighbors are shown). In adults, 1^{st}-nearest neighbors are separated by 1.3 cm, and 2^{nd}-nearest neighbors by 3 cm. This separation and field-of-view are sufficient to perform mapping over cortical regions, such as the visual or motor cortices.

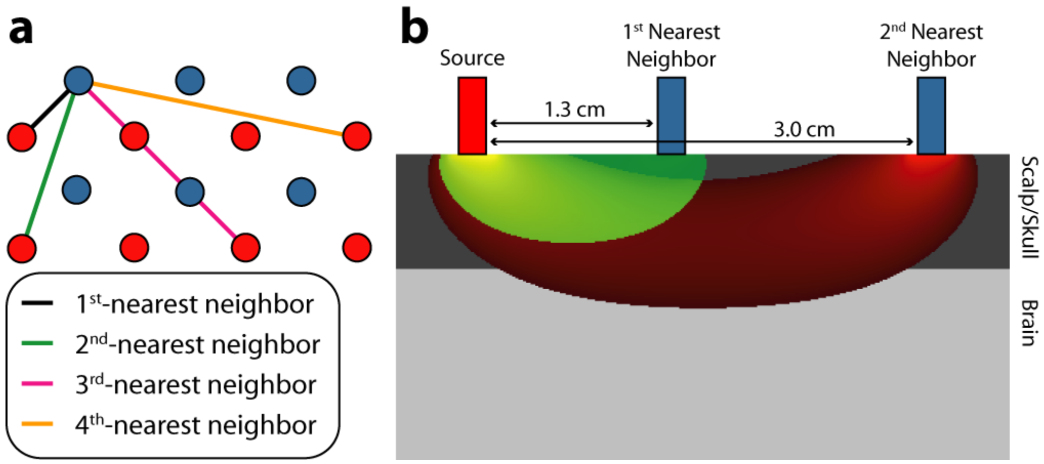

Figure 2.5: Definitions of nearest neighbor measurements. (a) A subset of our high-density DOT optode array showing how 1^{st}- through 4^{th}-nearest neighbors are defined. (b) Slices through a semi-infinite simulation of photon flow for 1^{st}- and 2^{nd}-nearest neighbor separation. We see that 1^{st}-nearest neighbors are sensitive mostly to scalp and skull, while 2^{nd}-nearest neighbors sample into the brain.

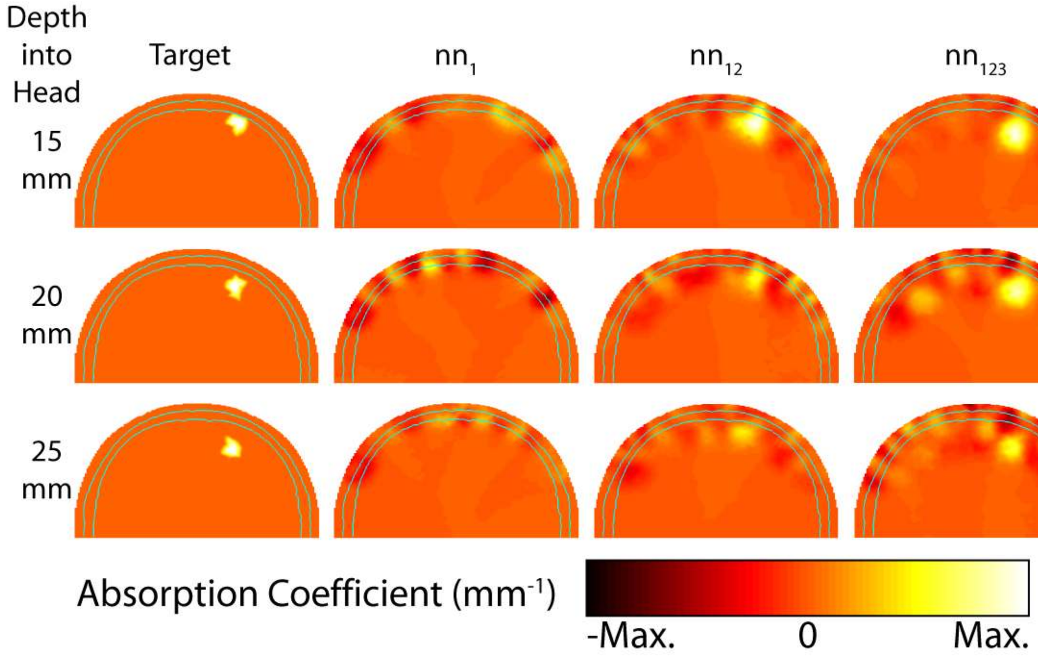

Figure 2.6: Depth sensitivity of optode arrays. Simulations performed in a model of the human head of target reconstructions at different depths (axial slices are shown). Using only 1st-nearest neighbors we can reconstruct no brain activations (as expected from Fig. 2.5). 2nd- and 3rd-nearest neighbors allow reconstructions deeper into the brain. Using measurements with further source-detector separations improves imaging performance at increasing depths.

frequencies (frequency encoding). Since distant sources are unlikely to be detected above the noise floor of the detectors, two sources can be co-illuminated as long as there are no detectors near both (spatial encoding). In practice, each optode array is divided into twelve-source regions. At any given time, one position is illuminated within each region (regions are spatially encoded). Temporal and frequency encoding are used within a region (the different regions are additionally encoded at different frequencies for further differentiation). The full encoding arrangement is currently configured for a frame rate of 10.79 Hz. Faster frame rates are possible, but (as no vascular physiology is expected above the heart rate of ≈ 1 Hz) are unnecessary.

Source illumination is provided by light-emitting diodes (LEDs) at 750 nm (750-03AU, Roithner Lasertechnik) and 850 nm, (OPE5T85, Roithner Lasertechnik). The LEDs are controlled digitally with dedicated, high-bandwidth (20 MHz) digital input/output lines (PCI-6534, National Instruments). This software encoding allows illumination patterns to be flexible and adaptable for different optode pad configurations. The illumination power averages 0.2 mW at each wavelength for each source position, which is well below ANSI limits.

Both sources and detectors are coupled to the head with fiber bundles measuring 3 mm diameter and 4 m in length. The optode array is held in place using a flexible plastic cap, fastened around the subject's head with Velcro straps.

At each detector, we need to be able to detect this light with the performance requirements discussed above, placing stringent benchmarks on the system engineering. Detecting brain activations at depth necessitates high signal-to-noise. And, detection of light from multiple source-detector separations requires high dynamic range ($> 10^6$) and low crosstalk ($< 10^{-6}$). To achieve these requirements, each detector channel has a dedicated avalanche photodiode (C5460-01, Hamamatsu), with decreased gain in order to improve dynamic range. Each detector is digitized by a dedicated 24-bit analog-to-digital converter chip (HD192, MOTU). This system is capable of detecting light from first- through fourth-nearest neighbors well-above the noise floor (Fig. 2.7).

After detection, data can either be spooled directly to a hard disk at a sampling rate of 96 kHz or decoded in real-time. Decoding consists of determining which detected light came from which source. A synchronization trigger allows light at each time within a frame to be assigned to particular detectors (removing the temporal encoding). Amongst the LEDs that are co-illuminated, digital lock-in detection undoes the frequency encoding, and light is assigned to the nearest source that was on (to remove spatial encoding).

2.3 Analysis

2.3.1 Overview

The goal of DOT data processing is to convert raw source-detector intensity time traces, $I(t)$, into images of concentration changes of hemoglobin species in the cortex. This process consists of two major steps. First, source-detector time traces are filtered an de-noised. Then, each measurement time is converted to an image of concentration change using the inverse model discussed above (Section 2.1.4). Additionally, data is resampled from the initial sampling rate ($>$ 10 Hz) to the desired sampling rate for analysis (often 1 Hz). A schematic of this process is shown in Figure 2.8. The software that controls these steps is described in Appendix C.

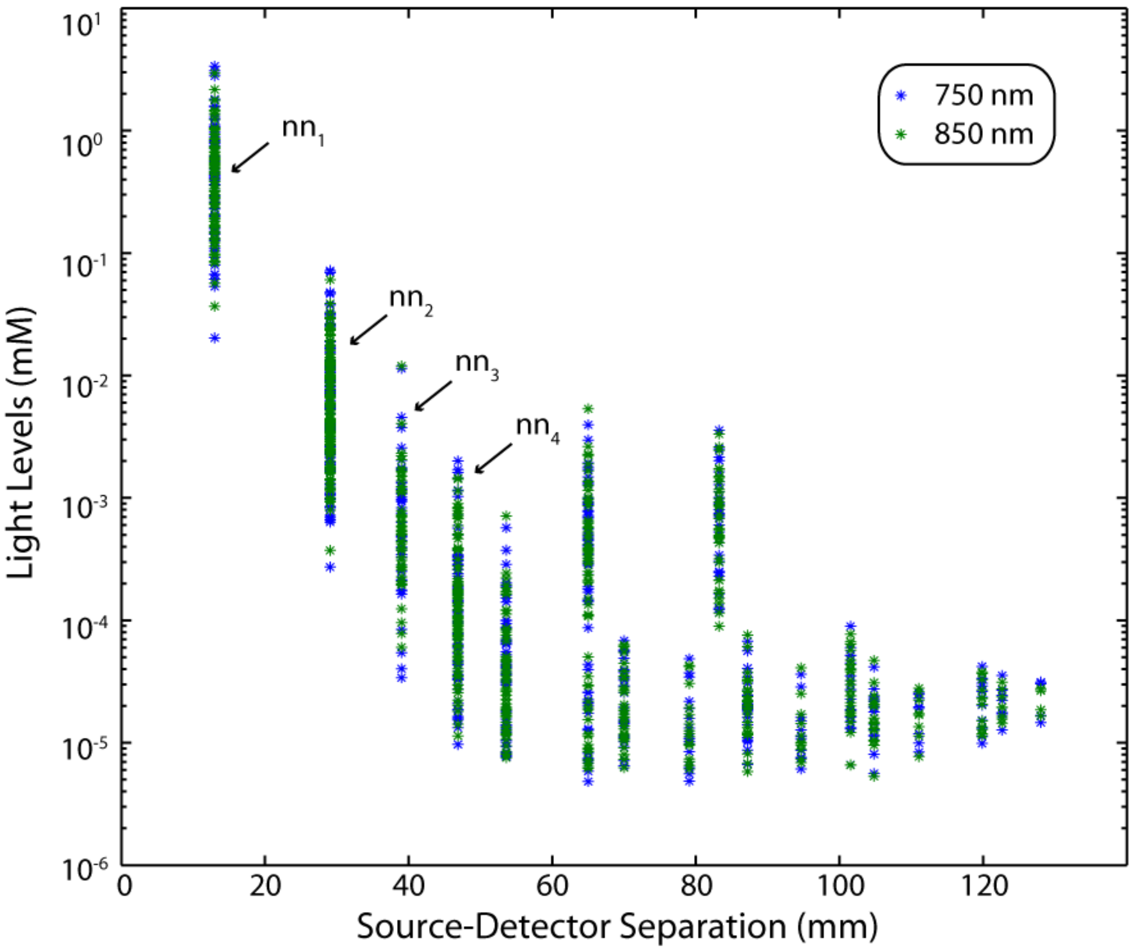

Figure 2.7: Light fall-off with source-detector distance. As source-detector distance increases, the power detected falls off approximately exponentially, until we reach the noise floor (at ≈ 10 pW). The large spread at each separation is due to differences in coupling between optodes and the head (this variation in baseline measurements is one reason why differential measurements improve signal-to-noise). The high levels at 6^{th}- and 9^{th}-nearest neighbors are due to cross-talk between spatial encoding regions; however, as we never use these measurements in reconstructions, this artifact is not a problem.

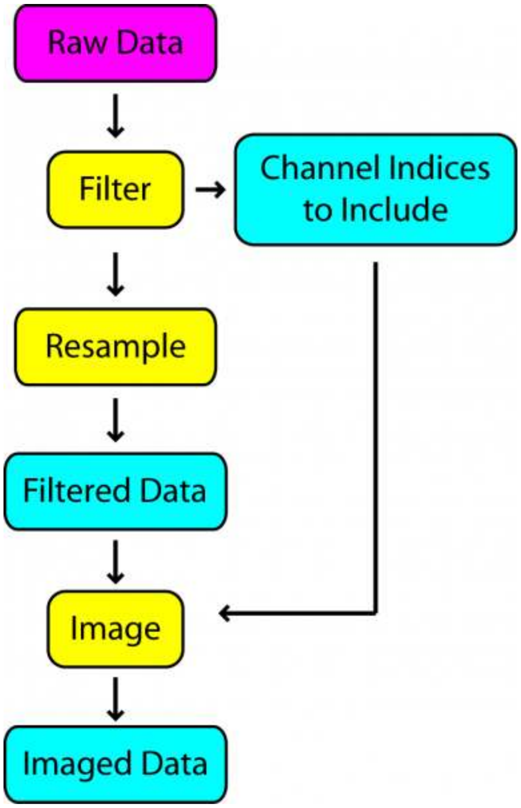

Figure 2.8: Overview of data processing. Raw source-detector data is filtered, resampled, and imaged. Along with this process, a list of noisy channels is kept, so that these measurements can be excluded from analysis and reconstruction. The outputs highlighted in blue are saved for post-processing and display.

2.3.2 Filtering

An overview of the filtering process is given in Figure 2.9. The first step is to convert intensity time traces to differential intensity (absorbance) measurements consistent with the Rytov approximation (Eq. 2.21):

$$y_i(t) = \Delta I_i(t) = -\ln \frac{I_i(t)}{\langle I_i(t) \rangle} \tag{2.47}$$

Here, i is the index of the source-detector pair, and $y_i(t)$ is our notation for the i^{th} source-detector measurement, and $I_i(t)$ is the detected intensity of this measurement (equivalent to the photon fluence, Φ_i, used earlier). Note that in the original definition of the Rytov approximation (Equation 2.31) $I_i(t)$ is normalized by the unperturbed (baseline) light intensity ($I_{0,i}(t)$). However, it often inconvenient or impossible to conduct a baseline measurement (e.g., when performing phase-encoded retinotopic paradigms, where the stimulus is always present, or when performing resting-state measurements, where intrinsic activity means there is no baseline state). Thus, we normalize our measurements by the average intensity over the length of the scan. As this change only results in a linear offset, it can easily be corrected later if one wishes to revert to measurements relative to a truer baseline.

At this point, we take the standard deviation of every channel. Those with high standard deviation (≥ 0.075, which is essentially equivalent to an original intensity standard deviation of 7.5%) are noted. These channels will be removed from further analysis, both in the construction of the superficial regressor and in the image reconstruction. An average 1$^{\text{st}}$-nearest neighbor had a standard deviation of 1.3% and an average 2$^{\text{nd}}$-nearest neighbor, 2.4% (with 1% of the latter being due to the desired activation); so, this three standard deviation threshold can exclude abnormally large variations while preserving normal physiology. Within a range, the reconstruction is relatively insensitive to the exact threshold chosen. A typical run keeps 98.9% of 1^{st}-nearest neighbors, 96.4% of 2^{nd}-nearest neighbors, 59.1% of 3^{rd}-nearest neighbors, and 19.0% of 4^{th}-nearest neighbors. Thus, the analysis is primarily dependent on 1st- and 2^{nd}-nearest neighbors, while 3^{rd}- (and to a lesser extent 4^{th}-) nearest-neighbors provide additional depth information when possible.

Every measurement channel is filtered to remove low-frequency drift and high-frequency noise. The low-pass filter is usually set at 2 Hz, which removes any instrument noise while maintaining pulse and respiration physiology. The cut-off frequency of the high-pass filter depends on the study design. For task-paradigm studies, where low-frequency physiology is unwanted noise, the filter is set at 0.02 Hz. For resting-state studies, where the goal is to study fluctuations below 0.1 Hz, the cut-off frequency is 0.009 Hz.

Since every measurement consists of light that has gone through the scalp, skull, and brain, what we actually detect is a mixture of hemodynamics occurring in all of these layers. To remove artifacts from superficial layers, we take advantage of the fact that high-density DOT systems measure light from multiple source-detector distances (Fig. 2.5). Measurements where the source and detector are located close to each other (in our system, 1^{st}-nearest neighbors) primarily sample superficial tissues, while longer source-detector separations (2^{nd}- through 4^{th}-nearest neighbors) sample deeper into the brain. Thus, superficial noise can be removed from deeper measurements by linear regression of the signal from shallow measurements (termed superficial signal regression, SSR) [Saager and Berger, 2005, 2008, Zeff et al., 2007]:

$$y_{\text{out},i}(t) = y_{\text{in},i}(t) - y_n(t)\frac{\langle y_{\text{in},i}(t), y_n(t)\rangle}{\|y_n(t)\|^2} \tag{2.48}$$

$y_{\text{in},i}$ is the i^{th} measurement time trace before filtering and y_n is the measure of superfi-

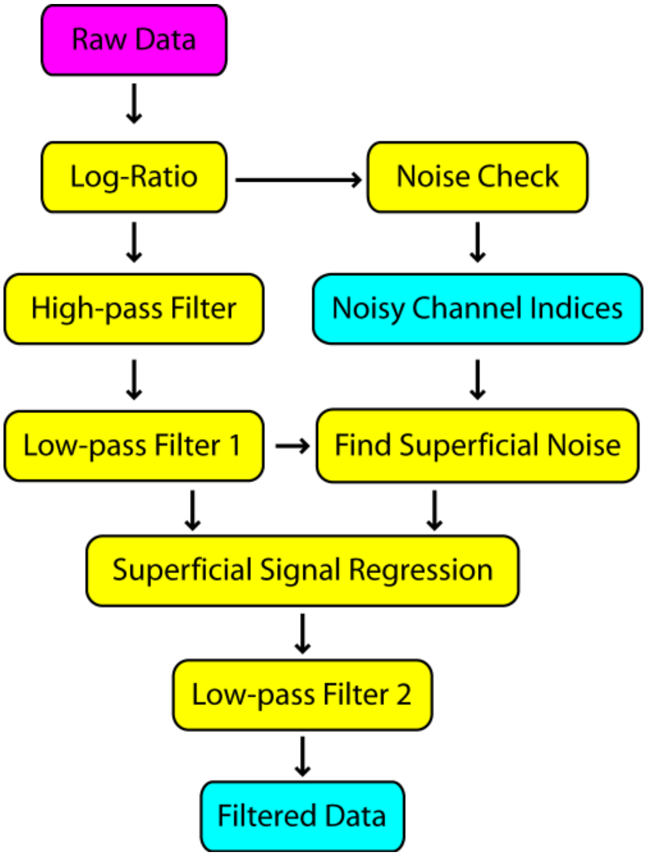

Figure 2.9: Overview of data filtering. Raw source-detector intensities (input in purple) are converted to Rytov approximation differential measurements. The first step is to find channels that have standard deviation above 0.075 so that they can be removed from future steps. Various filtering steps remove pulse and low-frequency noise. Additionally, 1^{st}-nearest neighbors are averaged to create a superfical noise signal that is regressed from all measurements to give a truer picture of brain hemodynamics.

cial noise derived. We construct our superficial regressor from all 1^{st}-nearest neighbor source-detector measurements within an optode array that passed the earlier noise threshold:

$$y_n(t) = \sum_{i \in nn_1} y_i(t) \tag{2.49}$$

This procedure drastically increases the contrast-to-noise of task-induced activations in the measurement time traces (Fig. 2.10) [Gregg et al., 2010].

At this point, a second low-pass filter is performed, with a cut-off frequency of 0.5 Hz to remove the remaining noise from pulse. After filtering, the data is usually resampled from the original scan rate (presently 10.79 Hz) to a more standard time base, often 1 Hz.

2.3.3 A-Matrix Construction

While analytical semi-infinite solutions to the diffuse approximation to the RTE can be used for neuroimaging, such a geometry is a poor model of the human head. Thus, we choose to model light flow using a two-layer hemispherical model. While, overall, the head is not a sphere, this model is appropriate over limited fields-of-view (e.g., the visual or motor cortices). As an analytical solution can not be found in this geometry, we use a finite element model program for near-infrared light flow, NIRFAST [Dehghani et al., 2003].

The adult head model has an outer radius of 80 mm with a 10 mm scalp/skull outer layer surrounding the brain. Optical properties (absorption coefficient, μ_a, and reduced scattering coefficient, μ_s') for the two layers were obtained from the table given in Strangman et al. [2003] using linear interpolation to the desired wavelength (Table 2.1).

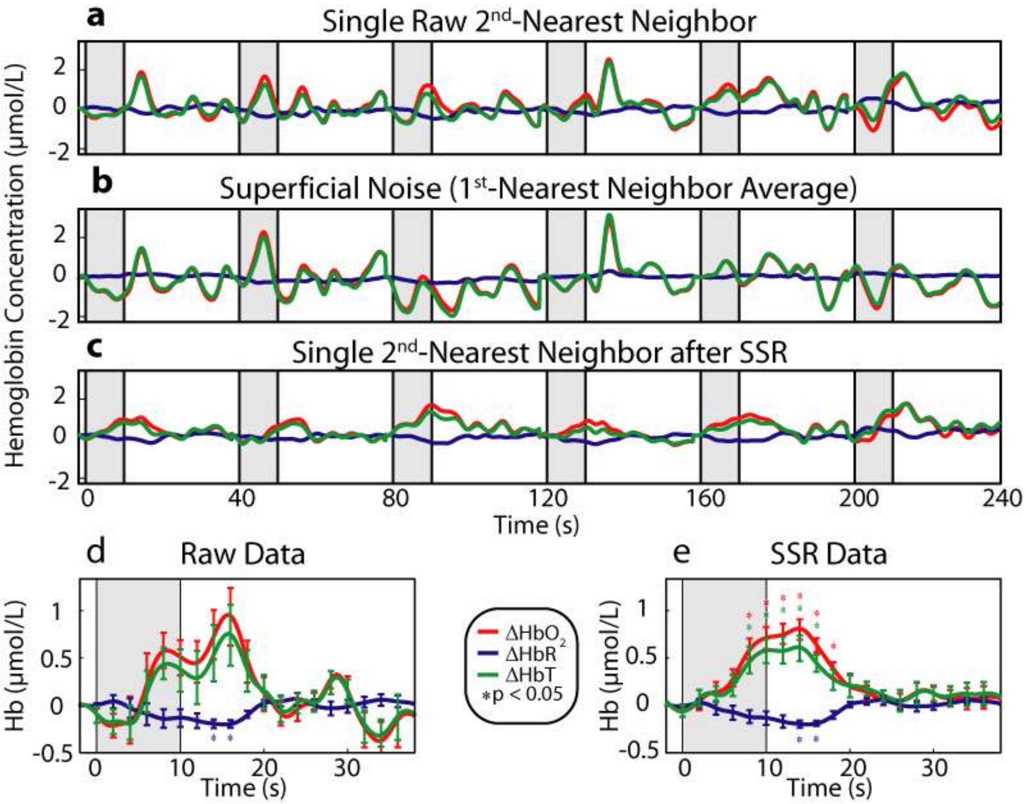

Figure 2.10: Improvements in CNR from superficial signal regression (SSR). The gray shaded regions indicate visual stimulus. (a-c) Time traces of the hemodynamic response to six blocks of stimulus with HbO_2 in red, HbR in blue, and HbT in green. The superficial noise signal (b) is regressed from a raw 2nd-nearest neighbor source-detector pair (a), producing noise-regressed data (c). Note the consistent clean shape after superficial signal regression (SSR). (d-e) Block-averaged time traces of (a) and (c), respectively. Error bars mark standard deviation and asterisks indicate statistically significant deviations from baseline. Note the reduced noise and improved CNR of the activation after SSR.

Table 2.1: Optical properties of the two-layer head model

	μ_a (cm^{-1})		μ_s' (cm^{-1})	
Tissue Layer	750 nm	850 nm	750 nm	850 nm
Scalp/Skull	0.15	0.17	8.4	7.4
Brain	0.19	0.19	12	11

The optode grids (as described in Section 2.2), which are originally defined in two dimensions, were conformed to the hemispherical model preserving distance and angle between each optode and the center point of the grid, which was located at the apex of the hemisphere. NIRFAST generated Green's functions for the sensitivities of each source and detector. These Green's function were converted from the tetrahedral geometry of the finite element model to a voxelized space (voxels were cubic with a side length of 2 mm) and cropped to the region with high sensitivity (e.g., for the adult visual cortex: 140-mm width, 80-mm height, 48-mm depth, for a total of 67,200 voxels: $70 \times 40 \times 24$).

Sensitivity matrices, A, for each array were constructed using the adjoint formulation and normalized consistent with the Rytov approximation (Equation 2.34).

2.3.4 Imaging

Once as many artifacts have been removed from the source-detector data as possible, the data is imaged following the theoretical procedures outlined above (Section 2.1). Both the measurements and the A-Matrix are cropped to just the measurements that will be used in the reconstruction, r (i.e., the intersection of the measurements that passed the noise threshold, g, and the nearest neighbors to use, usually either nn_{12} or nn_{1234}):

$$r = g \cap nn_{12 \text{ or } 1234} \tag{2.50}$$

Note that while a time trace of the average across channels of all 1st-nearest neighbor pairs was removed during the superficial signal regression (Eq. 2.48), the individual 1st-nearest neighbor channels retain variance after this regression and are used during the reconstruction.

This forward model is directly inverted for image reconstruction as in Equation

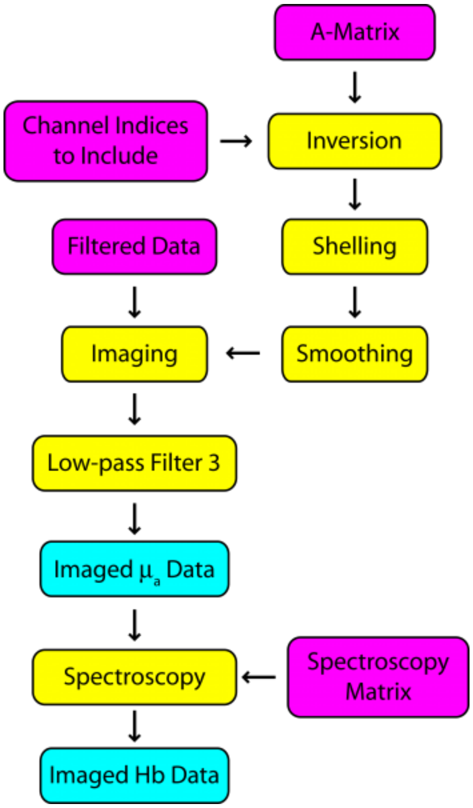

Figure 2.11: Overview of data reconstruction. First the A-matrix is prepared; after cropping to just the useful measurements, inversion is performed with Tikhonov and spatially-variant regularization. Imaging is performed with this A-matrix restricted to a cortical shell. Imaged data can be low-pass filtered (used only with resting-state data at the moment). Then, spectroscopy converts voxels of absorption coefficient change to voxels of hemoglobin concentration changes. Imaged $\Delta\mu_a(\mathbf{r})$ and $\Delta\mathrm{Hb}(\mathbf{r})$ data are saved for visualization.

2.43. For task-paradigm studies, the Tikhonov regularization constant is usually chosen to be $\lambda_1 = 10^{-2}$. For resting-state studies and infant studies with lower signal-to-noise, $\lambda_1 = 10^{-1}$ is used. For all *in vivo* studies, a spatially-variant regularization constant of $\lambda_2 = 10^{-1}$ was used.

As we were interested in hemodynamic responses within the cortex, we selected a cortical shell (1 cm thickness) from within our 3D A-matrix and averaged across the thickness of the shell. Note that this is different from a cortically-constrained reconstruction, since the cortical region is chosen after rather than before inversion. While this shell is thicker than the actual layer of gray matter, the depth resolution of the system (≈ 1 cm) means that the generated images are relatively insensitive to the thickness chosen as long as the shell excludes the superficial layer directly beneath the optodes and deep layers where the sensitivity of the measurements is low. All HD-DOT images displayed are posterior coronal projections of this cortical shell (i.e., we have averaged along the anterior-posterior axis), resulting in a point-of-view as if looking at the head from behind with the skin and skull removed (Fig. 2.12). The shelled A-matrix was then smoothed with a Gaussian kernel (5×5 pixel box, standard deviation 1.2 pixels).

The inverted A-matrix then multiplies the source-detector measurements to create maps of changes in the absorption coefficient at each wavelength (Eq. 2.45). Note that these steps are performed separately for each wavelength as the measurements that pass the noise threshold need not be identical between the two wavelengths. The imaged data is then (optionally) low-pass filtered; this filter is generally only performed with functional connectivity analysis, to remove components above 0.08 Hz.

Images of absorption change at each wavelength of light can be converted to changes in the concentrations of hemoglobin species, using their extinction coefficient

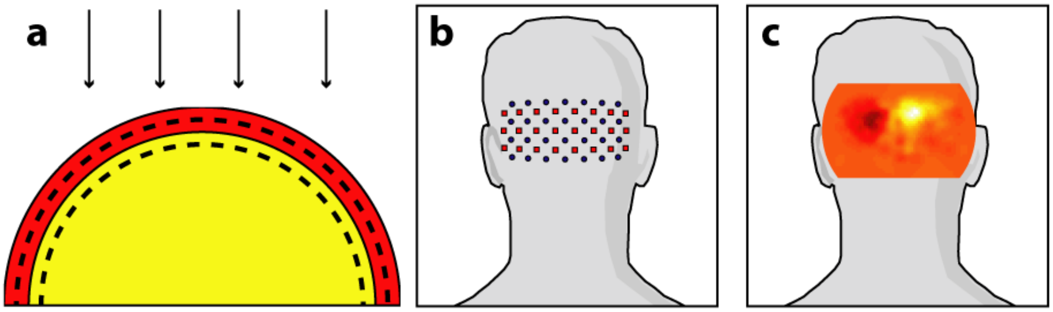

Figure 2.12: Location of the cortical shell for visualization. (a) A schematic of the hemispherical head model with brain (yellow) and scalp/skull (red). The cortical shell is shown in dashed lines, and the direction of projection is shown with arrows. (b) Schematic of the visual grid placed over the back of a human head. (c) A reconstruction placed over the head after shelling to show direction of view.

(Fig. 1.1).

$$\begin{aligned} \mu_{a,750} &= \varepsilon_{HbO_2,750}[\mathrm{HbO_2}] + \epsilon_{HbR,750}[\mathrm{HbR}] \\ \mu_{a,850} &= \varepsilon_{HbO_2,850}[\mathrm{HbO_2}] + \epsilon_{HbR,850}[\mathrm{HbR}] \end{aligned} \tag{2.51}$$

This can be rewritten in matrix format:

$$\begin{bmatrix} \mu_{a,750} \\ \mu_{a,850} \end{bmatrix} = \begin{bmatrix} \varepsilon_{HbO_2,750} & \varepsilon_{HbR,750} \\ \varepsilon_{HbO_2,850} & \varepsilon_{HbR,850} \end{bmatrix} \begin{bmatrix} [\mathrm{HbO_2}] \\ [\mathrm{HbR}] \end{bmatrix} \tag{2.52}$$

Or, more simply:

$$\mathbf{x}_{\mu_a} = \mathbf{E}\mathbf{x}_{Hb} \tag{2.53}$$

Thus, we can create images of hemoglobin concentration change with a simple matrix inversion:

$$\mathbf{x}_{Hb} = \mathbf{E}^{-1}\mathbf{x}_{\mu_a} \tag{2.54}$$

Images of total hemoglobin (HbT) can be created by summing those for HbO_2 and HbR. Generally, our purpose was not to find differences between these different contrasts. Thus, for simplicity, I will usually show images of one contrast. The images in the other contrasts are qualitatively similar.

Chapter 3

Improving Optical Imaging Performance through Tomography

3.1 Introduction

Near-infrared spectroscopy (fNIRS) holds the promise to extend functional neuroimaging methods into new settings, such as the assessment of brain function in clinical patients unable to be transported for functional magnetic resonance imaging (fMRI). However, the successful transition of optical techniques from intriguing concept to useful neuroscience tool has been hampered by difficulties in acquiring measurements through the scalp and skull. The standard fNIRS method of acquiring arrays of sparsely distributed measurements has limited spatial resolution and irregular spatial sensitivity, resulting in subsequent mislocalization of cortical hemodynamics. Initial simulation studies of high-density diffuse optical tomography (HD-DOT) have shown potential improvements for neuroimaging in both resolution and localization errors [Boas et al., 2004, Joseph et al., 2006]. In our human brain mapping studies, we have shown that HD-DOT studies have been able to generate detailed activation maps

[Zeff et al., 2007, White et al., 2009, White and Culver, 2010a]. However, the link between theoretical comparisons and *in vivo* results remains circumstantial. In this chapter, I provide a thorough evaluation of the abilities of sparse fNIRS and HD-DOT in simulation. This comparison will be continued through *in vivo* cortical mapping in the following chapter (Sections 4.2.4 and 4.2.5). This analysis will consist of three parts: (1) a comparison of resolution and localization errors in dense and sparse diffuse optical imaging using point-spread functions (this chapter); (2) simulations of more realistic activation patterns similar to those seen *in vivo* (Section 4.2.5); and (3) *in vivo* cortical mapping using both the HD-DOT system and a sparse subset of the same imaging array (Section 4.2.4) [White and Culver, 2010b].

Since near-infrared sources and detectors generally need to be displaced by approximately 3 cm in order for the sensitivity function to have significant brain sensitivity, this separation becomes a primary factor limiting spatial resolution. HD-DOT systems use a grid of overlapping source-detector measurements to allow multiple measurements within each voxel of the imaged volume. This technique provides better spatial sampling and a more robust approach to image reconstruction, which in turn provides better localization and resolution of the imaged activations. The goal of the present work is to provide multiple analyses that quantitatively evaluate the imaging improvements possible with HD-DOT. First, we examine standard simulation metrics in order to understand the ideal performance of multiple fNIRS systems in current use.

Both simulations and human data will show that sparse optode arrangements are unable to provide high enough image quality to perform detailed neuromapping studies, such as retinotopy, that move beyond individual activations to resolving the patterns cortical organization. In contrast, I will show that HD-DOT has superior performance and is able to reproduce expected *in silico* performance during *in vivo* applications.

3.2 Methods

3.2.1 Optode Arrangements

In order to test the performance of various fNIRS optode grids for *in vivo* brain imaging, I created three arrangements of sources and detectors. The first array was a standard square sparse array of interleaved sources and detectors (Fig. 3.1a; 7 sources and 8 detectors for 22 total measurements), which is the most commonly used fNIRS geometry. The second array was a second sparse array using a line of sources flanked by two rows of detectors (Fig. 3.1b; 8 sources and 14 detectors for 28 total measurements), which is another commonly used arrangement with the goal of increasing resolution along one axis. (We will refer to this arrangement as the triangular sparse array.) The third array was our high-density grid developed for the visual cortex (Fig. 3.1c, same as Fig. 2.4; 24 sources and 28 detectors for 212 1^{st}- and 2^{nd}-nearest neighbor measurements). For visualization, we display a smaller, centered field-of-view selected from the entire imaged area, measuring 102 mm width and 50 mm height in order to focus on the regions under the arrays with the highest sensitivities and lower image artifacts. This region is shown in Fig. 3.1 by the black dashed lines.

3.2.2 Simulation and Point-Spread Function Analysis

Point-spread functions (PSFs) were created by simulating a perturbation at a single point. The simulated absorption perturbation,$\mathbf{x}_{sim}$, is a vector of zeros except for one

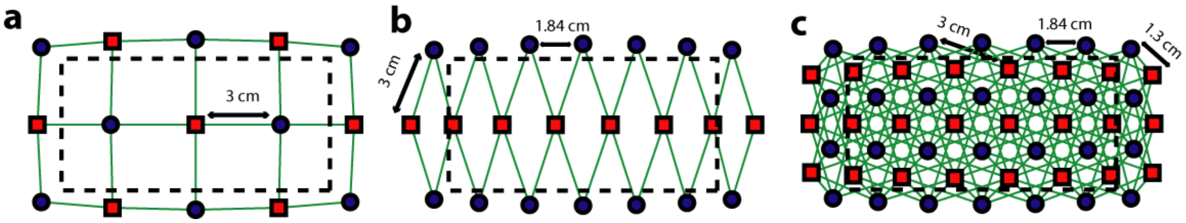

Figure 3.1: Diffuse optical imaging optode arrays for simulation. Sources are red squares, detectors are blue circles, and measurements are green lines. (a) Schematic of the square sparse imaging array. The 2D grid with 3-cm spacing was conformed to an 8-cm-radius sphere. Shown is a projection of the resulting 3D optode locations. (b) Schematic of the triangular sparse imaging array. (c) Schematic of the high-density imaging array (as in Fig. 2.4). The black box shows the region of interest for the simulation analyses.

target pixel with a value of one. I then generated simulated measurements:

$$\mathbf{y}_{sim} = \mathbf{A}\mathbf{x}_{sim} \tag{3.1}$$

And, I reconstructed an image:

$$\mathbf{x}_{recon} = \tilde{\mathbf{A}}^{\#}\mathbf{y}_{sim} \tag{3.2}$$

With this particular choice of $\mathbf{x}_{sim}$, this is equivalent to examining a row from the matrix $\tilde{\mathbf{A}}^{\#}\mathbf{A}$ (known as the resolution matrix). For this analysis, I removed the confounding influence of spatially-variant regularization, so $\mathbf{A}$ was inverted as in Eq. 2.39. For simplicity, all images shown were made using the 850 nm A-matrices. Note that I do not explicitly include noise in the simulated data. However, I do set the regularization based on *in vivo* imaging. Thus, the reconstructed images implicitly reflect the smoothing necessary to accommodate real-world measurement noise. Working with noiseless simulated data allows us to focus the image quality evaluations on the systematic modeling and data sampling errors. The evaluation of image quality in the presence of noise is addressed in full with the *in vivo* data evaluations.

I now set about charactering the resulting PSFs. Since the sparse arrays often reconstruct asymmetric and elliptical responses, using the square root of the area above half maximum to construct a full width at half maximum (FWHM) tends to be a poor measure of a responses characteristic length. Thus, I defined FWHM as the maximum separation between all pairs of points in the activation, which is a lower bound on the diameter of a circle needed to completely enclose the activation (Fig. 3.2a). Another standard image metric is the localization error, defined as the distance between the centroid of the response and the known location of the target (Fig. 3.2b). In neuroscience applications where the location of the activation is unknown, mislocalization and an overly large activation are both equivalent in that they cause brain hemodynamics to be measured where none actually occurred. Thus, we combined these two image metrics into a single effective resolution defined as the diameter of a circle centered at the known perturbation position needed to enclose the entire activation (Fig. 3.2c), which should more closely characterize expected *in vivo* performance.

3.3 Results

I analyzed the point-spread functions (PSFs) for every pixel within our imaging domain (Video 3.1). Moving the target activation point sequentially through the domain showed that the dense array was able to reconstruct the response with good localization and a slightly blurred but symmetric PSF. Both sparse arrays displaced activations to the nearest area of high sensitivity (i.e., onto the line between the nearest source-detector pair). These errors can result in the reconstructed responses to

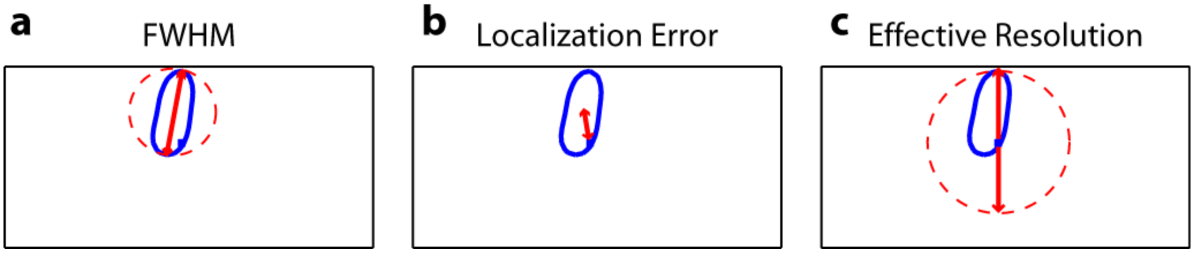

Figure 3.2: Definitions of imaging metrics for point-spread function analysis, shown using a simulated image reconstruction from the triangular sparse array. The target perturbation is the blue square, and the contour at half-maximum of the reconstruction is the blue line. (a) Full width at half maximum (FWHM) is defined as the maximum separation between any two points above half maximum in the reconstruction (red arrows). This is a lower bound on the diameter of a circle needed to enclose the reconstruction (red circle). (b) Localization error is the separation of the known target position and the centroid of the reconstruction (red arrows). (c) Effective resolution is the diameter of a circle centered at the known target position needed to enclose all points above half maximum in the reconstruction (red circle and arrows).

multiple targets appearing either artificially far apart upon inversion (Fig. 3.3a-c) or nearly identical despite large true separations (Fig. 3.3d-f).

Additionally, while the triangular sparse array performs well in horizontal localization, it has essentially only two voxels vertically: it is binary, placing responses either above or below the center source line with no further discrimination. Both sparse arrays have multiple lines of symmetry, points that fall equidistant between two measurements. The location of activations at these points cannot be distinguished and are projected equally into the two measurements, resulting in large reconstructed responses. One particularly notable symmetry is along the source line in the triangular sparse array; a target directly beneath this line is reconstructed as a large vertical activation stretching the entire height of the pad.

Image errors can be quantified using standard metrics of imaging performance (Tables 3.1 and 3.2). The size of the reconstructed response is measured with the full effective width at half maximum (FWHM) of each targets point-spread function

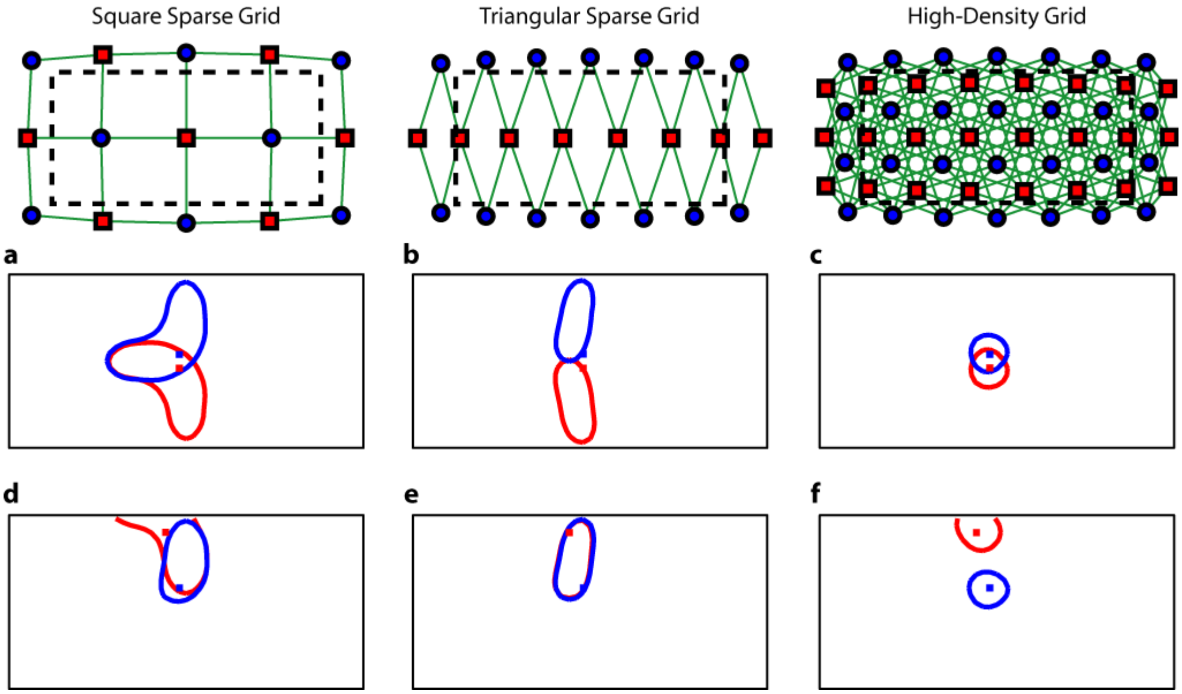

Figure 3.3: Representative image performance of sparse and high-density arrays. Targets are shown as red and blue squares. Half-maximum contours of the reconstructed responses are shown with the appropriately colored lines. (a-c) Here, two targets have been placed 4 mm apart adjacent to the horizontal midline of the arrays. The high-density array can correctly place the responses with a relatively small PSF (separation 4.4 mm). However, the triangular sparse array artificially displaces the two reconstructions (separation 23.2 mm) and enlarges the PSFs. The square sparse array results in reconstructions with an L-shape, which gives a large activation size, but reasonably close placement of the centroids (separation 11.5 mm). (d-f) Here, two targets have been placed far apart (separation 16.5 mm). Although the triangular sparse array reconstructs them as superimposed (separation between centroids of only 0.6 mm), the high-density array correctly separates them (17.5 mm). The square sparse array again reconstructs one of the activations in an L-shape, resulting in intermediate separation values (8.2 mm) with a large response size.

(Fig. 3.4a-c). Displacement of the response from the target point is calculated using localization error (Fig. 3.4d-f). Since both broadening and misplacement of activations are similar in the sense that they both cause reconstructed responses where no activity should be measured, we combined resolution and localization error into a single metric of effective resolution, defined as the diameter of a circle centered at the known target location needed to enclose all activated points above half maximum (Fig. 3.4g-i). Judging by all three metrics, the high-density system has two advantages over the sparse arrays. First, the average image quality is higher (an improvement of 1.76× in FWHM, 5.4× in localization error, and 2.27× in effective resolution). Second, this high performance is relatively even over the entire field-of-view. The performance maps of the sparse arrays alternate between areas of good and poor quality. Since most brain activations have an extent on the order of 1 cm, it is likely that sparse arrays will perform only up to the quality of their worst pixel.

Table 3.1: Examination of PSFs of sparse and dense fNIRS arrays (mean ± standard deviation).

Array	FWHM (mm)	Localization Error (mm)	Effective Resolution (mm)
Square Sparse	21.6 ± 4.6	5.3 ± 2.0	29.9 ± 5.2
Triangular Sparse	20.9 ± 4.3	5.4 ± 3.6	31.7 ± 7.1
High-Density	12.1 ± 1.4	1.0 ± 0.9	13.5 ± 2.2

Table 3.2: Performance ranges for PSFs of sparse and dense fNIRS arrays (minimum to maximum).

Array	FWHM (mm)	Localization Error (mm)	Effective Resolution (mm)
Square Sparse	14.6 – 42.0	0.4 – 10.7	16.5 – 44.2
Triangular Sparse	16.5 – 48.2	0.0 – 13.5	16.5 – 48.2
High-Density	8.2 – 17.2	0.0 – 5.8	8.9 – 25.3

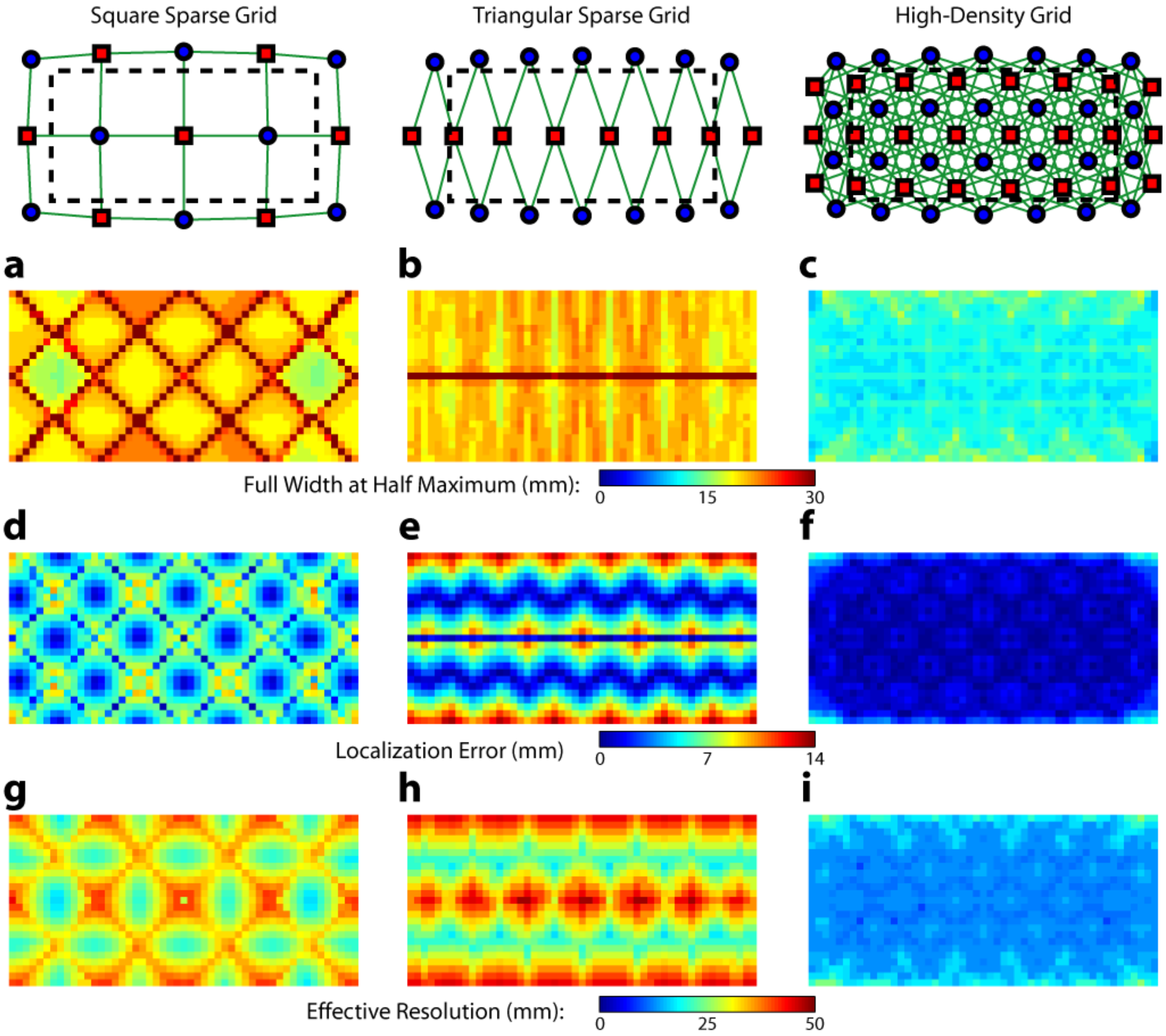

Figure 3.4: Image quality metrics for the point-spread functions of targets placed at every location in sparse and high-density grids. (a-c) Full width at half maximum of the imaging arrays. For the sparse arrays, there is overall poor resolution (high FWHM) with worse resolution along lines of symmetry in the grid geometry. Also, note that the triangular array has the worst resolution directly beneath the source line, where the system cannot constrain the activation vertically. The resolution for the high-density array is high (low FWHM) across the entire imaging domain with little variation. (d-f) Localization error of the imaging arrays. While the sparse arrays have low localization error directly under measurements and along points of symmetry, between measurements it is high. Localization error for the high-density array is uniformly low across the entire field-of-view. (g-i) Effective resolution of imaging arrays. The sparse arrays have poor effective resolution between the measurements, and only good effective resolution directly between adjacent sources and detectors. Effective resolution for the high-density array is good across the entire imaging domain, with little variation.

3.4 Discussion

I have conducted a quantitative comparison of the imaging performance of multiple imaging arrays for diffuse optical imaging. The goal of this exercise was to evaluate the potential improvements in image resolution and localization error of HD-DOT over sparse imaging geometries in the context of detailed *in vivo* neuroimaging tasks. This work builds on previous literature that has evaluated the theoretical performance of neuroimaging DOT systems. Boas et al. [2004] analyzed the resolution and localization error of a square and a hexagonal HD-DOT grid. In contrast to this paper, both grids were high-density, and the subject of the comparison was the use of back-projection versus tomographic imaging techniques. Similarly, Joseph et al. [2006] demonstrated qualitative improvement of performing tomography over using single source-detector distances within the context of an HD-DOT array and simple focal activations. Since no sparse array was included in the comparison, it is difficult from those results to judge possible improvements over the sparse arrangements that are in wide-spread current use. Additionally, these studies have two algorithmic limitations: they assume a semi-infinite head geometry, and the reconstructions are depth-constrained to a plane with a known perturbation location. These assumptions limit translation of the simulations to evaluating neuroscience results.

My analysis judged three imaging geometries based on their performance on standard metrics of image quality. These simulations yield a FWHM of 12 mm for the high-density array and 21 mm for the two sparse arrays. Boas et al. [2004] report their resolution using characteristic areas: 2.0 cm^2 for high-density DOT and 4.5 cm^2 for a back-projection. (This is not the same as using a sparse grid, but it serves as a useful comparison for our results.) Converting our characteristic diameters to areas yields 1.1 cm^2 for high density and 3.5 cm^2 for sparse. Assuming similar regularization, my simulation might have higher resolution since I used 1$^{\text{st}}$-nearest neighbor separations of 1.3 cm and 2$^{\text{nd}}$-nearest neighbor separations of 3.0 cm, compared to 1.9 cm and 4.25 cm for the Boas et al. study. Additionally, my work shows the high-density array to have much better localization error than sparse arrays, 1.0 mm versus 5.3 mm. Boas et al. measured localization errors of 2 mm for DOT versus 5 mm for back-projection.

While activation size and mislocalization can be easily separated in simulations since the target is known *a priori*, this rigor does not translate to *in vivo* separations. When performing a brain activation study, the goal is to locate the area of the brain that responds preferentially to a given stimuli. This challenge is especially problematic with sparse arrays, which mislocalize many different, widely separated areas to the same area of high sensitivity. From a neuroimaging perspective, it is equivalent if two distinct areas are superimposed due to a broad reconstruction or due to them both being artificially displaced to the same area. Since optical neuroimaging systems currently sample only superficial regions of cortex, their brain sensitivity jumps from gyri to gyri. Thus, seemingly small mislocalizations laterally can actually result in large errors in terms of position along the 2D cortical surface. So, to combine knowledge of FWHM and localization error into a single metric of expected *in vivo* performance, I used the effective resolution (the diameter of a circle centered at the known activation point needed to circumscribe all voxels above half-maximum contrast). The high-density array has an effective resolution of about 1.3 cm, which should prevent identification to the wrong gyrus. However, the sparse arrays both have effective resolutions greater than 3 cm (as expected heuristically based on their source-detector separations).

Since one of the main benefits of optical technology is its potential to translate to a bedside neuroimaging tool, it is important to develop techniques that can perform effectively in neuromapping paradigms in single subjects. Noninvasive optical techniques have spatial resolution between fMRI and EEG. While improvements such as high-density arrays are unlikely to result in image quality that surpasses the high resolution of fMRI, improving image quality is always a fundamental goal, allowing researchers to access the advantages of optical neuroimaging (e.g., portability and comprehensive hemodynamic measurements) without being hampered by insufficient imaging performance. A reasonable objective within the field of neuroimaging is 1 cm resolution, which would allow the distinguishing of gyri and the ability to perform classical human brain mapping paradigms, such as retinotopy. My results show that common and traditional sparse array approaches have performance that would prevent them from succeeding at such detailed neuroimaging studies. In contrast, new high-density DOT techniques extend the capabilities of optical methods to meet these challenges.

Chapter 4

Retinotopic Mapping of the Visual Cortex

4.1 Introduction

Functional near infrared spectroscopy (fNIRS) and diffuse optical tomography (DOT) have shown promise as tools for neuroimaging in populations ill-suited to functional magnetic resonance imaging (fMRI) and positron emission tomography (PET) due to a combination of the techniques' portability and comprehensive measurement of hemodynamics. While the potential impact is great, in order to become a widespread neuroscience tool, non-invasive optical imaging techniques need to be developed with the capability to map brain function with reasonably high resolution, repeatability, and sensitivity. Neuroimaging systems are expected to be able to not only identify cortical areas, but also discriminate features and borders within them. These challenges are not unique to emerging optical techniques, but were also faced by both PET and fMRI in their early development. fMRI and PET established their worth as brain mapping tools through their ability to map the highly organized structure of the visual cortex. In this chapter, I demonstrate that high-density DOT is able to meet this same neuroimaging benchmark through mapping the visual field using traveling waves of neuronal activation and phase-encoded mapping procedures [White and Culver, 2010a].

Invasive studies of animals have shown that the visual cortex is composed of many distinct processing areas, each with its own map of the visual field (or subset thereof) [Essen et al., 1992]. These maps are retinotopic, meaning that adjacent areas in the visual field map to adjacent areas of the cortex. So, an easily controlled stimulus can be used to selectively activate these different cortical locations. Thus, the visual cortex provides an ideal test system for judging the reliability and resolution of new neuroimaging systems. Retinotopic mapping was used for the validation of both PET [Fox et al., 1987] and fMRI [Engel et al., 1994, 1997, DeYoe et al., 1994]. The ability to conduct retinotopic mapping has further enabled neuroscience studies of processing in the visual cortex [Tootell et al., 1997, Tootell and Hadjikhani, 2001]. In addition, the visual cortex continues to be used as a standard system by which to judge further improvements in image quality and algorithms, such as constructing a common atlas space for adults and children [Kang et al., 2003].

Visual responses have been studied with NIRS [Colier et al., 2001], however, the spatial resolution of the sparse systems previously used has been too low to distinguish the retinotopic organization within the visual cortex. Thus, such studies have been limited to differentiating the right and left hemispheres. However, even without access to high spatial resolution, the visual cortex has still served as a model system for advancing temporal NIRS methods, including event-related algorithms [Schroeter et al., 2004, Plichta et al., 2006], multimodal imaging with fMRI [Toronov et al., 2007], extending optical methods to bedside neonatal measurements [Karen et al., 2008, Taga et al., 2003], and developing methods to simultaneously analyze multiple hemodynamic contrasts [Wylie et al., 2009].

Having developed a high-density diffuse optical tomography (HD- DOT) system as an advance on previous fNIRS technology, we have previously been able to discriminate two activations within the same visual quadrant using block-design paradigms [Zeff et al., 2007]. I now address the task of mapping the visual field with higher spatial resolution to show that HD-DOT is able to reproduce classic neuroscience results. Rather than activating individual cortical regions in a block paradigm, I use stimuli that move periodically in the visual field, creating a traveling wave of activation in the visual cortex [Engel et al., 1994, DeYoe et al., 1994]. Decoding the resulting periodic activations with Fourier analysis allows the construction of full retinotopic maps that relate each area of the visual field to locations in the cortex [Sereno et al., 1995, DeYoe et al., 1996, Tootell et al., 1998]. Through these experiments, we are able to evaluate the ability of HD-DOT to contiguously map the entire visual field. Additionally, we can test our ability to construct high signal-to-noise maps in individual subjects, which is a crucial step for clinical neuroimaging.

Continuing the analysis of Chapter 3, I also analyzed the same phase-encoded data with sparse arrays. First, as the triangular sparse array (Fig. 3.1b) is a subset of the high-density array (Fig. 3.1c), I re-imaged the data to see if the sparse array could reproduce the mapping found with DOT. Second, I wanted to be sure that errors in *in vivo* imaging were not due to subject motion or instrument noise. Thus, I simulated retinotopic mapping targets, much as point targets were simulated in Chapter 3. Thus, I can evaluate with confidence the ability of sparse NIRS and DOT to perform complicated neuro-mapping tasks. These results are intended to demonstrate increases in the fidelity of HD-DOT mapping, allowing the field to move forward more confidently into novel and clinical experiments.

4.2 Methods

4.2.1 Stimulus Paradigm

The study was approved by the Human Research Protection Office of the Washington University School of Medicine and informed consent was obtained from all participants prior to scanning. Fourteen healthy adult subjects (11 female, 3 male, age range 21–27) were recruited with no known neurological or psychiatric abnormalities. Subjects 1 to 5 were scanned three times each; the rest were scanned once. Thus, a total of 24 data sets were analyzed in the experiment. Subjects were seated in an adjustable chair in a sound-isolated room facing a 19 inch LCD screen at a viewing distance of 90 cm. The imaging pad was placed over the occipital cortex, and the optode tips were combed through the subject's hair. Hook-and-look strapping around the forehead held the array in place. The distance over the top of the head from the nasion to the top row of optodes was measured so as to establish repeatable cap placement.

All stimuli were phase-encoded, black-and-white reversing logarithmic checkerboards (10 Hz contrast reversal) on a 50% gray background [Engel et al., 1994, DeYoe et al., 1994]. Polar angle within the visual field was mapped using counter-clockwise and clockwise rotating wedges: minimum radius 1°, maximum radius 8°, width 60°, and a rotation speed of 10°/s for a cycle of 36 s. This rotation frequency allows for each stimulated brain region to return to baseline before subsequent activations [Warnking et al., 2002]. In fMRI retinotopic experiments, it is common to use two simultaneous rotating wedges. However, resolving the resulting ambiguity involves *a priori* knowledge of anatomy, allowing activations to be ascribed solely to the contralateral hemisphere [Warnking et al., 2002]. In this study, we preferred not to use *a priori* knowledge of the functional architecture and instead decided to use a stimulus with a single rotating wedge to eliminate ambiguity. Eccentricity within the visual field was mapped with expanding and contracting rings: minimum radius 1°, maximum radius 8°, width 1.4° (3 checkerboard squares), and 18 positions with 2 s per position for a total cycle of 36 s. Subjects were instructed to fixate on a central crosshair for all experiments, and the four stimuli were presented in a pseudorandom order. All stimuli started with 5 s of a 50% gray screen, continued with ten cycles of the phase-encoded stimulus, and concluded with 15 s of a 50% gray screen.

4.2.2 Phase-Encoded Processing

The phase-encoded stimuli create a traveling wave of neuronal activity along the cortical surface as the stimuli move through the visual field. Relative to the stimulus onset, each cortical position will be periodically activated with a different delay. Since we know the position of the stimulus on the screen at each time, we can match each pixel's measured delay to the area of the visual field to which it corresponds [Sereno et al., 1995]. In order to perform this analysis, the series of activations due to each stimulus was down-sampled to 1 Hz (36 time points per stimulus cycle). Since the data has already been low-pass filtered to 0.5 Hz, this step does not remove any information, but allows the convenience of having one activation frame per stimulus location. Recall that due to the earlier log-ratio step, each cortical location's time trace had been shifted (mean subtracted) so that the mean of each contrast was zero over the entire scan period. Every pixel's timecourse was Fourier transformed and the phase at the stimulation frequency (0.0278 Hz = 1/36 s) found. This phase then corresponds to the delay between stimulus onset and the pixel's activation.

However, we additionally need to correct for the finite neurovascular response time. Assuming that this lag time remains fixed at each cortical position, we can correct for this delay using counter-propagating stimuli [Sereno et al., 1995]. Our convention is to define zero phase as the center of the visual field for the ring stimuli and as the lower vertical meridian for the wedge stimuli. The positive phase direction is defined as outwards for the ring stimuli and counter-clockwise for the wedge stimuli. The visual field is thus defined with a right-handed coordinate system (r, θ)[a]. To find the corrected phase, we first inverted the phase found for clockwise and inwards stimuli by adding π and correcting for phase-wrapping. These phases, for each pixel, were then averaged with the phases from the counter-clockwise and outwards stimuli, respectively, to generate a corrected phase.

Using this phase analysis, we find the average phase lag is approximately 1 radian. Given that an entire stimulus cycle is 36 s, this corresponds to a neurovascular lag of 5.7 s. This is longer than one might expect, however, it is a measure of the delay between of the time that the stimulus is centered over a cortical location until peak response rather than a measure of stimulus onset to response onset, which is how neurovascular lag is normally reported. While the phase images have this lag automatically removed by the above phase averaging, activations from a single stimulus still retain the lag. Thus, when presenting data from a single stimulus trial, we assume a 6 s lag.

After combining data from the two stimulus propagation directions, the wedge phase maps represented how every angle of the visual field is mapped to the cortex, and, similarly, the ring phase maps showed retinotopic eccentricity mapping [Sereno et al., 1994]. Both before and after averaging, the phase maps were smoothed using a 3 pixel by 3 pixel moving box average.

---

[a] Note that while the end results are equivalent, this is the opposite visual angle phase definition from that used by [Sereno et al., 1994, 1995]

4.2.3 Co-registration

Since DOT does not have concurrent anatomical information, as is obtained with MRI, it can be difficult to compare results taken over multiple imaging sessions. There are slight differences in where one subject places the pad day-to-day ($\approx$ 2 mm) and slightly larger differences in where the pad fits best on different subjects ($\approx$ 6 mm). While we measured the external position of the imaging pad relative to external anatomic landmarks, allowing us to be sure we were always imaging the visual cortex, the precision of this measurement was too low to serve as the sole co-registration method. We desired a method to locate the visual cortex that was relatively independent of the variables to be analyzed. Since the visual stimulus excites low-order visual cortex areas the most strongly, the magnitude of the Fourier component at the stimulation frequency measured at each cortical position creates an image that highlights the right and left visual cortices. All points with a magnitude greater than the half-maximum were considered to be in either the right or left visual cortex (based on their position relative to the midline). The centroid of each region was then determined, and the midpoint between the two centroids was considered to be the center of the visual cortex. When combining or comparing data from multiple sessions and subjects, each imaging session was translated so that this center point was at the center of the image. It is important to note that co-registration was not used when analyzing data from a single imaging session. In all cases, we intend to judge the quality of the data based on its internal pattern and not on its location relative to unknown external landmarks.

4.2.4 Comparison with Sparse fNIRS Arrays

In order to show that the ability to map retinotopy was due to the performance of high-density DOT arrays, I imaged some of the data acquired during this study with the triangular sparse fNIRS array (Fig. 3.1b). Since this triangular array is a subset of the high-density array, this merely involves cropping the set of measurements to the sparse subset. Since the square array (Fig. 3.1a) is not a subset of the high-density array, this data could not be directly compared to retinotopic maps taken with such an array. For this analysis, the field-of-view was restricted to the region of high sensitivity and low image artifacts (as in Section 3.2.1).

4.2.5 Simulated Cortical Activations

As a bridge between the earlier analysis of point-spread functions (Chapter 3) and the *in vivo* results in this chapter, I also performed *in silico* simulations of the type of brain activations I acquired in my retinotopic mapping study. With this technique, we can see if any *in vivo* artifacts found in the high-density or sparse arrays are as expected from the system's simulated performance or whether such artifacts should be ascribed to measurement noise. Thus, we can be more confident that the benefit we see with HD-DOT are valid.

I created a sequence of target activations $\mathbf{x}_{sim}(t)$, where each frame has a target similar to the activations seen in the *in vivo* data. The visual angle mapping sequence consists of target activations 10 mm in radius traveling in an ellipse (20 mm and 15 mm major and minor axes) with a center slightly off center from the center of the field-of-view (from here on referred to as the elliptical target). The eccentricity mapping sequence consists of two rectangular targets (30 mm width, 14 mm height) moving upward in the field-of-view (to be referred to as the bar target). Reconstructed responses $\mathbf{x}_{recon}(t)$ were then constructed as earlier (Equations 3.1 and 3.2). Phase-encoded mapping of these periodic responses was performed as in Section 4.2.2.

4.3 Results

4.3.1 HD-DOT Images from Phase-Encoded Stimuli

Our three-dimensional image reconstruction yields a 1 Hz series of images of cortical activations. In order to examine the contrast-to-noise of the responses to the visual stimuli, I block-averaged the data across the multiple cycles of the periodic stimuli, which resulted in a 36 frame movie (1 frame/second) for each stimulus. Four frames from a movie of the response to the counter-clockwise rotating wedge stimulus in one subject (subject 1, session 1) show that we can locate responses in all four visual quadrants (Fig. 4.1). As expected from prior retinotopic studies, activations appear in the opposite cortical hemisphere from the area of the visual field where the stimulus was located (Video 4.1). Since every pixel has been independently mean subtracted over the entire study, any pixel with activation necessarily has a time period where its value is negative. Thus, the regions with negative ΔHbO_2 opposite the activation should not be confused with a true neuronal deactivation.

Similarly, four frames from a movie of the response to the expanding ring stimulus (subject 4, session 1) show that we can locate responses to multiple visual field eccentricities (Fig. 4.2 and Video 4.2). Since this stimulus appears in both the right and left visual hemifields, we see activations corresponding to the left and right visual hemispheres. As the stimulus moves outward in the visual field, both activations move upward in our field-of-view.

These studies were repeated in these subjects over three sessions. In all three

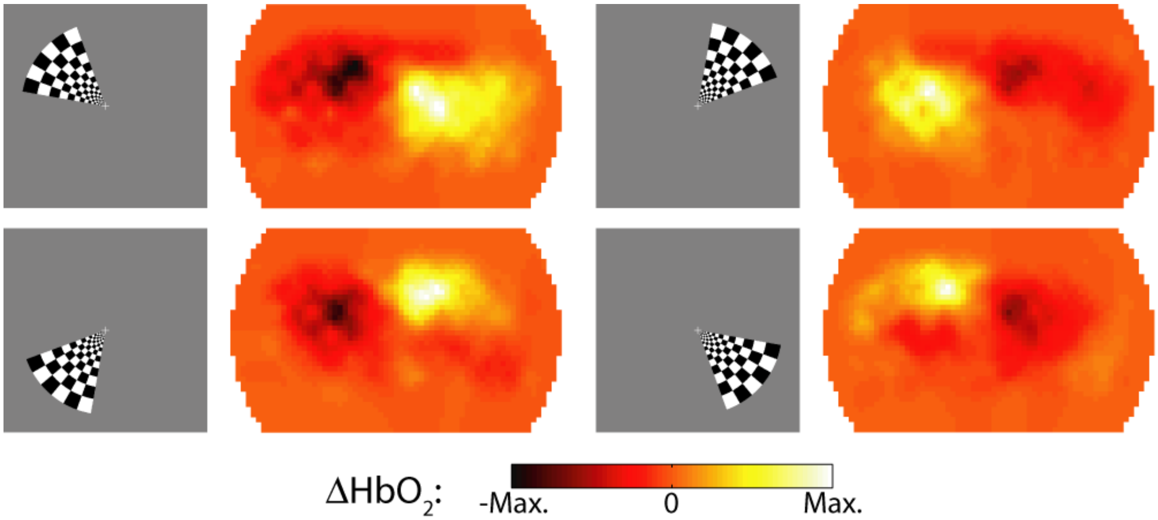

Figure 4.1: Examples of activations due to a counter-clockwise rotating wedge stimulus (subject 1, session 1). In order to match the stimuli and responses for this figure, I have used our measured 6 s lag between stimulation and maximal response. Note that the hemodynamic response is always maximal in the opposite visual quadrant from the stimulus.

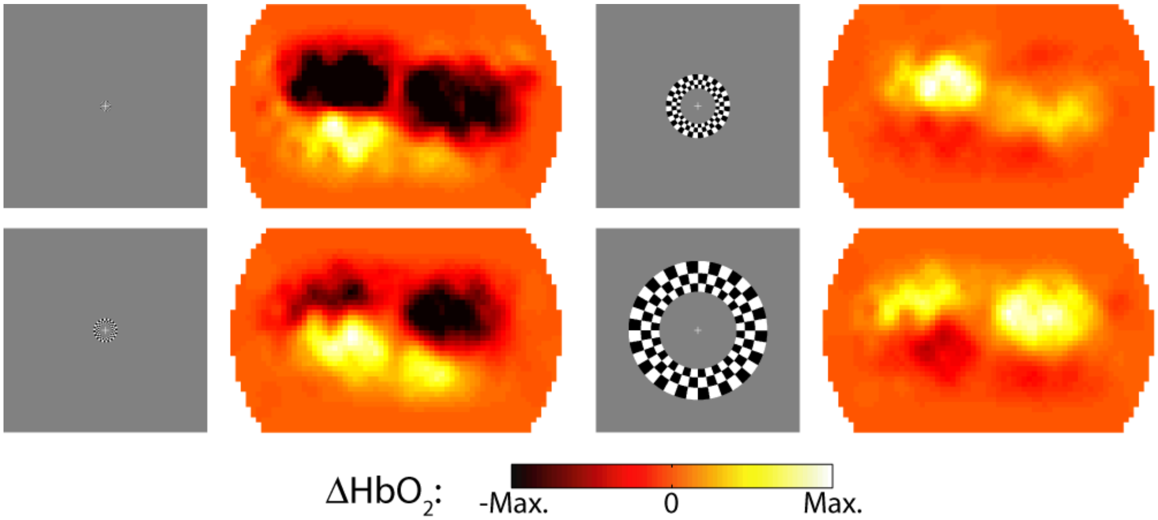

Figure 4.2: Examples of activations due to an expanding ring stimulus (subject 4, session 1). In order to match the stimulus and response for this figure, we have used our measured 6 s lag between stimulation and maximal response. Note that the maximal hemodynamic response is bilateral and moves upward as the stimulus moves outward.

sessions, the activations appear in the same relative locations. This repeatability is demonstrated in Fig. 4.3, where a contour has been drawn at half-maximum for each of the stimulus frames chosen above in Figures 4.1 and 4.2. While the eccentricity data is slightly noisier than the visual angle data, the activations in both studies on subsequent days appear in the same area of the cortex.

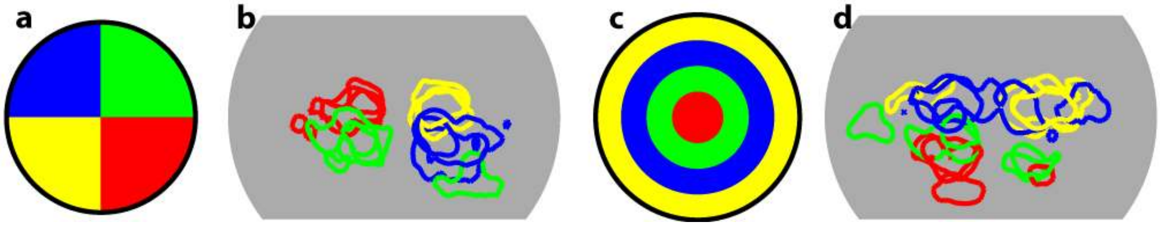

Figure 4.3: Repeatability of retinotopic activations. (a) Legend showing the color-coding of different visual quadrants, each corresponding to one of the stimuli chosen from the full movie (Fig. 4.1). (b) An overlay of contours drawn at half-maximum contrast for each of four stimuli (roughly corresponding to the visual quadrants in (a)) in subject 1 over three separate imaging sessions. Note the repeatability of the localization of the measurements. (In one session the upper right visual field caused a second activation in the ipsilateral cortex, which may be due to worse signal-to-noise on that day.) (c) Legend showing the color-coding of different visual eccentricities, each corresponding to one of the stimuli chosen from the full movie (Fig. 4.2). (d) An overlay of contours drawn at half-maximum contrast for each of four stimuli (roughly corresponding to the eccentricities in (c)) in subject 4 over three separate imaging sessions. Note the repeatability of the localization of the measurements.

High contrast-to-noise data demonstrating the ability to discriminate multiple angles and eccentricities within the visual field was obtained from all 14 subjects analyzed. The robustness of the data is shown for selected data sets in Fig. 4.4 for the wedge stimulus. The upper visual cortex (denoted with red and yellow) has the highest signal-to-noise in all subjects (both activations are placed in the correct hemisphere in all 14 subjects). The lower visual cortex (denoted with green and blue) is noisier (the lower left visual cortex is localized in 4 subjects, and the lower right visual cortex in 12 subjects). Similarly, Fig. 4.5 demonstrates the ability to robustly see multiple eccentricities within subjects with the ring stimulus. The central visual field (coded red and green) is seen in all 14 subjects, while the periphery (coded blue and yellow) is noisier and sometimes does not appear (the blue is localized in 13 subjects, yellow in 12). In addition, the system's sensitivity to the two hemispheres is not always equal. The average over all 24 sessions clearly shows clean discrimination of visual angles (Fig. 4.4f) and eccentricities (Fig. 4.5f), with all four selected frames having high signal-to-noise localized activations.

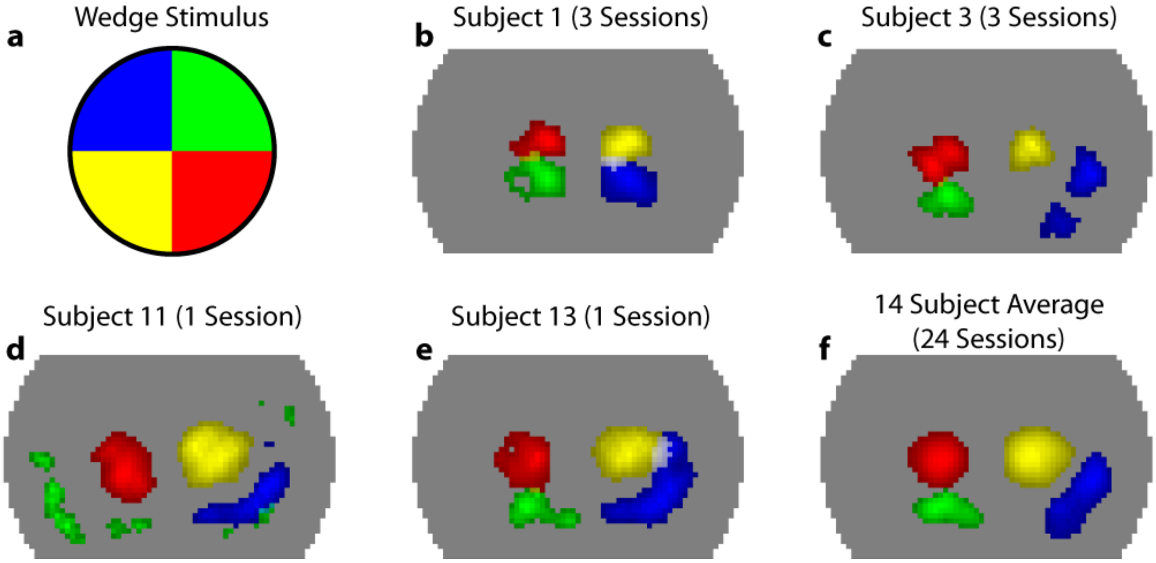

Figure 4.4: Examples of activations due to a counter-clockwise rotating wedge stimulus in multiple subjects. (a) Legend showing the color-coding of different visual quadrants roughly corresponding to the four frames chosen from the full movie in Fig. 4.1. (b) Overlay of four activations (with a threshold at the half-maximum contrast of each frame) from subject 1 (all sessions averaged). Note the ability to clearly discriminate multiple visual angles within a single hemisphere. (c-e) Similar overlay images showing four visual quadrants in additional subjects. (f) Four visual quadrants shown in the average of all 24 sessions from 14 subjects.

These inter-subject differences might be the result of differences in cortical folding. In some subjects, we obtained anatomic MRI scans from a separate study. These images were segmented in Caret, and the area beneath the optode array labeled to a

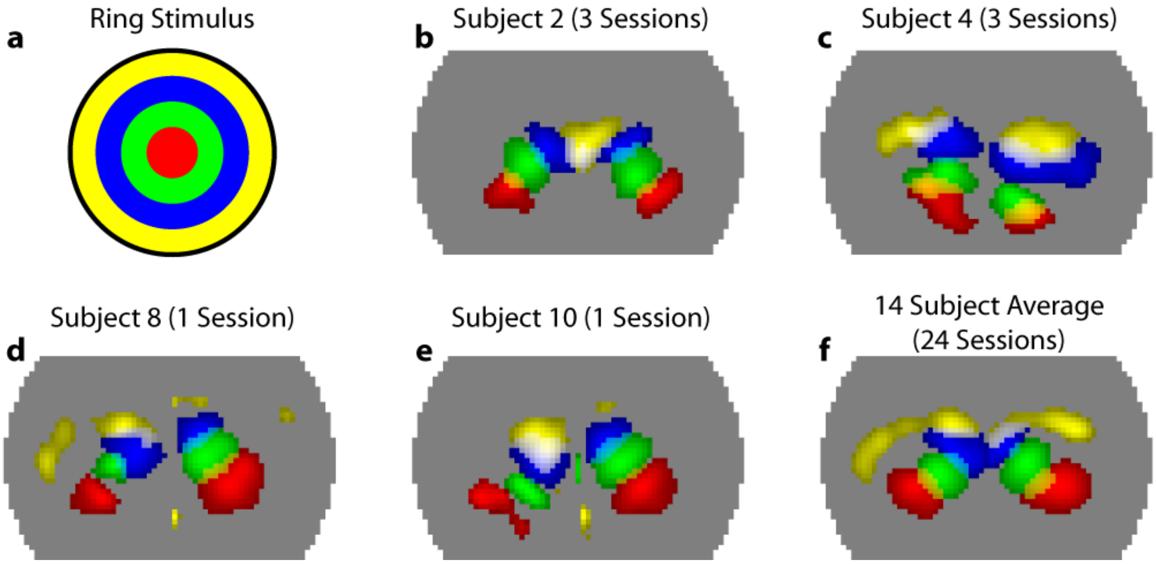

Figure 4.5: Examples of activations due to an expanding ring stimulus in multiple subjects. (a) Legend showing the color-coding of different visual eccentricities roughly corresponding to the four frames chosen from the full movie in Fig. 4.2. (b) Overlay of four activations (with a threshold at half-maximum contrast; due to uneven sensitivity to the two hemispheres, the right and left halves of the pad have different thresholds) from subject 2 (all sessions averaged). Note the ability to clearly discriminate multiple eccentricities within a single hemisphere. (c-e) Similar overlay images showing four eccentricities in additional subjects. Occasionally, the peripheral visual field (yellow) is seen only with low signal-to-noise. (f) Four visual eccentricities shown in the average of all 24 sessions from 14 subjects.

depth of 2 mm (our approximate sensitivity depth into the brain). In some subjects we were able to see DOT sensitivity above and below the calcarine sulcus (which divides the representations of the upper and lower visual fields) (Fig. 4.6a). In other subjects, the calcarine sulcus terminated inferiorly, such that the lower visual cortex (with the upper visual field representation) was presumably hidden from view behind the cerebellum (Fig. 4.6b). These anatomical variations seem to explain differences in the ability to perform functional localization (Fig. 4.6c,d). Similar results are seen between the two hemispheres. In subject 3, the calcarine sulcus terminated superiorly in the left hemisphere, but inferiorly in the right hemisphere (Fig. 4.7a,b). In this subject, we can only see lower visual cortex (upper visual field) activations in the left hemisphere (Fig. 4.7c).

4.3.2 Retinotopic Mapping Using Phase Data

If we first examine a pixel chosen from one of the regions that responds strongly to the rotating wedge visual stimulus, we see that over the course of the entire stimulus presentation (10 cycles, subject 1, session 1) there is a strong hemodynamic response each time the stimulus passes (Fig. 4.8a), although, since each contrast is mean-subtracted, the traces don't return to a "baseline" in between stimulations. Note that the data has high signal-to-noise, which is reflected in this trace's (ΔHbO_2) Fourier transform (Fig. 4.8b). Almost all of the power is concentrated in the stimulus frequency with little background noise. We then examine this Fourier transform at the rotation frequency (0.0278 Hz = 1/36 s). An image of the height of this peak indicates the areas that respond strongly to the stimulus, highlighting the two hemispheres of the visual cortex (Fig. 4.8c). The phase of this Fourier component relates each pixel to a visual angle within the visual field (Fig. 4.8d,e); in this image, we have used

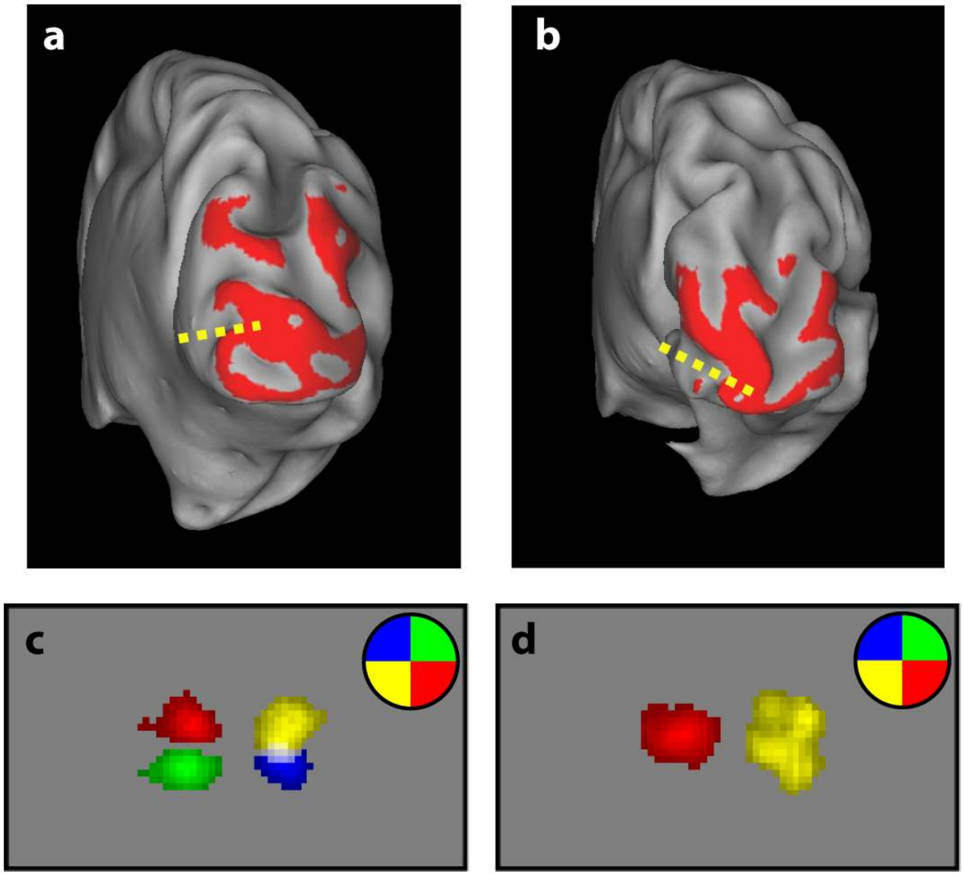

Figure 4.6: Anatomical differences explain inter-subject differences in DOT maps. (a-b) Inflated posterior views of the cortical surface of the right hemisphere in two subjects. The expected optode sensitivity is shaded in red. The calcarine sulcus is noted in by the dashed yellow line. In subject 1 (a), we expect sensitivity both above and below the sulcus. In subject 2 (b), almost all the sensitivity is above the sulcus. (c-d) Overlay of activations seen in these subjects. In subject 1 (c), we see all four quadrants (inset shows the quadrant definitions in the visual field), which as expected given sensitivity both above and below the calcarine sulcus. In subject 2 (d),we only see the lower visual field with high signal-to-noise (upper visual cortex, again with an inset legend). This results confirms our hypothesis as we didn't much sensitivity below the calcarine sulcus.

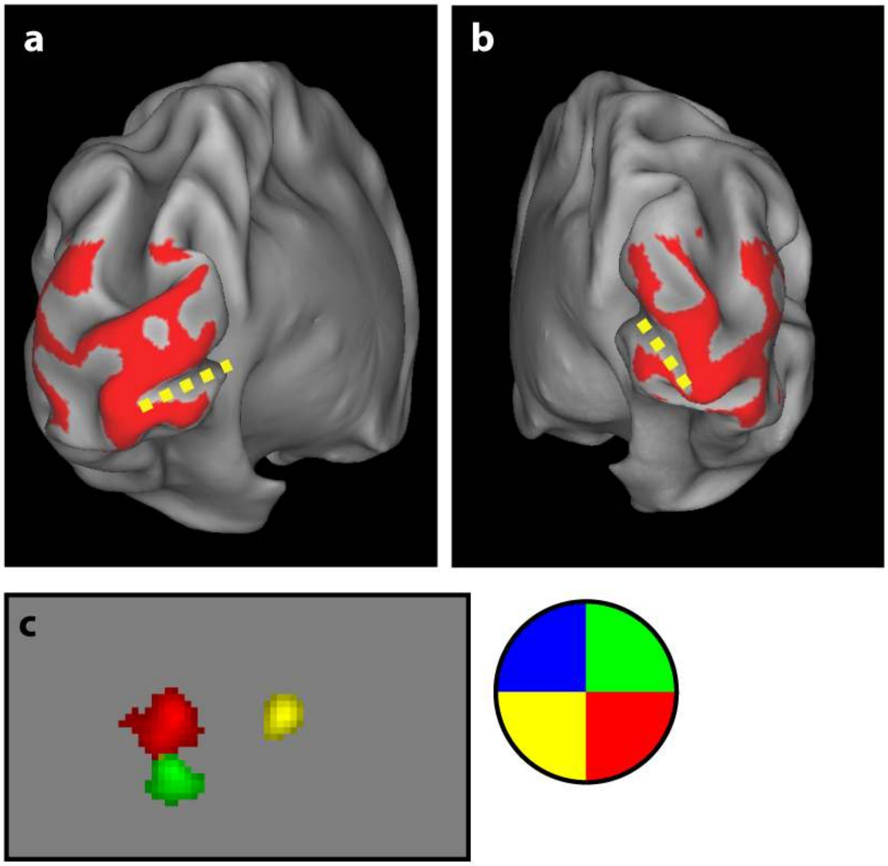

Figure 4.7: Anatomical differences explain inter-hemispheric differences in DOT maps. (a-b) Inflated posterior views of the cortical surface of the left (a) and right (b) hemispheres in subjects 3. The expected optode sensitivity is shaded in red. The calcarine sulcus is noted by the dashed yellow line. In the left hemisphere, we expect sensitivity both above and below the sulcus. In the right, almost all the sensitivity is above the sulcus. (c) Overlay of activations seen with high signal to noise in this subject (inset shows the quadrant definitions in the visual field). We see both the upper and lower visual cortex in the left hemisphere, but only the upper visual cortex in the right, as hypothesized from the anatomy of the calcarine sulci.

phases from the clockwise and counter-clockwise stimuli to remove the delay between the neuronal and vascular responses. In the middle of the field-of-view, we can see a clear "pinwheel" pattern that corresponds to a 180° rotation of the visual field.

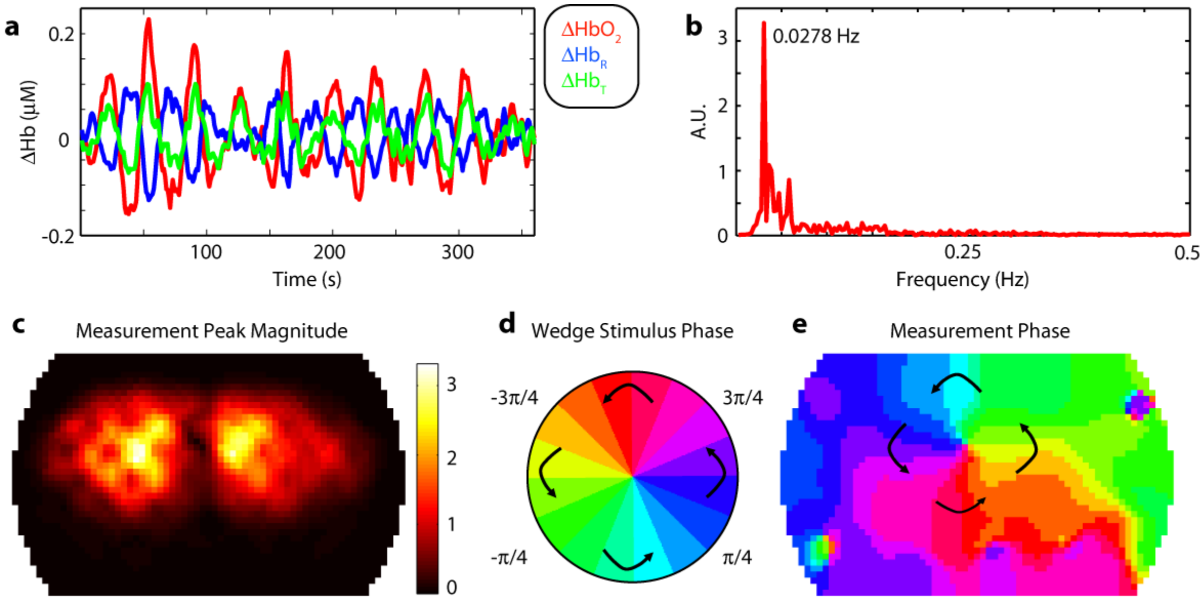

Figure 4.8: Fourier processing of phase-encoded data. (a) Time traces in all three contrasts (ΔHbO_2, ΔHbR, and ΔHbT) from a single pixel (subject 1, session 1). Note the high signal-to-noise as we see ten activations due to the ten cycles of the stimulus. As each contrast trace has individually been mean subtracted, the returns to baseline between the cycles appear as "deactivations". (b) Magnitude of the Fourier transform of the ΔHbO_2 signal in (a). Note the strong peak at the rotation frequency, with little background noise in the signal. (c) An image of the magnitude of the peak in the Fourier transform across the field-of-view of the pad. Bright areas correspond to pixels that respond most strongly to the stimulus. Two visual hemispheres are clearly visible. (d) A legend defining phases of visual angle within the visual field. (e) The phase of the Fourier transform of each pixel in the field-of-view. This phase corresponds to the delay between the start of the stimulus cycle and the activation of that region in the cortex and thus relates each location in the visual field to its cortical projections.

Examining the phase data from multiple subjects shows, as expected from the earlier quadrant data, a similar pattern in all subjects (Figs. 4.9 and 4.10, here we are focused on a 6 cm by 4 cm subset of the imaging domain centered over the visual cortex). The lower visual field (phases color-coded light green through dark blue) is seen robustly in all subjects. However, the upper visual field (phases color-coded violet through yellow) is seen only in five subjects and is usually smaller in extent than the lower visual field representation. In eccentricity, we see the expanding rings as a stack of phases vertically and bilaterally in the two hemispheres. The most central areas of the visual field (lowest eccentricity, color-coded blue through red) are the most robustly visible (seen in all subjects). In twelve subjects, we are also able to see representations of the peripheral visual field (color-coded orange through green). The phase images shown were all constructed using oxyhemoglobin as a contrast, but maps constructed using deoxyhemoglobin and total hemoglobin are qualitatively similar (Fig. 4.11).

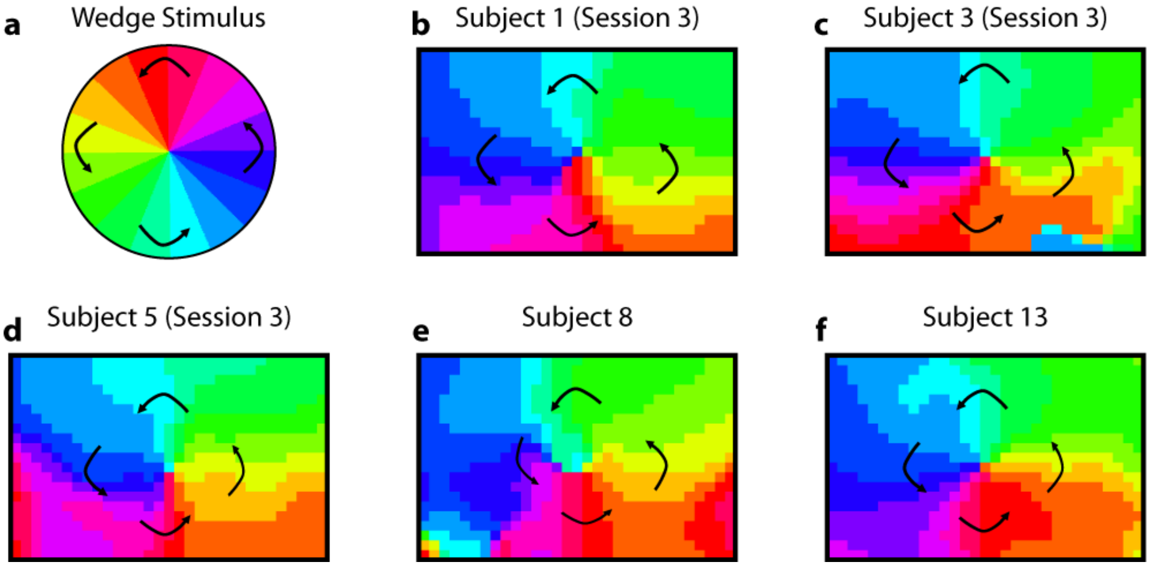

Figure 4.9: Retinotopic maps from phase-encoded wedge stimuli in multiple subjects. (a) A legend defining phases of visual angle within the visual field. (b-f) Retinotopic maps of the organization of visual angle within the center of the visual cortex of five subjects. Note that in all subjects we see the same "pinwheel" pattern as in (a) and Fig. 4.1. Arrows are shown for orientation.

We also performed Fourier phase analysis using the co-registered, averaged data

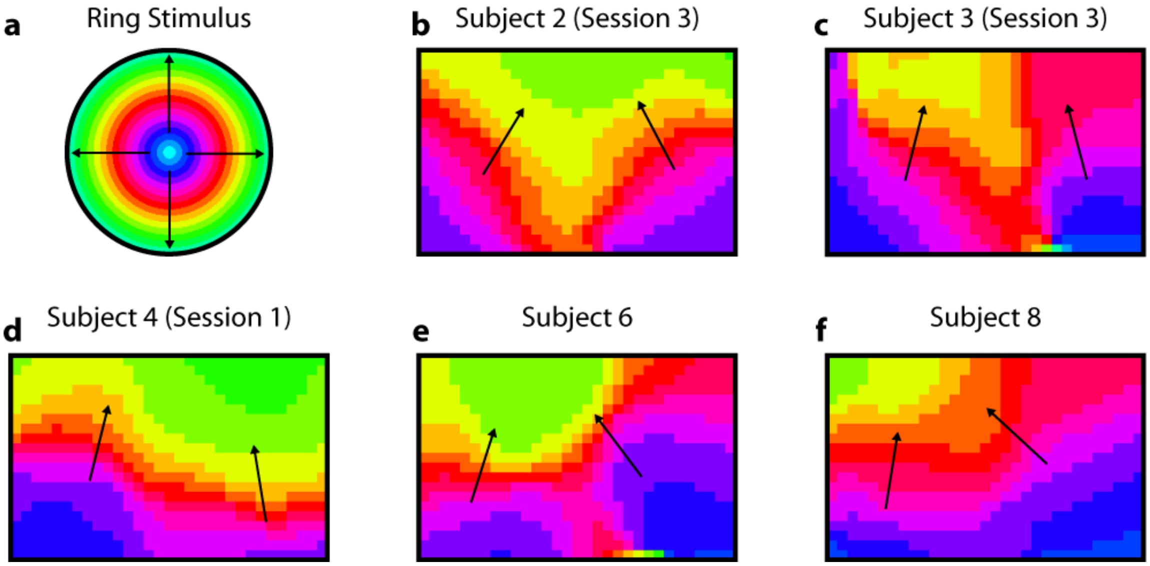

Figure 4.10: Retinotopic maps from phase-encoded ring stimuli in multiple subjects. (a) A legend defining phases of eccentricity within the visual field. (b-f) Retinotopic maps of the organization of eccentricity within the center of the visual cortex of five subjects. Note that in all subjects we see the same stacked pattern as expected from the individual frame activation data (Fig. 4.2). Arrows are shown for orientation.

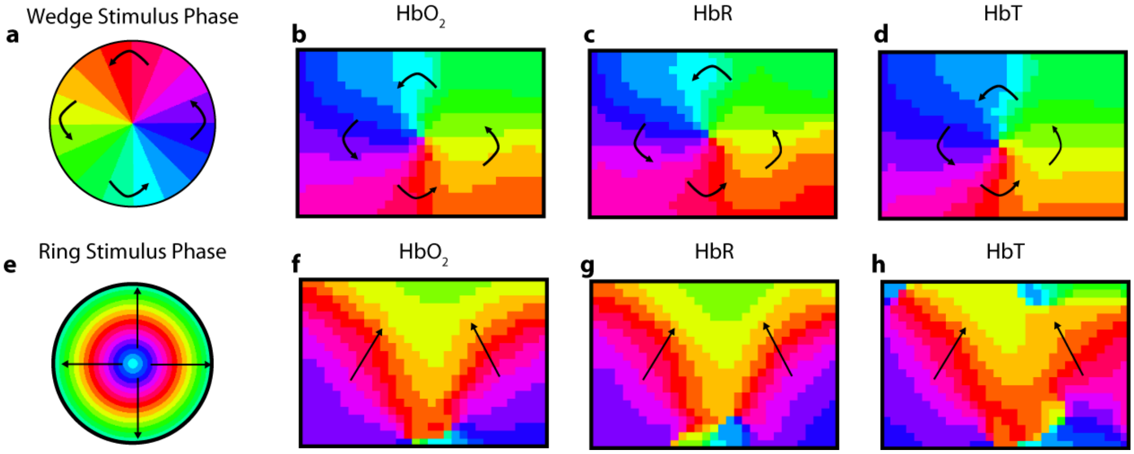

Figure 4.11: Retinotopic maps from phase-encoded stimuli using multiple hemodynamic contrasts. (a) A legend defining phases of visual angle within the visual field. (b-d) Retinotopic maps of the organization of visual angle within the center of the visual cortex in subject 1 (session 1) using all three hemodynamic contrasts. Note that in all contrasts we see the same "pinwheel" pattern as in (a) and Fig. 4.9. (e) A legend defining phases of eccentricity within the visual field. (f-h) Retinotopic maps of the organization of eccentricity within the center of the visual cortex in subject 2 (session 3) using all three hemodynamic contrasts. Note that in all contrasts we see the same stacked pattern as expected from Fig. 4.10. Arrows are shown for orientation.

from all 24 scanning sessions. The phase from the wedge stimulus shows the "pinwheel" pattern around the center of the visual field (Fig. 4.12a,b). As with the individual subjects' data, the lower visual field (upper visual cortex) is more strongly represented in our field-of-view (in the figure, we see large areas with green through blue phases). The upper visual cortex (lower visual field, phases violet through yellow) is smaller, but can still be clearly seen. The phase from the ring stimulus shows the "stacked activations" pattern seen in the individual subjects' data (Fig. 4.12d,e). While the ability to see the peripheral visual field varied between subjects, here the periphery (phases colored orange through green) is clearly visible.

The gradient of the phase images (steepest ascent in phase) shows the representation of the visual field unit vector within the visual cortex. The gradient of the wedge stimulus shows the angular unit vector, and the gradient of the ring stimulus shows the radial unit vector. The angular unit vector shows the direction of the cortical activation traveling wave associated with the counter-clockwise wedge stimulus, while that for the radial unit vector shows the direction of travel of the expanding ring activation. When we take the gradient of the group-average wedge stimulus phase map, we see that the unit vectors show a vortex around the center of the visual field (Fig. 4.12c). The gradient of the group-average ring activation phase map shows the upwards direction of movement (Fig. 4.12f). In both of the gradient images, the lengths of the vectors at each position have been normalized so that they contain information about the direction of the gradient but not its slope. These vector plots can also reveal areas of curl and divergence in the peripheral field-of-view that may be less apparent in the images of phase.

The visual cortex is divided into multiple processing areas, each with it's own retinotopic map of the visual field. As these maps are contiguous in spatial representations at their boundaries, the coordinate system reverses across the borders.

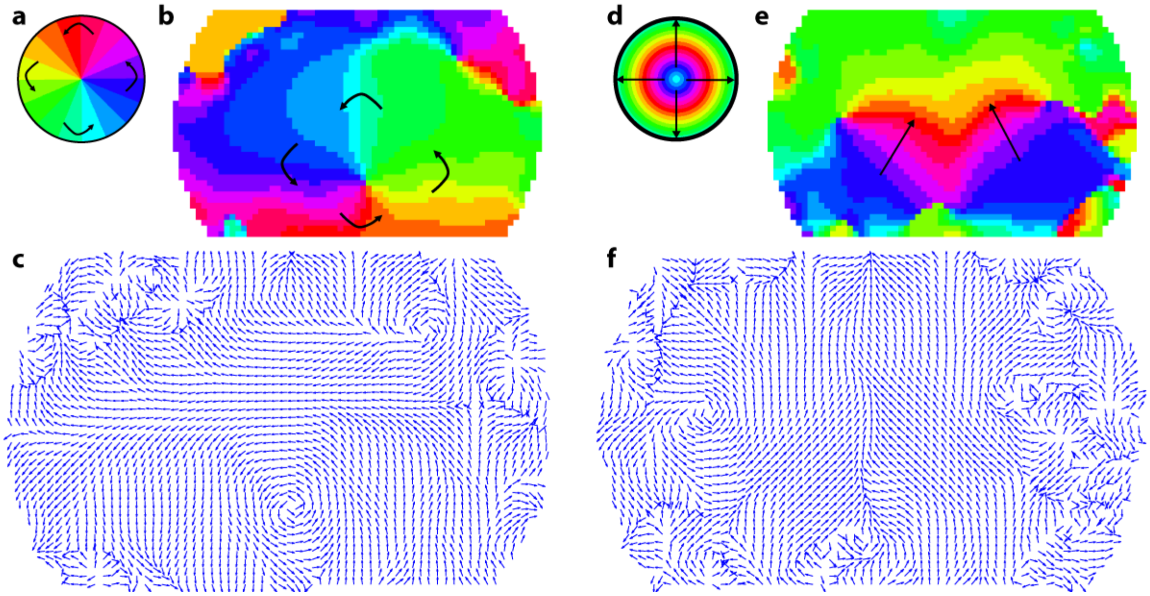

Figure 4.12: Retinotopic maps from phase-encoded stimuli in the subject-averaged data. (a) A legend defining phases of visual angle within the visual field. (b) A retinotopic map of the organization of visual angle within the center of the visual cortex. Note the same "pinwheel" pattern as in (a) and Fig. 4.9 in the center of the field-of-view. (c) The gradient of the phase map in (b). Each arrow's length is normalized to one and the direction shows the direction of steepest ascent (after compensating for phase-wrapping). The arrows thus show the direction of motion of the traveling wave of activity due to the counter-clockwise wedge stimulus on the visual cortex. Note the large area of rotation. There is additional structure visible in the periphery of the field-of-view. (d) A legend defining phases of eccentricity within the visual field. (e) A retinotopic map of the organization of eccentricity within the center of the visual cortex. Note the same stacked pattern as expected from Figs. 4.2 and 4.10. (f) The gradient of the phase map in (e). Each arrow's length is normalized to one and the direction shows the direction of steepest ascent (after compensating for phase-wrapping). The arrows thus show the direction of motion of the traveling wave of activity due to the expanding ring stimulus on the visual cortex. Note the large area of bilateral upward gradients.

For example, while V1 maps the visual field in a mirror-image (left-handed) fashion, the map in V2 is non-mirror-image (right-handed). The gradient maps of phase (Fig. 4.12c,f) are the unit vectors of the coordinate system. Thus, analyzing their relation at each voxel gives us a measure of the handedness of the map (Fig. 4.13). We can parcellate our DOT images into mirror- and non-mirror-image sections, putatively reflecting borders between different processing regions.

4.3.3 Comparison with Sparse fNIRS

To continue the comparison of sparse and high-density imaging arrays (from Chapter 3) using *in vivo* data, I analyzed the above data using the full high-density system as well as a subset that forms the triangular sparse array [White and Culver, 2010b]. While the triangular sparse array can somewhat place the wedge activations in the correct quadrant, the activations are extended and have strange shapes, often with components in the wrong quadrants (Fig. 4.147c,d and Video 4.3). Similarly, this array often mislocalizes the ring responses or fails to reconstruct entire hemispheres of activity (Fig. 4.15c,d and Video 4.4). The high-density array accurately places both activation series throughout the field of view with tighter localization (Figs. 4.14e,f and 4.15e,f).

I then performed retinotopic mapping using Fourier analysis. The triangular sparse array is unable to correctly map the organization of the visual cortex with either stimulus. With the wedge stimulus, while the triangular sparse array appeared to do an adequate job reconstructing individual stimulus frames, this in fact masked an inability to create a proper phase pattern for either stimulus type. With the wedge stimulus (Fig. 4.14h), there are three main errors: (1) what should be vertical gradients in phase are instead reported as horizontal gradients in the upper field-of-view;

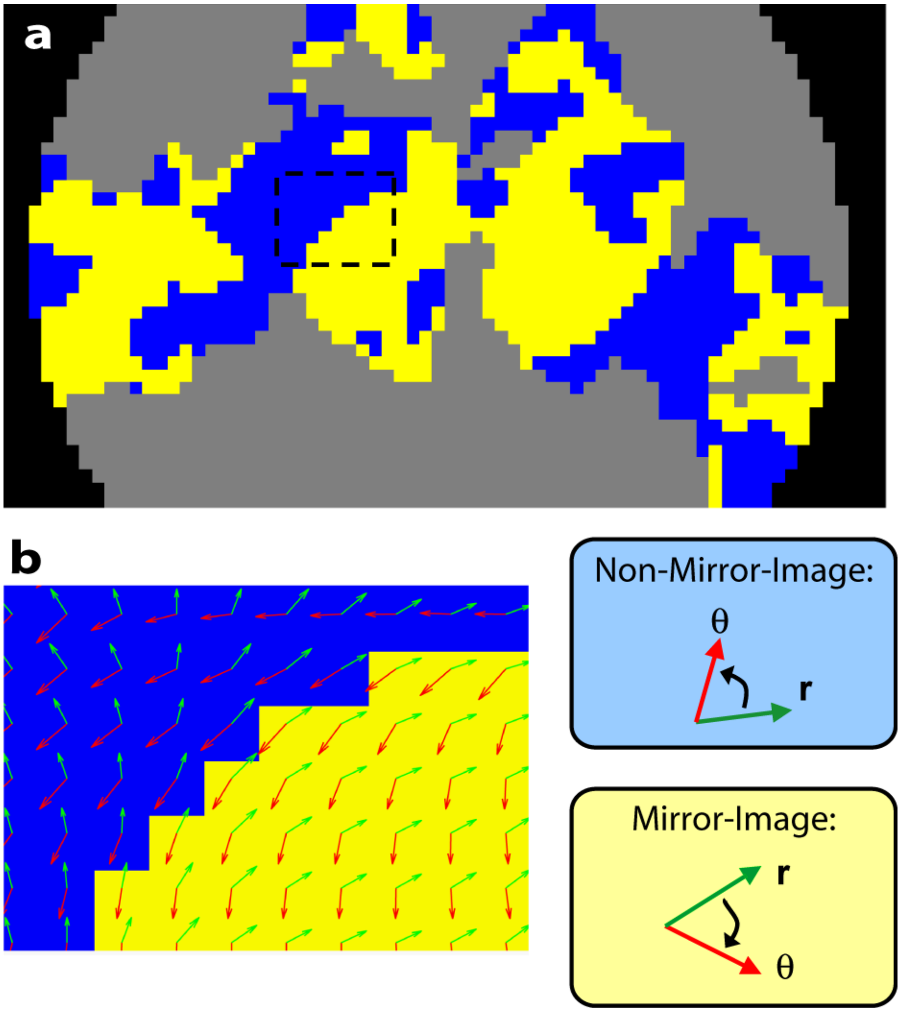

Figure 4.13: Finding cortical borders in the visual cortex with DOT. (a) The visual cortex in subject 1 (session 1, ΔHbT) divided into mirror- and non-mirror-image sections based on the relationship between the radial unit vector (gradient of phase in eccentricity) and the angular unit vector (gradient in phase of visual angle). Areas colored gray had phases too noisy to perform the analysis; areas in black are external to the brain. Note the bilateral striped pattern of mirror- and non-mirror-image regions are we move peripherally in the visual cortex. (b) A close-up of the dashed box in (a) showing the unit vectors overlaid on the handedness labeling. Note how the relationship between the two vectors changes from approximately 90° in one direction to approximately 90° in the other as we cross the boundary.

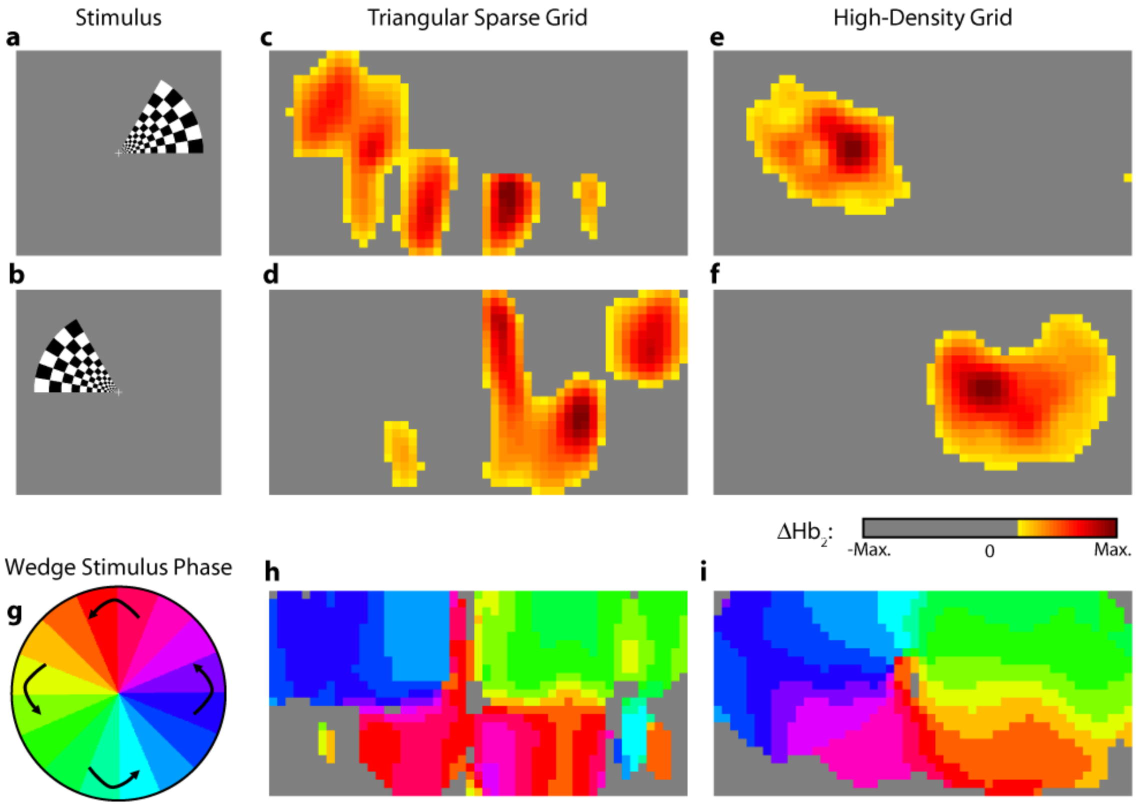

Figure 4.14: Comparison of sparse fNIRS and high-density DOT through retinotopic mapping of the wedge stimuli (subject 1, session 1). (a-b) Two equally spaced frames from the stimulus. (c-d) Activations from these stimuli reconstructed with the triangular sparse array. Note the poor localization and strange activation shapes. (e-f) Reconstructions using the high-density array. Activations are correctly placed with reasonable sizes. (g) Legend defining the phase of the target phase-encoded stimulus. (h) The phase of each pixels activation at the rotation frequency using the triangular sparse array. Note the inability to reconstruct a pinwheel of phase. (i) Phase mapping with the high-density array, which correctly locates all phases.

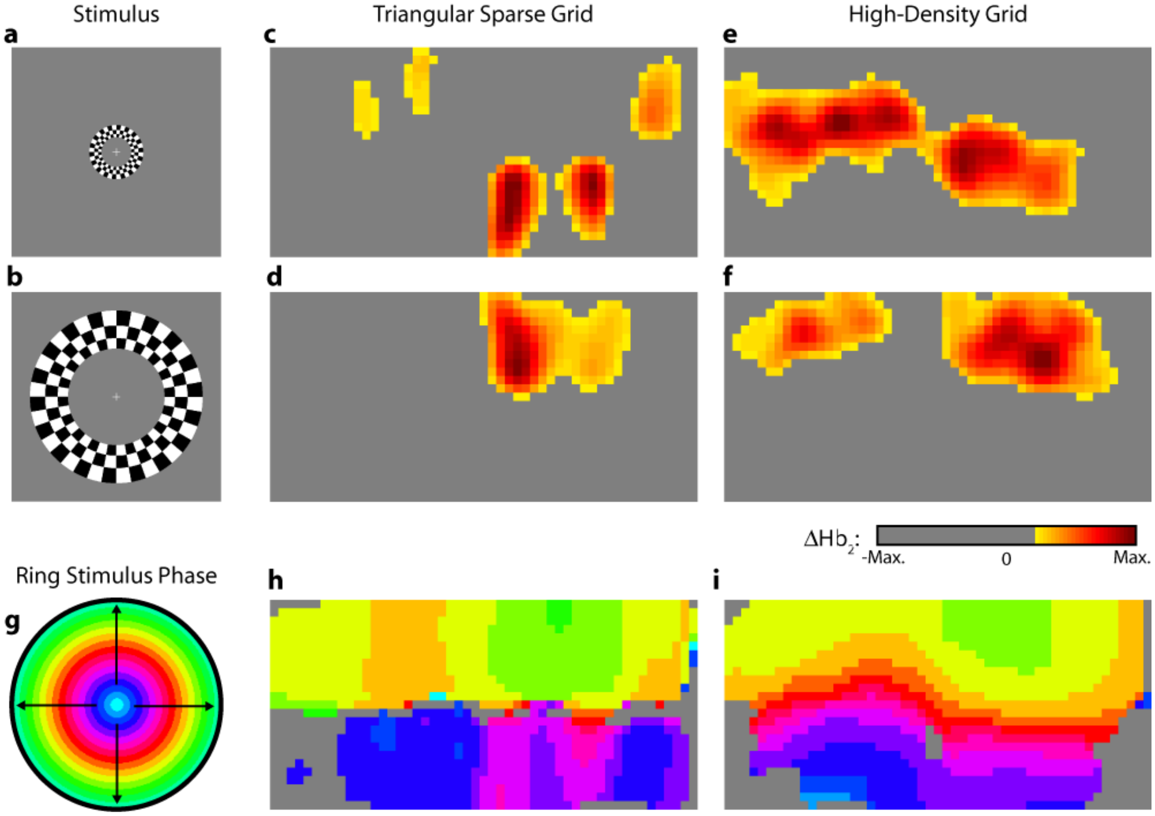

Figure 4.15: Comparison of sparse fNIRS and high-density DOT through retinotopic mapping of the ring stimuli (subject 4, session 1). (a-b) Two equally spaced frames from the stimulus. (c-d) Activations from these stimuli reconstructed with the triangular sparse array. Note the poor localization, especially when the activation passes beneath the source line, and the inability to always locate activations in both hemispheres. (e-f) Reconstructions using the high-density array. Activations are correctly placed with reasonable sizes. (g) Legend defining the phase of the target phase-encoded stimulus. (h) The phase of each pixel's activation at the rotation frequency using the triangular sparse array. Note the ability to distinguish only two regions, and the conversion of vertical gradients into horizontal gradients. (i) Phase mapping with the high-density array, which correctly locates all phases.

(2) these gradients are reconstructed as bidirectional, resulting in local extrema of phase; and (3) in the lower field-of-view, the phase pattern has phases (e.g., magenta) reconstructed in the wrong quadrant. With the ring stimulus, the triangular sparse array is unable to reconstruct the expected phase pattern (Fig. 4.15h), again resulting in incorrect horizontal gradients and local extrema. Additionally, there is a discontinuity in phase between the lower and upper halves of the array. As expected, the high-density array is able to accurately replicate both expected phase patterns throughout the field-of-view (Figs. 4.14i and 4.15i).

4.3.4 Simulated Cortical Activations

In order to provide an intermediary evaluation between *in silico* point-spread functions (Chapter 3) and *in vivo* retinotopy experiments (Section 4.2.4), which necessarily excite extended areas of cortex, I performed simulations of activations designed to approximate neuronal activation patterns seen with the retinotopic mapping experiment. In the first experiment, the target was a 1 cm radius circle, which moved in an elliptical pattern through the field-of-view (Fig. 4.16a-c). In the second experiment, the target was a bilateral pair of rectangles moving vertically in the field-of-view (Fig.4.17a-c).

A reconstructed time series was generated for both series of targets and for each of the optode arrays. The square sparse grid results in linear reconstructions along the nearest source-detector measurement (Figs. 4.16d-f and 4.17d-f). The triangular sparse array localizes the activations well horizontally, but has only binary vertical discrimination–it can only tell whether the target is above or below the source line (Figs. 4.16h-j and 4.17h-j). The high-density grid performs well in localizing the targets throughout both series (Figs. 4.16k-m and 4.17k-m). Also see Videos 4.5 and

4.6.

By Fourier transforming each pixel's time traces and finding the phases at the rotation frequency, we can perform *in silico* phase-encoded retinotopic mapping. By convention, zero phase of the elliptical target is defined as its most vertical position (Fig. 4.16n) and for the bar target as the bottom of the field of view (Fig. 4.17n). Although the square sparse grid mislocalized many of the reconstructed targets, we see that it generates the correct pinwheel phase pattern for the elliptical target (Fig. 4.16o, although around the edges there are some abnormalities due to the uneven sampling sensitivity) and a distorted but recognizable general phase trend from bottom to top for the bar target (Fig. 4.17o). The triangular array has the same problems in simulation that were found *in vivo*, indicating that these problems were not solely due to noise during the scanning session. In both simulations (Figs. 4.16p and 4.17p), what should be vertical gradients are reconstructed as horizontal, local minima of phase are generated, phases appear in the wrong quadants, and there are missing phases when targets pass under the center source-line of the pad.

4.4 Discussion

4.4.1 Retinotopic Mapping

In this chapter, I performed a detailed spatial analysis of the visual cortex using our HD-DOT methods. Phase-encoded mapping of the visual cortex serves as an *in vivo* validation paradigm for many imaging questions. Here, our retinotopic mapping study highlights multiple advantages of the high-density diffuse optical tomography system. First, we are able to obtain high contrast-to-noise data from single subjects within a single session instead of having to rely on multi-subject averages. Thus,

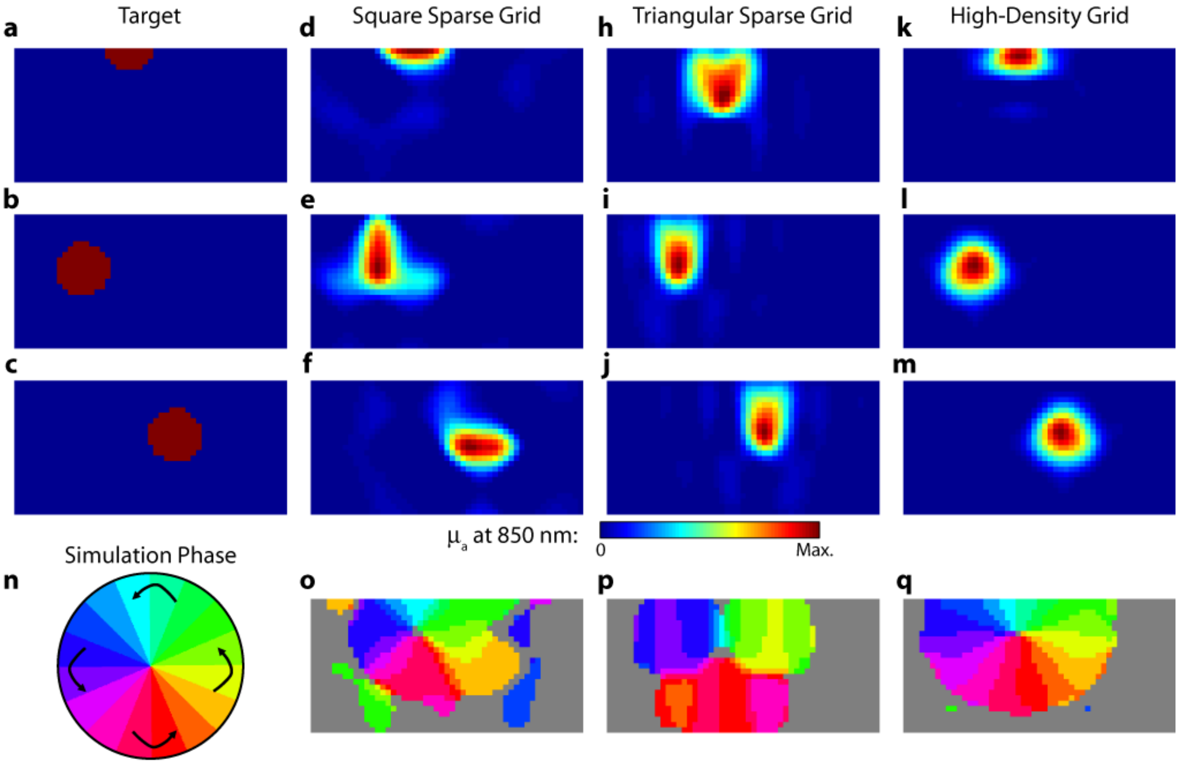

Figure 4.16: Simulations of activations similar to those from phase-encoded mapping of visual angle. The stimulus is of 1 cm radius and moves in an elliptical pattern, with the center of the ellipse displaced from the center of the field-of-view. There are a total of 36 activations in the entire rotation series. (a-c) Three equally spaced frames from sequence of targets. (d-f) These three activations are reconstructed with the square sparse array. The activations are displaced to the nearest measurement location. (h-j) Reconstructions using the triangular sparse array. The activations are located correctly horizontally, but displaced to the same vertical location. (k-m) Reconstructions using the high-density array. Activations are correctly placed with the correct size. (n) Legend defining the phase of the target phase-encoded stimulus. (o) The phase of each pixel's activation at the rotation frequency using the square sparse array. This measure gives the delay between the start of the stimulus and the maximum activation of each pixel. Areas with gray have low signal-to-noise and are discarded. The square sparse array is able to correctly reconstruct the pinwheel of phase from the original stimulus, with some lobes of abnormal phases near the edges and an asymmetric shape. (p) Phase-encoded mapping using the triangular sparse array. Vertical gradients have been incorrectly reconstructed as horizontal, and some phases have been placed in the incorrect quadrant. (q) Phase mapping with the high-density array, which correctly locates all phases in the pinwheel.

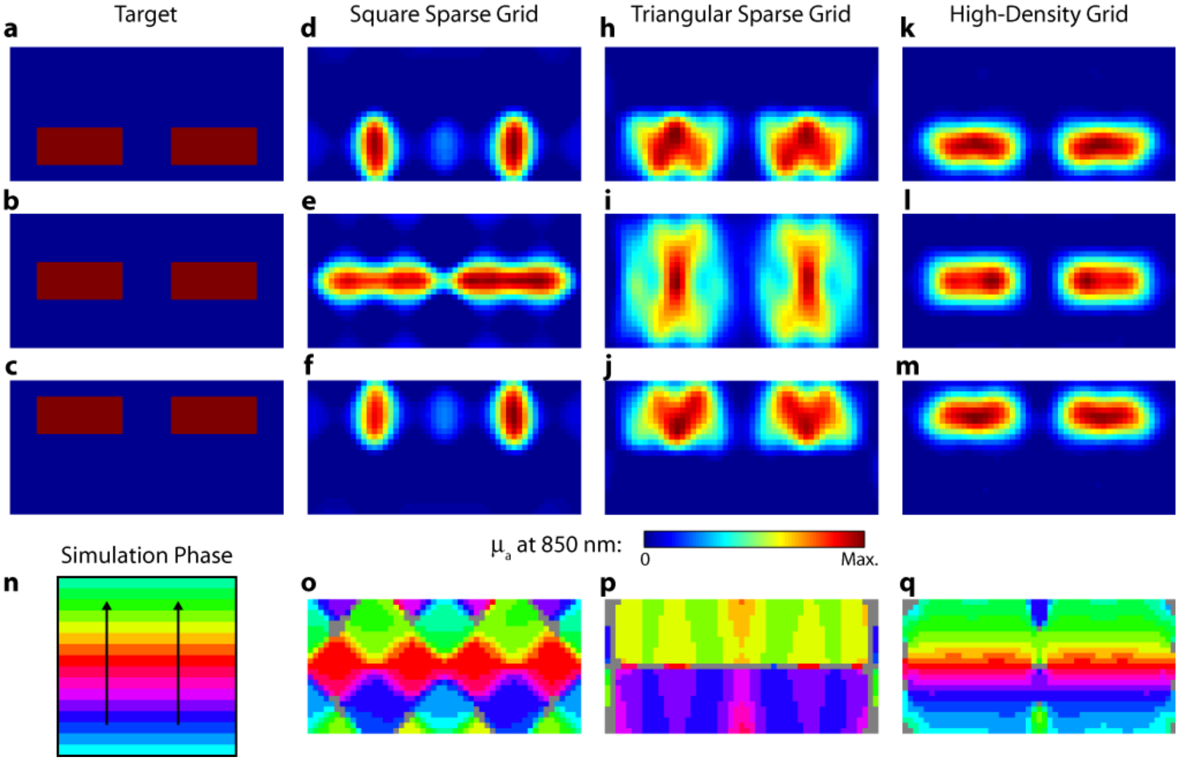

Figure 4.17: Simulations of activations similar to those from phase-encoded mapping of eccentricity. The stimulus is two 1.4 cm tall rectangles moving upward in the field of view. There are a total of 18 activations in the entire rotation series. (a-c) Three equally spaced frames from the sequence of targets. (d-f) These three activations are reconstructed with the square sparse array. The activations are displaced to the nearest measurement location, often resulting in squeezing in the horizontal direction. (h-j) Reconstructions using the triangular sparse array. Activations under the source planes are unconstrained vertically due to the pads symmetry. (k-m) Reconstructions using the high-density array. Activations are correctly placed with the correct size. (n) Legend defining the phase of the target phase-encoded stimulus. (o) The phase of each pixel's activation at the rotation frequency using the square sparse array. The square sparse array is able to find the general trend of increasing phase vertically, but with many artifacts in shape. (p) Phase-encoded mapping using the triangular sparse array. Due to the inability to vertically localize activations, the array can only define two general regions of phase, and it converts gradients that should be vertical to be horizontal. (q) Phase mapping with the high-density array, which correctly locates all phases in the target.

we can reliably detect inter-subject differences, which is necessary for moving to future clinical paradigms. Second, our high spatial resolution allowed us to visualize features within the visual cortex, such as the multiple visual angles and eccentricity representations within a single hemisphere, that have previously been unobtainable with fNIRS. Third, we have used these traveling cortical activations to create cortical maps of the retinotopic organization of the visual cortex.

Determining the organization of how each area the visual field activates the cortex is difficult with fixed-position stimuli due to the nature of the visual cortex's organization. First, individual visual stimulations take up a finite amount of the visual field and, thus, naturally excite a large area of the visual cortex. In addition, a single visual stimulus can excite multiple visual processing areas. Second, the detected size of the activation is further increased by the spatial extent of the neurovascular response. And third, the measurement is further blurred by convolution with the point-response function of the imaging technique. While these points can be addressed through the use of a large number of stimuli, such a procedure would be inefficient. Alternatively, the phase-encoded mapping procedure followed here (and reviewed in depth by Warnking et al. [2002]) easily resolves these issues. The Fourier analysis can reveal subtle differences in phase allowing the maps to be determined with greater detail than that available from the broad response to individual visual stimuli (compare the spatial extent of an activation in Fig. 4.1 to an individual phase in Fig. 4.9). Furthermore, the dynamics of the traveling wave can be used to distinguish different visual cortex regions, allowing more detailed studies of processing in the visual cortex [Wandell and Wade, 2003, Wandell et al., 2005].

4.4.2 High-Density DOT

The retinotopic mapping techniques demonstrated in this work are made possible by the image quality of high-density diffuse optical tomography systems. The majority of previous optical neuroimaging studies have been performed using solely time traces from source-detector measurements or images made with topographic back-projections (fNIRS or DOI). Because such systems require source-detector separations of around 3 cm in order to sample the cortex, their spatial resolution is thus restricted. In addition, as all measurements are a mixture of hemodynamics in the scalp, skull, and brain, data is often obscured by superficial and systemic hemodynamic artifacts.

The detailed mapping task of examining the organization of the visual cortex revealed subtle effects that limit wider utility of sparse systems. When examining individual point activations from individual stimuli, it might not appear that the worse resolution of the sparse systems is a problem. For example, in Fig. 4.16a-m, the sparse arrays seem to do an acceptable job at reconstructing the target activations. However, due to heterogeneous localization errors and resolution (Chapter 3, especially Fig. 3.4), they are unable to move beyond individual stimuli to assimilating that information to perform retinotopic mapping. The triangular sparse array is unable to properly decode phase in either simulation (Figs. 4.16p and 4.17p). While the square sparse array can do a reasonable job with the elliptical target (Fig. 4.16o), it suffers many artifacts when attempting to map the bar target (Fig. 4.17o). Only the high-density array can reconstruct both simulations properly (Figs. 4.16q and 4.17q). This *in silico* performance is duplicated *in vivo*, where a triangular sparse subset of the high-density array is unable to generate visual cortex maps of either visual angle or eccentricity that capture the correct global neural architecture (Figs. 4.14 and 4.15). These results show that HD-DOT is able to perform detailed studies of neural organization that are a step forward in the development of optical neuroimaging.

4.4.3 Variability and Cortical Folding

The ability to make high contrast-to-noise images within a subject that are repeatable gives us the confidence to ascribe inter-subject variations to true response differences rather than to system noise. Within this study, we have been able to detect such inter-subject differences. While all subjects had responses that followed the expected retinotopic organization, not every area of the visible field was seen in all subjects. This is most likely due to differences in cortical folding. These differences are not unexpected; similar variations have been found in both previous invasive, anatomic studies [Stensaas et al., 1974] as well as in fMRI retinotopic studies [DeYoe et al., 1996, Dougherty et al., 2003].

Due to DOT's low depth-of-penetration, the variations in the present experiment are more difficult to quantify. However, we can make some hypotheses about our observations. In some subjects, we fail to see the more peripheral areas of the visual field. Since the peripheral visual field in V1 is in the deepest (most anterior) area of the calcarine sulcus, we would expect this to be difficult to see with the current HD-DOT system. In those subjects in whom we do see more responses from stimulation in the peripheral visual field, we may be seeing representations in higher-order visual areas. The other area of the visual field that we sometimes fail to see is the upper visual field, which projects to the lower visual cortex. I hypothesize that, in these subjects, the calcarine sulcus terminates inferiorly on the occipital pole, causing the lower visual cortex to be located deeper and behind the cerebellum.

In future studies, better co-registration of DOT images with anatomic MRIs could be used to test these hypotheses. Photon propagation models could be generated using a more accurate tissue model. Localization of the pad would allow DOT image reconstructions to be inherently registered to the subject's anatomy, eliminating the need for *post hoc* co-registration. The position of activations relative to a segmented cortical surface would allow the calculated phases and gradients to be located on the known folded geometry. These advances would be aided by future improvements in dynamic range and signal-to-noise that allow increased depth sensitivity. For example, measurements up to 5th-nearest neighbor would enable detection of activations in sulcal depths that are missed by current techniques (Fig. 4.18) [Dehghani et al., 2009].

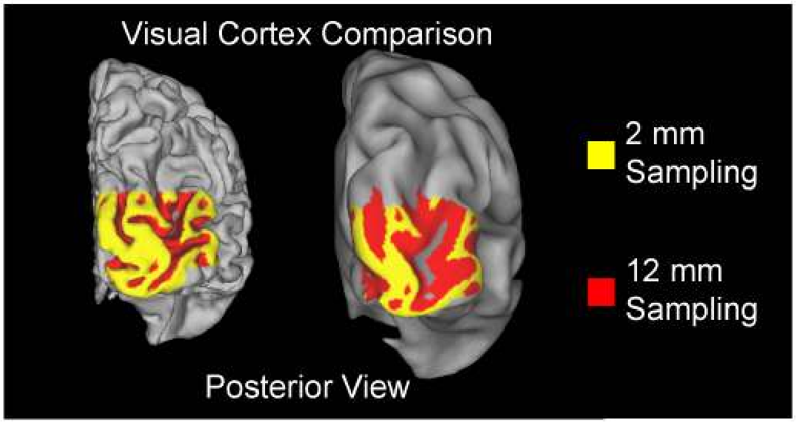

Figure 4.18: Increasing coverage of the visual cortex with more nearest neighbors. An anatomic MRI (subject 1, right hemisphere) was segmented using Caret and the cortex was colored based on it's depth. With the current system (using 1st- and 2nd-nearest neighbors, we expect to see approximately 2 mm into the cortex (yellow area), which enables to see only the tops of gyri. With a system with improved signal-to-noise and dynamic range (so as to be able to image with up to 5th-nearest neighbors), we expect depth-penetrations of 12 mm into the brain (red area), enabling almost all the sulcal depths along the convexity to be seen (the hemisphere is also shown slightly inflated for easier visualization of the sulci).

The phase and vector plots can also reveal additional structure in the peripheral field-of-view. These features can be used to find the boundaries between different cortical processing regions [Sereno et al., 1994, 1995]. This extension is important for taking the present HD-DOT results beyond a basic study of retinotopy towards studies of visual processing in populations not amenable to fMRI, such as development of the visual cortex in children and cortical plasticity after brain injury. However, this analysis requires interpolation that assumes the continuity of the retinotopic maps, including across cortical borders, while our current sampling is likely too superficial to separate gyral folds, at least in adults. This problem is especially acute in the subject-averaged results where data in the peripheral of the field-of-view might be from areas of the brain with more variable cortical folding, causing us to possibly average different cortical locations in each subject. With subject-specific anatomic modeling, the cortical folding could be made explicit, as it is with fMRI.

4.4.4 Conclusion

In this chapter, I have shown the use of optical imaging to perform full retinotopic mapping of the visual cortex non-invasively in adult humans. Previous optical studies focused on activating small patches of cortex and had the limitations of fNIRS systems, such as low spatial resolution, poor depth discrimination, and restricted field-of-view. The higher spatial resolution, brain specificity, and field-of-view of the high-density DOT system used herein enable us to map multiple visual angles and eccentricities within the same visual hemisphere. One of fMRI's original validations was its ability to reproduce retinotopic results that had been obtained through invasive animal experiments. This work establishes that high-density DOT is also able to meet this benchmark. In addition, I have shown that moving optical neuroimaging from single activation studies to cortical mapping is only possible with DOT techniques. Both simulations and *in vivo* data with sparse fNIRS arrays showed an inability to reconstruct the correct cortical organization. This is an example of how these phase-encoded paradigms and the maps they generate form a standardized model with which to judge new developments in optical algorithms and systems. With these advances in techniques and validation paradigms, the field of optical neuroimaging can move with more confidence into studies of higher-order brain function and of clinical utility.

Chapter 5

Functional Connectivity Mapping

5.1 Introduction

Optical neuroimaging has never lacked clinical potential, due to its ability to longitudinally and non-invasively monitor brain function. However, progress towards the bedside practice of methods to map brain function has been hindered by conceptual and technical limitations. One obstacle is that task-based neuroimaging, which is standard in cognitive neuroscience research, is generally ill-suited to clinical populations since they may be unable to perform any task. Recently in functional magnetic resonance imaging (fMRI), it was discovered that even during the absence of overt tasks, fluctuations in brain activity are correlated across functionally-related cortical regions [Biswal et al., 1995] (Fig. 5.1). Thus, the spatial and temporal evaluation of spontaneous neuronal activity has allowed mapping of these resting-state networks (RSNs) [Fox and Raichle, 2007]. Translating these advances to optical techniques would enable new clinical and developmental studies. Yet, mapping spontaneous activity with fNIRS measurements presents significant challenges due to the obscuring influences of superficial signals, systemic physiology, and auto-regulation. In this chapter, I develop DOT techniques that, combined with correlation analysis, allow us to isolate functional maps from resting-state measurements and demonstrate the feasibility of functional connectivity DOT (fcDOT) [White et al., 2009].

Low frequency fluctuations in cerebral hemodynamics have been detected by NIRS [Obrig et al., 2000, Elwell et al., 1999]. However, as the optical signal is a mixture of hemodynamics within the scalp, skull, and brain, it is particularly susceptible to artifacts from systemic changes. For example, global blood pressure fluctuations have been found to lead to misanalysis of functional responses in fNIRS studies [Jasdzewski et al., 2003, Boden et al., 2007]. In addition, the frequency components of systemic hemodynamics partially overlap those of RSNs. As with fcMRI, these systemic contributions must be removed to observe the underlying spatial maps of the brain networks. In part because fNIRS has traditionally had difficulty in separating different physiologic contributions, previous resting-state studies have focused on investigating the correlation between the measured signal and systemic physiological variables [Rowley et al., 2007, Reinhard et al., 2006, Katura et al., 2006, Franceschini et al., 2006]. While such experiments have yielded interesting results, including some within the clinical setting [Schroeter et al., 2005], they have not moved beyond temporal analysis to the study of spatial correlations and neural connectivity. As previously stated, fNIRS suffers from performance limitations. Low spatial resolution (≈ 3 cm) may average out any underlying spatial correlation structure. In addition, an fNIRS study to detect RSNs requires a field-of-view greater than typically available in order to cover both correlated and uncorrelated (e.g., control) brain regions.

While there are multiple challenges, both physiological and methodological, to the development of fcDOT systems, their successful creation would open up new approaches to the research of resting-state physiology. The discovery of functional connectivity (fcMRI) has led to its use as an important tool throughout neuroimaging

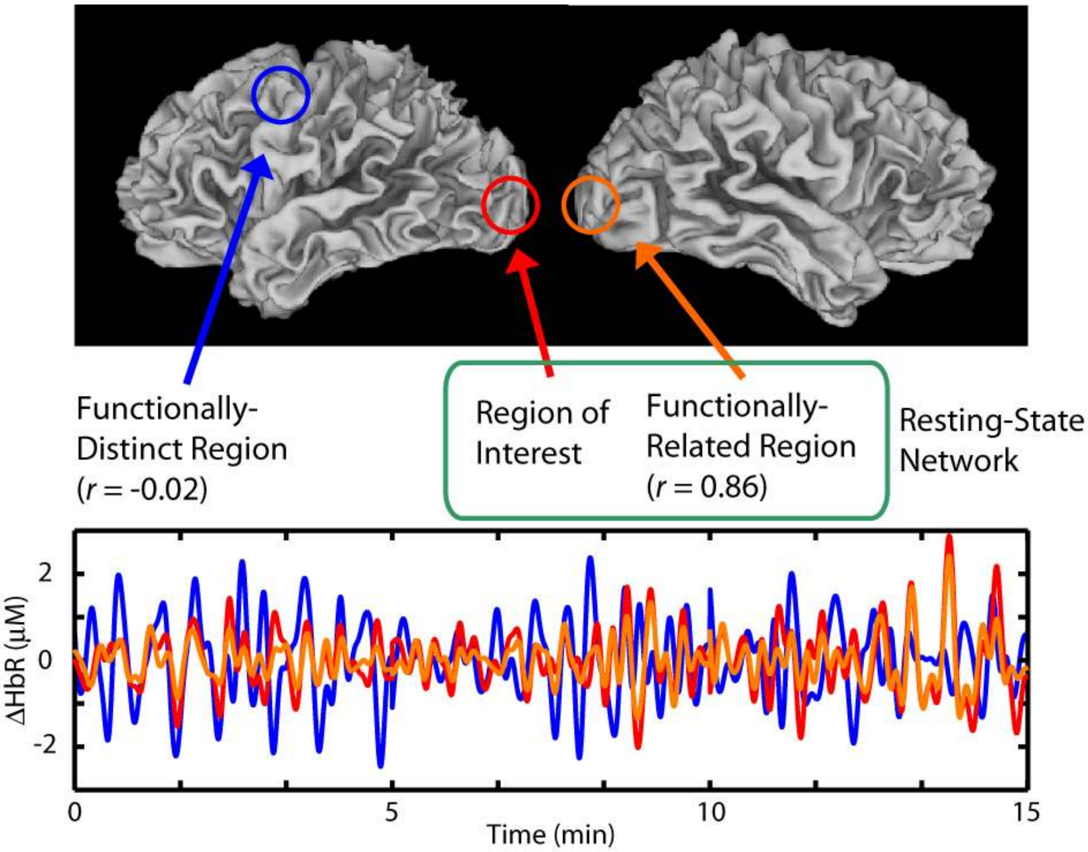

Figure 5.1: Correlated intrinsic brain hemodynamics in the resting-state measured with DOT (ΔHbR). First, we select a region of interest, here the left visual cortex (red time trace). Even in the absence of visual stimuli, the hemodynamics in the right visual cortex are highly correlated (orange time trace, $r = 0.86$) with those in the left. However, the hemodynamics in functionally-distinct regions (such as the left motor cortex) are uncorrelated (blue time trace). We group all the areas that are correlated into a "resting-state network". (Although the eye easily picks out patterns where the motor and visual cortices are correlated, note that uncorrelated ($r = 0$) is not the same things as anti-correlated ($r = -1$). In order for the correlation coefficient to be zero overall, there will necessarily be periods where the two traces are correlated as well as times when they are anti-correlated.)

research [Fox and Raichle, 2007], including insights into childhood brain development [Fair et al., 2007, 2008, Fransson et al., 2007]. Recent fcMRI studies have found RSNs that are altered in patients with depression [Greicius et al., 2007], Alzheimer's disease [Greicius et al., 2004], and Tourette syndrome [Church et al., 2009]. However, important brain-injured populations, such as intensive care patients, cannot be easily transported to fixed scanner environments. The portability and wearability of fcDOT systems could allow significant applications in populations that are not amenable to traditional functional neuroimaging, such as hospitalized patients and young children.

To address our goal of fcDOT mapping, I extended our field-of-view to provide unique simultaneous 3D imaging of distributed cortical regions covering both the visual and motor cortices with high resolution. These spatial techniques are complemented by our linear regression methods (Eq. 2.48) that remove global superficial signals and correlation analyses to map spontaneous brain activity patterns. We judge the success of fcDOT by our ability to obtain spatial correlations maps based on local physiology that match the fcMRI literature and our own subject-matched fcMRI experiments. Functional connectivity was first demonstrated by BOLD-fMRI detecting low-frequency variations in the motor cortex during the resting state [Biswal et al., 1995]. fcMRI's original validation was that the resulting spatial correlations corresponded with the brain's functional architecture as mapped by task-induced responses. Previous fcMRI studies have also demonstrated that the motor and visual cortices constitute largely independent functional networks, each exhibiting high levels of inter-hemispheric correlation [De Luca et al., 2006, Damoiseaux et al., 2006]. We, thus, expect resting-state analysis of seed regions found from a sensory task-response study to reveal that sensory network, while the other sensory network will provide a control that should be uncorrelated. These studies aim to establish the utility of DOT for functional connectivity analysis.

5.2 Methods

5.2.1 Protocol and fcDOT Analysis

Healthy adult subjects were recruited (4 female and 1 male, ages $24-27$). Informed consent was obtained prior to both DOT and MRI scanning. The protocol was approved by the Human Research Protection Office of the Washington University School of Medicine. Stimulus studies were performed to locate the motor and visual cortices. The visual cortex was stimulated using pseudorandom blocks of right and left lower visual quadrant reversing checkerboard grids (10 Hz reversal on 50% gray background, 10 s on and 20 s off). The sensorimotor cortex was stimulated with pseudorandom blocks of right and left finger tapping (self-paced at about 3 Hz, 10 s on and 20 s off). For resting-state analysis, a 50% gray screen with a crosshair was viewed (in 5 min blocks for 10 or 15 min total). The stimulus and resting-state trials were presented in a pseudorandom order for each session.

Subjects were seated in an adjustable chair facing a 19 inch LCD screen at 70 cm viewing difference. DOT imaging arrays were placed over the visual (24 sources, 28 detectors, Fig. 5.2a) and sensorimotor (24 sources, 18 detectors, Fig. 5.2b) cortices and held in place with hook-and-loop strapping. The position of the pads relative to the nasion and inion was measured to establish repeatable positioning. When performing superficial signal regression, a separate regressor was created from each pad's own 1^{st}-nearest neighbors (in case scalp/skull hemodynamic artifacts differed between the two locations). All images shown are projections of cortical shells (Visual: posterior coronal view, Motor: superior horizontal view, Fig. 5.2c,d).

Functional response images were obtained by block-averaging each subject's trials and temporally averaging (5 s) around the peak hemodynamic response. For each of the four regions of interest (left/right visual and left/right motor cortices) and for

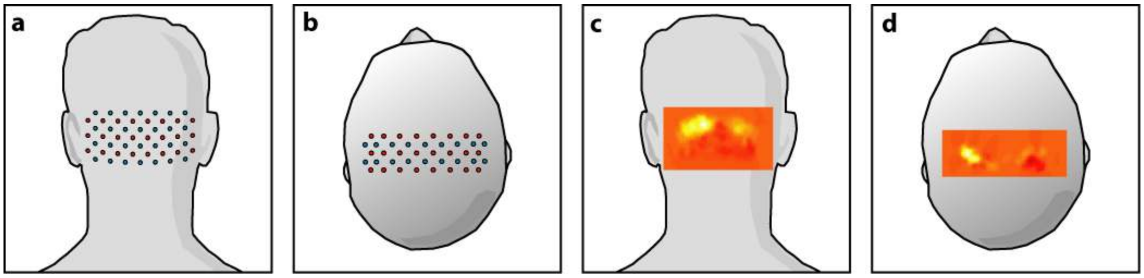

Figure 5.2: DOT imaging system for functional connectivity. (a) Schematic of the visual cortex imaging pad (24 sources, red, and 28 detectors, blue). (b) Schematic of the motor cortex imaging pad (24 sources, red, and 18 detectors, blue). (c) A left visual cortex response (ΔHbO_2), posterior coronal projection of a cortical shell. (d) A motor cortex response (ΔHbO_2), superior axial projection of a cortical shell.

each subject, a 1 cm^3 volume was chosen as a seed region for correlation analysis. Resting-state images were low-pass filtered (0.08 Hz). The resting-state time traces from within each seed volume were averaged to create a seed signal, and correlation coefficients were calculated between the seed signal and every other voxel in the field-of-view of both imaging pads (see Section 5.2.3).

5.2.2 fMRI Acquisition and Analysis

For comparison, we scanned one subject with fcMRI. fMRI data were acquired on a Siemens 3 T MAGNETOM Trio scanner. The session included two structural scans: a T1-weighted MP-RAGE sequence (TE = 3.08 ms, TR(partition) = 1000 ms, flip angle=8°, 176 slices with 1 × 1 × 1 mm voxels) and a T2-weighted turbo spin-echo image (TE = 84 ms, TR = 6.8 s, 32 slices with 1 × 1 × 4 mm voxels). Resting-state fMRI was performed using a BOLD-sensitive asymmetric spin-echo echo-planar sequence (TE= 27 ms, flip angle=90°, in-plane resolution 4 × 4 mm). Whole-brain EPI volumes of 40 contiguous, 4 mm-thick axial slices are obtained every 2.5 s. For each resting-state acquisition run, the subject viewed a small crosshair on the screen while 128 consecutive frames were acquired (320 s). Four resting-state runs were acquired ($\approx$ 20 min total).

Preprocessing removed motion and systematic intensity differences. Images were registered to an atlas, resampled to 3 mm cubic voxels, and spatially smoothed. Each voxel's time course was temporally band-pass filtered ($0.009 - 0.08$ Hz) and linear regression removed sources of spurious correlations: signals from head motion, the whole-brain average, the ventricles, and white matter. Seed regions (9 mm radius spheres) were chosen through direct viewing of anatomy in Analyze, choosing regions over superficial central sulcus (motor) and extra-striate cortex (visual). The BOLD signal within each seed volume was then used to make a correlation map in the same manner as with DOT (see Section 5.2.3). For visualization, correlation coefficients were mapped to the fiducial surface segmentation in Caret [Van Essen et al., 2001].

5.2.3 Correlation Statistics

The following random-effects analysis was conducted for each contrast separately. Correlations between time traces were calculated using the Pearson correlation coefficient, r, which is displayed in the correlation images. To examine the significance of the inter-hemispheric correlations within the motor and visual networks as measured with fcDOT, I constructed two sets of inter-hemispheric r-values (motor-to-motor and visual-to-visual). Each set contained seven values: one r-value each per scan session. A third set of residual background correlation coefficients was created from the motor-to-visual r-values (all four possible seed-to-seed correlations averaged to one r-value per subject). The null hypothesis was then that each inter-hemispheric set was indistinguishable from the background set. This hypothesis was tested with a paired (within subject) Student's t-test. The t-statistics were converted to p-values using the right-tail of the distribution (i.e., we expected positive correlation within each network).

5.3 Results

With our extended DOT system, I simultaneously imaged with DOT arrays placed over the visual and motor cortices (Fig. 5.2a,b). Task paradigms were performed to locate the motor and visual cortices within each subject, yielding functional responses with high contrast-to-noise (Fig. 5.2c,d).

Spectral analysis of resting-state measurements (5 min) showed $1/f$ components as well as distinct peaks attributable to cardiac ($0.75-1$ Hz) and respiratory ($0.1-0.3$ Hz) frequencies (Fig. 5.3a shows an example Fourier transform from subject 2). Since the temporal sampling rate of the DOT system (10.8 Hz) is much higher than that of typical fMRI ($\approx$ 0.5 Hz), these physiologic confounds were not aliased into lower frequency bands. However, there are also vascular confounds from systemic auto-regulation that occur within the same frequency range as RSN correlations. Using 1^{st}-nearest neighbor measurements that have minimal penetration into the brain, I constructed measures of each pad's scalp hemodynamics (Fig. 5.3b). Every channel had the superficial/global signal removed by regression and was band-pass filtered ($0.009-0.08$ Hz). These obscuring signals constituted on average 37% of deeper channels' power in the low-frequency functional connectivity regime. Image reconstruction then allowed the localization of brain physiology, resulting in voxel time courses that are unobscured by systemic confounds (Fig. 5.3c). The goal was to distinguish between systemic and local physiologic sources of low-frequency variations, allowing us to perform correlation mapping solely on the latter.

With the aid of the functional responses, seeds regions (1 cm^3) were chosen for use

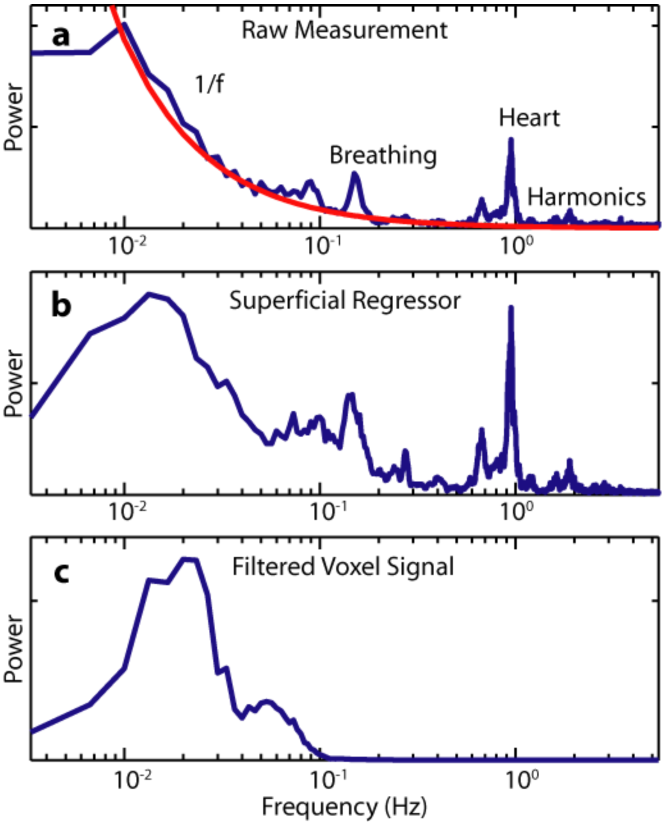

Figure 5.3: Power spectra of resting-state DOT signals (ΔHbO_2) (a) Spectral power of a single 2^{nd}-nearest-neighbor resting-state time trace, sampling both brain and superficial tissues, before the application of any filters (5 min, subject 2). The low-frequency components follow a $1/f$ curve (red), and there are peaks at the respiratory (0.16 Hz) and cardiac rates (0.95 Hz). (b) Spectral power of the superficial regressor derived from all 1^{st}-nearest-neighbor measurements in the visual pad. These systemic low-frequency fluctuations are removed from the data prior to performing functional connectivity mapping. (c) Spectral power of a filtered imaged signal (5 min from a single voxel under the measurement in (a)). This remaining spectral power within the desired frequency range is used to perform fcDOT. All traces have been smoothed with a moving average filter, width 5 voxels.

in correlation analysis (Visual: Fig. 5.4a,d, Motor: Fig. 5.4g, j; this figure shows data from subject 1). From each seed region, the time traces of ΔHbO_2, ΔHbR, and ΔHbT during resting-state brain activity were extracted. I then determined the correlation coefficient between these seed regions and every other cortical voxel's time course. For the visual cortex seeds, the images show that each seed region was correlated with the surrounding cortex, the more lateral cortex, and the contralateral cortex (Fig. 5.4b,e). In addition, the visual cortex seeds were uncorrelated with the motor cortex (Fig. 5.4c,f). Similarly, correlation mapping for the motor cortex seeds resulted in symmetrical correlation profiles with the contralateral motor cortex (Fig. 5.4i,l), but not within the visual cortex (Fig. 5.4h,k).

We investigated the repeatability of the fcDOT results through repeated mapping of the same subject. Correlation analysis from three sessions showed that the patterns were qualitatively similar over multiple days (Fig. 5.5). In addition, robustness was assessed with images acquired across a total of five subjects, all showing comparable connectivity patterns (Fig. 5.6 shows three subjects). The average of the functional connectivity maps from all seven sessions shows inter-hemispheric correlations in both the motor and visual networks with low crosstalk between the two networks (Fig. 5.7).

fcDOT analysis was repeated with all three hemodynamic contrasts. All the resulting correlation maps had the same pattern of inter-hemispheric correlations (Fig. 5.8a-c shows examples from subject 1). However, ΔHbT shows qualitatively lower spatial localization and more areas of negative correlation. In order to assess the statistical significance of the correlations within the visual and motor cortices, we repeated our fcDOT imaging and correlation analysis across seven scanning sessions (five subjects total, three sessions in subject 1). These data were evaluated with a random-effects model using the seed-to-seed correlation coefficients from all three hemodynamic contrasts. The group sets of inter-hemispheric correlation coefficients

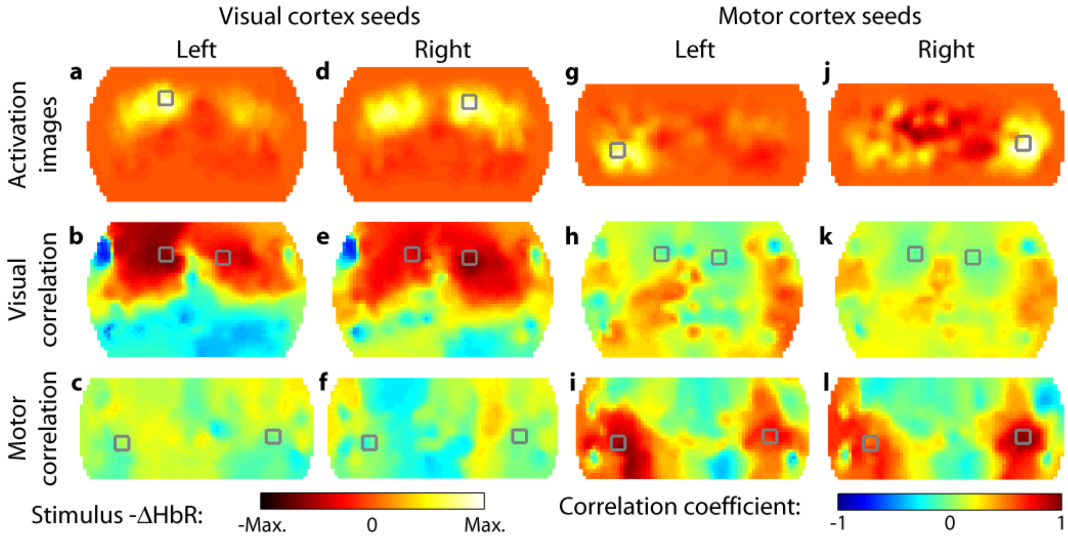

Figure 5.4: fcDOT using correlation analysis (ΔHbR, subject 1, session 1). (a) A functional response in the left visual cortex. There is a decrease in HbR with high contrast-to-noise. The response is scaled to its maximum contrast (scale reversed so decreases in HbR are positive contrast). The left visual cortex seed is defined by the gray box. (b) Correlation map in the visual cortex using the left visual cortex seed. There is correlation with both hemispheres of the visual cortex, but not with the lower region of the pad. Boxes for both right and left seed regions are shown. All correlation images scale from $r = -1$ to 1. (c) Correlation map in the motor cortex using the left visual cortex seed. The correlation throughout the field-of-view is low. Both right and left motor seed boxes are shown for reference. (d-f) fcDOT using the right visual cortex seed. Note the similar pattern to the left visual seed. (g-i) fcDOT using the left motor cortex seed. Note the high inter-hemispheric correlation in the motor cortex, but lack of any high correlations with the visual cortex. (j-l) fcDOT using the right motor cortex seed. Note the similar pattern to the left motor seed.

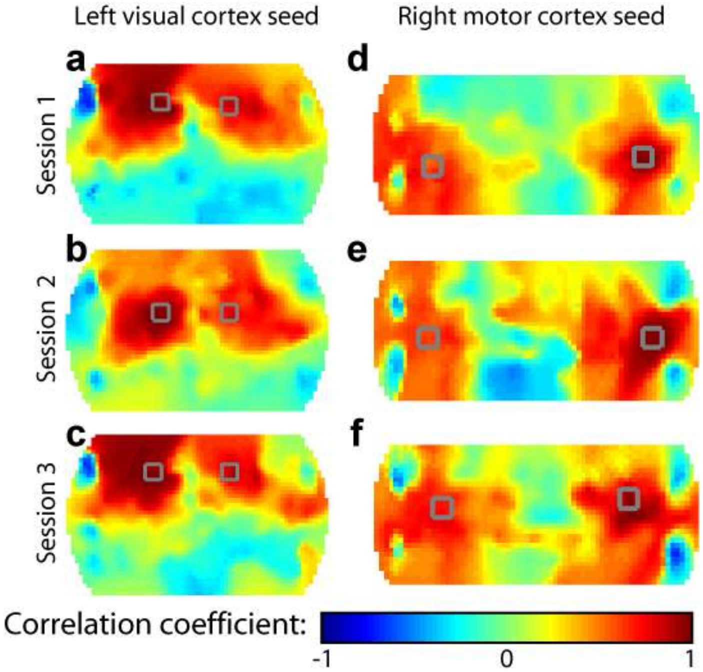

Figure 5.5: Repeatability of fcDOT over multiple imaging sessions (subject 1, ΔHbR). Seed boxes are shown in gray. Images from different sessions are not co-registered. (a-c) Correlation maps within the visual cortex from the left visual cortex seed. (d-f) Correlation maps within the motor cortex from the right motor cortex seed. Note the similarity in the patterns in each session (with slight linear translations between days).

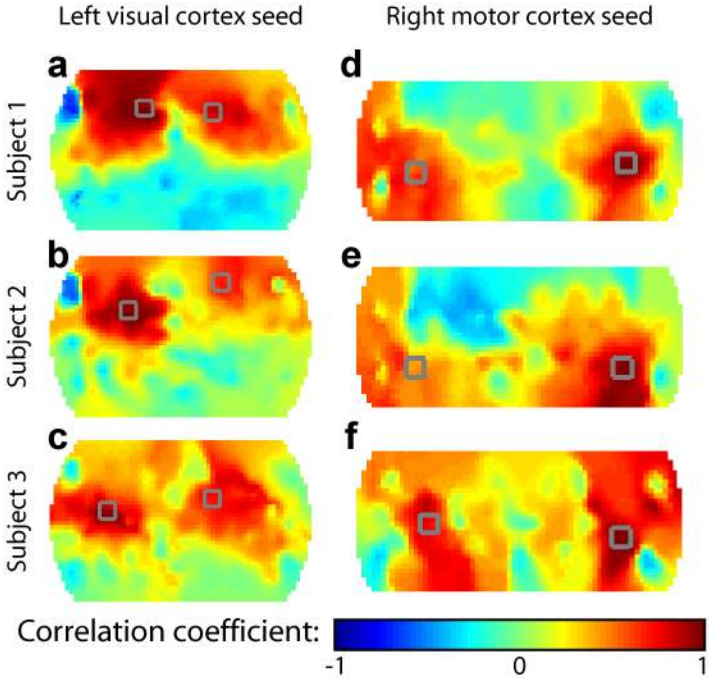

Figure 5.6: Robustness of fcDOT mapping in multiple subjects (ΔHbR). Seed boxes are shown in gray. For subject 1, session 1 is shown. (a-c) Correlation maps within the visual cortex from the left visual cortex seed. (d-f) Correlation maps within the motor cortex from the right motor cortex seed. All subjects have of high inter-hemispheric connectivity in both networks.

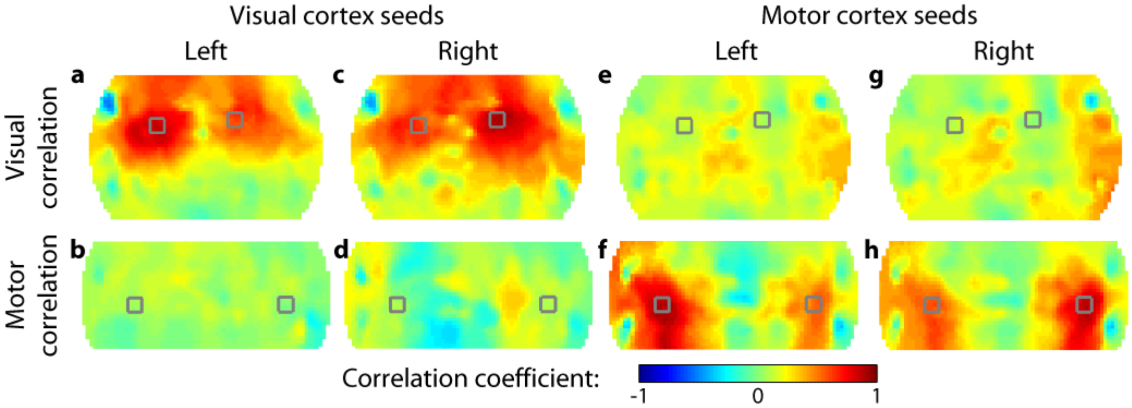

Figure 5.7: Multi-session average of all fcDOT correlation maps (ΔHbR). (a) Correlation map in the visual cortex using the left visual cortex seed. There is correlation with both hemispheres of the visual cortex, but not with the lower region of the pad. Boxes for both right and left seed regions are shown. All correlation images scale from $r = -1$ to 1. (b) Correlation map in the motor cortex using the left visual cortex seed. The correlation throughout the field-of-view is low. Both right and left motor seed boxes are shown for reference. (c, d) fcDOT using the right visual cortex seed. Note the similar pattern to the left visual seed. (e-h) fcDOT using the motor cortex seeds. Note the high inter-hemispheric correlation in the motor cortex, but lack of any high correlations with the visual cortex.

were compared against the set of visual-to-motor correlation coefficients within each contrast (Fig. 5.8d). The correlations were most robust in ΔHbR and were also significant in $\Delta\mathrm{HbO_2}$; ΔHbT had the largest standard deviations and highest p-values, but still had statistically significant inter-hemispheric correlations (Table 5.1). If, however, we do not remove channels with poor signal-to-noise and do not regress out superficial hemodynamic oscillations that allow us to localize neural activity (see Section 2.3.2), then the correlation p-values increase by two orders-of-magnitude (Table 5.2). The correlation maps created without signal-to-noise reduction are dominated by artifact structure due to corruption by measurements with poor signal-to-noise. In addition, the resulting maps have globally high correlations, showing that systemic physiology can obscure local variations. These maps do not localize neural activity or map functional connectivity (Fig. 5.9).

Table 5.1: Seed-to-seed correlation significance (p-values) with fcDOT.

	$\Delta\mathrm{HbO_2}$	ΔHbR	ΔHbT
Visual	2.1×10^{-3}	1.7×10^{-4}	2.2×10^{-2}
Motor	4.1×10^{-4}	9.4×10^{-4}	7.1×10^{-3}

Table 5.2: Seed-to-seed correlation significance (p-values) with fcDOT without superficial signal regression and without removing noisy channels from the reconstruction.

	$\Delta\mathrm{HbO_2}$	ΔHbR	ΔHbT
Visual	0.08	0.04	0.17
Motor	0.23	0.12	0.80

For further validation, the results of fcDOT (subject 1, session 1) were compared against those obtained from the same subject with (non-simultaneous) fcMRI. Measuring the position of the DOT imaging pads relative to external anatomic landmarks

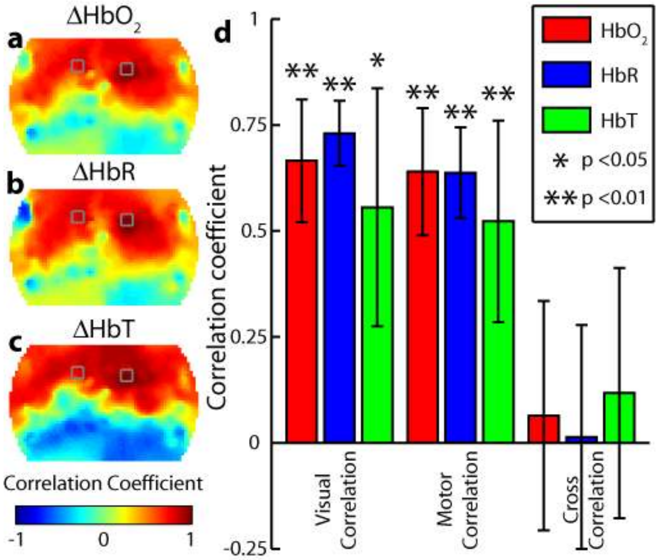

Figure 5.8: fcDOT analysis with all three hemoglobin contrasts (ΔHbO_2, ΔHbR, and ΔHbT). (a-c) Visual correlation maps from the right visual cortex seed for each of the three contrasts (subject 1, session 1). Seed regions are shown in gray. The maps for ΔHbO_2 and ΔHbR are very similar. The map for ΔHbT is less localized, has more regions of negative correlation, and is more variable from subject-to-subject. (d) Correlation coefficients across multiple subjects and days for all three contrasts (mean and standard deviation). The *p*-value comparing each inter-hemispheric correlation to the visual-to-motor correlation within each contrast is shown. Visual and motor networks are significantly correlated with all three contrasts, while there is little correlation between the visual and motor cortices.

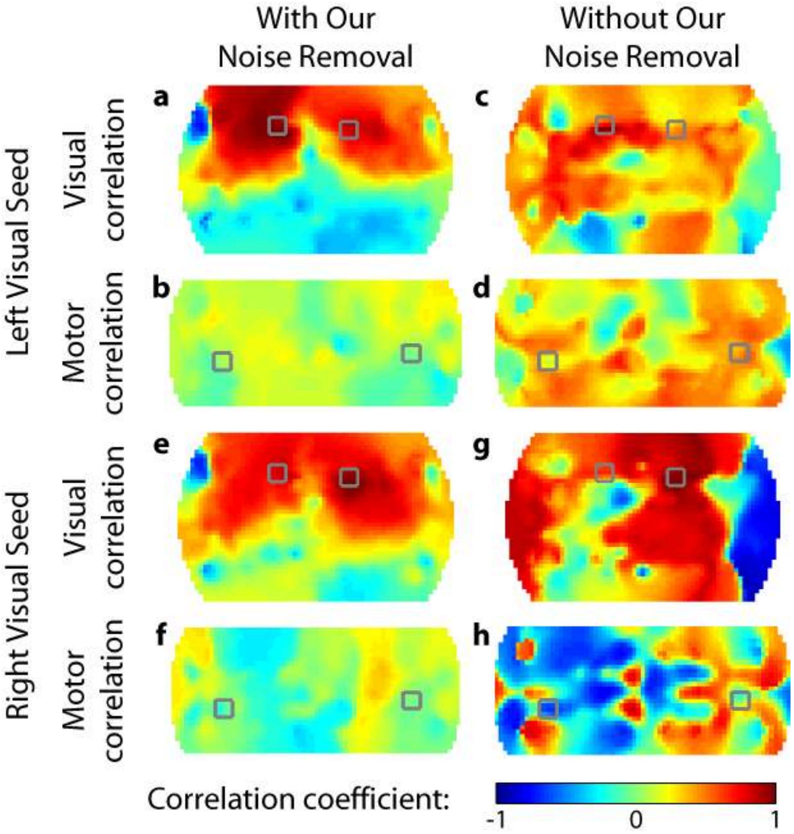

Figure 5.9: fcDOT with and without our regression and signal-to-noise improvement techniques (ΔHbR, subject 1, session 1). (a,b) Correlation maps in the visual and motor cortices using the left visual cortex seed with regression and noise removal. (The same images as Fig. 5.4b,c.) (c,d) Correlation maps using the left visual cortex seed without regression and noise removal. While this is the same raw data as (a) and (b), we now see global high correlations due to systemic confounds and artifact structure (possibly from coupling to optode motion) that obscures any underlying structure. Note the lack of any local correlation structure and the high correlations with the motor cortex. (e,f) Correlation maps using the right visual cortex seed with regression and noise removal. (The same images as Fig. 5.43e,f.) (g,h) Correlation maps using the right visual cortex seed without regression and noise removal. While this is the same raw data as (e) and (f), we now lack the local correlation pattern seen in (e).

(inion and nasion) and locating these features in an anatomic MRI confirmed that the DOT imaging pads were interrogating the visual and motor cortices (Fig. 5.10a,b). The seed-to-seed correlation coefficients generated by fcDOT analysis were similar to those from fcMRI (Fig. 5.10c,d). Both correlation matrices show high inter-hemispheric (within-network) correlations (Table 5.3). The motor-to-visual correlations were approximately zero with both methods (Table 5.3, mean and standard deviation are shown as there are four inter-network seed-to-seed correlations). Correlation images were also generated with resting-state fMRI data and the results are qualitatively similar to those from fcDOT in both the motor and visual cortices (Fig. 5.11).

Table 5.3: Comparison of fcDOT and fcMRI correlation coefficients (r).

	fcDOT	fcMRI
Inter-hemispheric Visual	0.80	0.70
Inter-hemispheric Motor	0.68	0.79
Visual-to-Motor	-0.03 ± 0.04	0.00 ± 0.07

5.4 Discussion

We hypothesized that we would be able to measure functional connectivity within the visual and motor networks using DOT. From fMRI reports and from our fcMRI studies, both networks exhibit high levels of inter-hemispheric correlation [De Luca et al., 2006, Damoiseaux et al., 2006]. In addition, the motor and visual cortices are members of distinct functional networks, and should be uncorrelated with each other.

This hypothesis is supported by the present fcDOT imaging results. The stimuli resulted in symmetric functional responses. Then, with resting-state analysis, we saw high correlations bilaterally in the same regions as the task-related responses. The

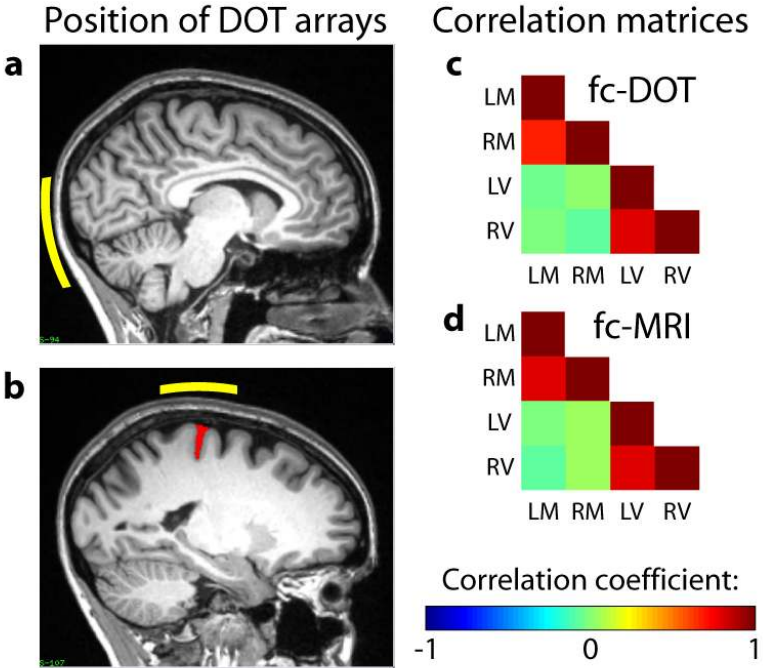

Figure 5.10: Comparing fcDOT with fcMRI. (a) Sagittal slice (5 mm left of midline) from subject's anatomical MRI with schematic of the visual cortex DOT pad superimposed (yellow), showing its position over the visual cortex. (b) Sagittal slice (18 mm left of midline) from an anatomical MRI with schematic of the motor cortex DOT pad superimposed (yellow), showing its position over the central sulcus (red). (c) Cross-correlation matrix for all four seeds from fcDOT imaging (LM: left motor cortex, RM: right motor cortex, LV: left visual cortex, RV: right visual cortex). Note the high inter-hemispheric correlations and low correlations between the motor and visual networks. (d) Cross-correlation matrix for all four seeds from fc-fMRI imaging. Note the similarity to the fcDOT correlation matrix.

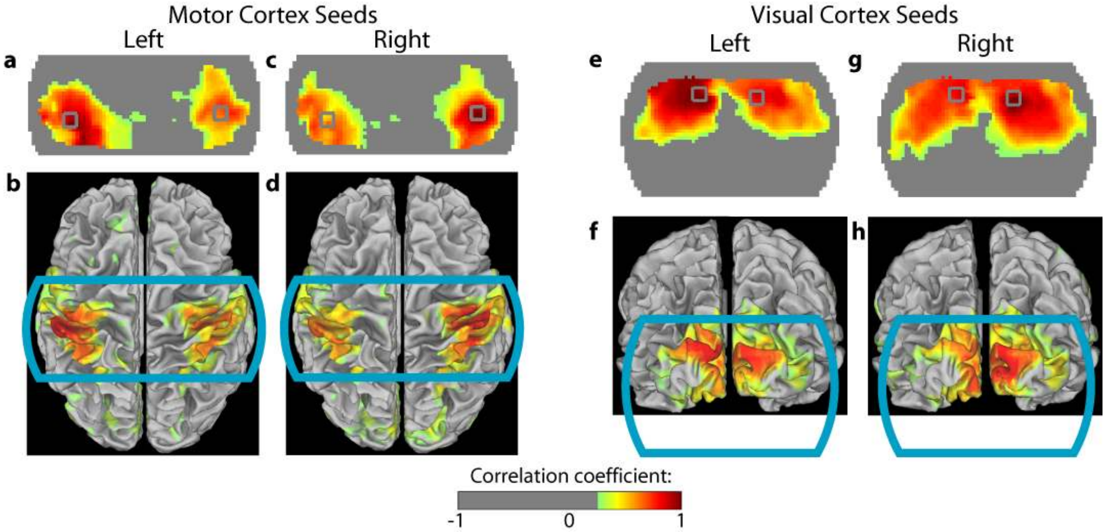

Figure 5.11: Similarity of correlation maps from fcDOT (subject 1, session 1) and fcMRI (subject 1). (The color scale has a threshold at $r = 0.25$, and areas around the edges of the DOT image reconstruction with poor sensitivity have been removed.) (a) fcDOT correlation map using the left motor cortex seed. (b) fcMRI correlation map, dorsal view, using the left motor cortex seed. The DOT motor imaging pad's position is shown in cyan. (c,d) fcDOT and fcMRI (dorsal view) using the right motor cortex seed. (e,f) fcDOT and fcMRI (posterior view) using the left visual cortex seed. (g,h) fc- DOT and fcMRI (posterior view) using the right visual cortex seed. Note the similarity of the fcDOT and fcMRI connectivity maps for all four seeds.

correlation maps are slightly broader than the task-response maps. This difference may be due to association with brain regions involved with higher-order processing; while these regions might not respond as strongly to the simple task paradigms, they may still correlate strongly in the resting-state. Additionally, the sensitivity of DOT imaging is lower near the pad edges, but the correlation analysis normalizes out differences in contrast, allowing the correlation maps to extend more fully to the margins of the field-of-view. Other interesting features in the visual cortex images were the lower correlation along the midline (where we expect the superior sagittal sinus) and the flat region of low correlation along the bottom of the imaging domain (cerebellum, which should be uncorrelated). Additionally, the fcDOT maps showed low correlation between the two pads, demonstrating the expected independence of the two networks. Thus, these fcDOT results produced the pattern predicted by fMRI and seen with our own subject-matched experiment.

Future fcDOT studies will benefit from the use of stereotactic coordinates and atlases in order to align and combine multi-subject data. This could be accomplished with more precise registration of the imaging pads to anatomic landmarks followed by an affine transform to an atlas space, as in fMRI. It is worth noting, however, that the ability to make robust maps on single subjects, as demonstrated in this work, is an essential step towards clinical neuroimaging, where a group-average image would be less helpful than a detailed scan of a particular patient.

In this study, I performed functional connectivity mapping using seed-based correlation analysis on image sequences band-pass filtered between 0.009 and 0.08 Hz. We chose this methodology in order to correspond to the processing stream in [Fox et al., 2005], and these particular filter limits remain common in fcMRI processing. There are other methods for preprocessing functional connectivity data. For example, removing linear trends and use a 0.1 Hz low-pass filter while continuing to use seed-based correlation analysis. Furthermore, one could use independent component analysis (ICA) to discriminate networks without assumptions about seed locations [De Luca et al., 2006, Greicius et al., 2004, Damoiseaux et al., 2006, Fransson et al., 2007]. Since DOT's sensitivity to vascular compartments and sampling of systemic hemodynamics differs from those of MRI, the evaluation of different processing methods within the context of fcDOT deserves future study.

Both fcMRI and fcDOT must remove global confounds and nuisance signals. Differences in the sensitivity and field-of-view of the two methods led to different regression steps preceding computation of the functional connectivity maps. For fcMRI, the processing included regressions of the global signal, the white matter signal, and the ventricular signal. In contrast, DOT has only limited depth sensitivity and is unlikely to suffer artifacts from white matter and the ventricles. However, DOT measurements will be corrupted by hemodynamics in the scalp and skull as well as by slow global fluctuations due to auto-regulation [Franceschini et al., 2006, Obrig et al., 2000]. To remove these confounds, we regressed out a signal derived from superficial measurements. This signal contains systemic hemodynamic variations as well as physiology located within the scalp and skull. This method increases the brain-specificity of the DOT method and permits the functional connectivity analysis of local cerebral hemodynamics.

Recently, controversy has surrounded the effects of systemic respiratory and cardiac variations on fcMRI networks [Birn et al., 2008, Shmueli et al., 2007]. While we believe that these artifacts have only small effects on fcMRI mapping, the widespread adoption of functional connectivity techniques will be aided if the mechanisms, relationships, and strengths of different spontaneous signals were better understood. Cardiac and breathing pulsations affect resting-state measurements due to fMRI's low temporal sampling rate (a typical repetition time (TR) is 2.5 s), which causes high-frequency systemic physiology to be aliased into the low-frequency regime in an uncontrolled manner [Lowe et al., 1998, Lund et al., 2006]. In contrast, our DOT system images its entire field-of-view every 93 ms, meaning that the carrier frequencies for cardiac and respiratory variations are unlikely to be aliased into lower-frequency bands where the functional connectivity signal is found and can be removed with simple low-pass filters. Thus, the RSNs found with fcDOT can be more confidently ascribed to be free of aliasing artifacts.

There were small differences between correlation maps determined with different hemodynamic contrasts: the functional correlations were strong in ΔHbO_2 and ΔHbR, but noisier and less localized with ΔHbT. Since DOT instrument noise appears in the absorption measurements at each wavelength and physiologic noise appears in cerebral blood volume (CBV) and oxygen saturation (S_tO_2), with these preliminary results, the propagation of noise into the different contrasts is complicated. Future studies will be required to make physiological judgments about the origins of these mapping differences.

The ability of discover maps in all three contrasts offers opportunities beyond those of BOLD-fMRI. Previous stimulus-response studies have found differences between images from the three contrasts, usually showing advantages to ΔHbT for functional mapping, including a tighter correlation to cerebral blood flow (CBF) and potentially better spatial localization [Devor et al., 2005, Culver et al., 2005, Sheth et al., 2004]. While BOLD is primarily venous sensitive, each optical contrast can have different compartmental sensitivity [Dunn et al., 2005]. In addition, while fcMRI maps (primarily dependent on HbR) could have been due to fluctuations in either CBV or S_tO_2, our results show that maps are present in both CBV and S_tO_2. Our fcDOT methods can in principal be extended to laser speckle measures of CBF, and future systems could provide simultaneous assessment of CBF, oxygen extraction fraction, and cerebral metabolic rate of oxygen consumption.

Non-invasive optical techniques can also be combined with direct measurements of systemic physiology, such as pulse and respiration rates and blood pressure, as was performed by Franceschini et al. [2006]. While, in this work, I removed systemic fluctuations in order to improve local neuronal specificity, Franceschini et al. showed that correlations to physiological measurements can reveal information such as the flow of blood pressure waves through the circulation. Due to DOT's high sampling rate, similar analysis can be performed at higher frequencies (e.g., at the respiration and pulse rates). Future studies that evaluate these systemic physiologic correlation maps, in combination with the functional connectivity methods demonstrated herein, could help elucidate the effect of the vascular tree on resting-state signals. DOT also does not interfere with electrical recording techniques, allowing studies that more directly compare resting-state neuronal and vascular activity than are currently possible [He et al., 2008]. All of these techniques should allow fcDOT to gain insight into the origins of the functional connectivity signal and to improve knowledge of extraneous sources of variance in optical and MRI studies.

These results demonstrate the successful application of functional connectivity methods to DOT of adult human subjects. My results validate DOT functional connectivity methods (fcDOT) within a model system established by fMRI. Such an approach increases our confidence in the fidelity of fcDOT, providing a strong foundation for moving RSN analysis beyond the studies that fMRI is capable of performing.

Chapter 6

Bedside fcDOT in Neonates

6.1 Introduction

Poor neuro-developmental outcomes in premature infants are a major clinical concern. As advancements in perinatal and neonatal intensive care have greatly improved overall survival, a significant portion of these at-risk infants are surviving with long-term motor, cognitive, behavioral, or emotional deficits, including cerebral palsy, visual impairment, and learning disability [Allen, 2008, Larroque et al., 2008, Marlow et al., 2005]. Traditional neuroimaging modalities have provided valuable cross-sectional, anatomical information of the developing brain, but there is a great clinical need for assessing brain function in real-time, safely, and at the bedside. Routine electroencephalography (EEG) monitoring is far from being a standard of care for preterm infants and often requires specialized training for proper interpretation. In addition, its spatial resolution is too poor to be able to resolve regional brain activity. Anatomic magnetic resonance imaging (MRI) can detect large structural injuries [Latal, 2009, Ment et al., 2009] but is an indirect measure of brain function.

Currently, the gold standard for functional neuroimaging research is functional magnetic resonance imaging (fMRI) with blood oxygenation level dependent (BOLD) contrast. However, fixed scanners and strong magnetic fields make it difficult to transport critically ill neonatal intensive care unit (NICU) patients for scans. Thus, for lack of useful tools for assessment, it is hard to determine how treatments affect brain function and development or to detect injury early enough for treatment to be an effective.

In recent years, there has been an increasing number of studies using DOT and NIRS to examine task-induced responses in infants (Fig. 6.1) [Karen et al., 2008, Liao et al., 2010, Meek et al., 1998, Taga et al., 2003, Gibson et al., 2006]. While this research has increased knowledge of neonatal development and has advanced the design of optical neuroimaging systems, such task-based activation paradigms are of limited clinical utility. Infants are unable to perform many cognitive tasks, and having them attend to any task is difficult. To move beyond this conceptual barrier, we looked to resting-state functional connectivity to map brain networks even in the absence of task-performance (Chapter 5). Clinical adaptation of this technique would thus be ideal for neonates or unconscious patients.

The fMRI community has been moving forward with clinical application of fcMRI [Kiviniemi, 2008]. However, their efforts have focused on those population better suited to fMRI scanning, namely mobile patients such as those with Alzheimer's [Buckner et al., 2009, Greicius et al., 2004], depression [Greicius et al., 2007], or schizophrenia [Calhoun et al., 2008]. There have been additional studies examining brain activity in comatose, but stable patients [Boly et al., 2009, Vanhaudenhuyse et al., 2010]. However, the difficulties of scanning NICU infants with fMRI preclude easy clinical scanning. The number of fcMRI studies of neonatal cognitive development is limited, with difficulties in the ability to scan longitudinally and without sedation [Fransson et al., 2007, 2009, Smyser et al., 2010]. Furthermore, one cannot

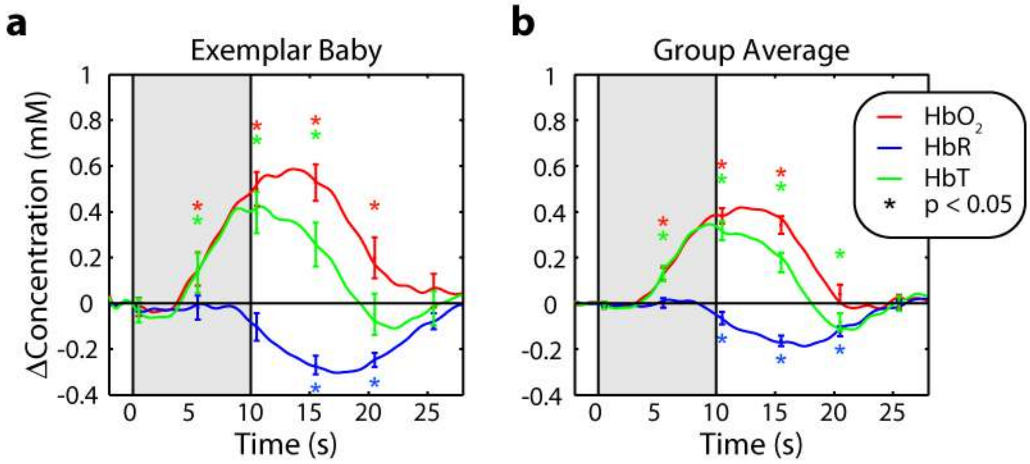

Figure 6.1: Functional activations in the visual cortex of neonates measured with high-density NIRS. (a) Block-average of an activation due to a full-screen visual stimulus (times in gray) in a newborn term infant. High-density measurements were used to regress superficial signals, but no reconstruction was done; this trace is an average of all 2nd-nearest neighbor source-detector measurements corrected for diffuse path length. Error bars show standard deviation and asterisks indicate significant deviations from pre-stimulus baseline. (b) Results from the same experiment averaged over all infants. Note that term infants have a similar hemodynamic response function to adults (Fig. 1.3b) with a possibly slightly delayed HbR response.

predict when injuries occur, thus making such measurements of single developmental time points less useful. A methodology enabling frequent longitudinal scans at the bedside is necessary for possible diagnostic use.

In this chapter, I apply fcDOT to bedside imaging of neonates within the first month of life. I show the first fcDOT images in infants and how these maps can be disrupted through brain injury. If these proof-of-concept results are extended, we expect that fcDOT can become an important diagnostic and prognostic tool for neonatologists.

6.2 Methods

6.2.1 Protocol

Subjects were recruited from the nurseries of Barnes-Jewish and St. Louis Children's Hospitals. Informed consent was acquired from the infants' parents. The study was approved by the Human Research Protection Office of Washington University in St. Louis. We scanned 3 term and 5 premature infants. One preterm infant had a unilateral occipital stroke. Another preterm infant had significant non-neuronal injuries, but the anatomic MRI scan was mostly normal (some residual blood in the germinal matrix, but appropriate myelination). All other infants were healthy. The term infants were scanned during the first three days of life. Premature infants were scanned at various points during their hospitalized course. All infants were scanned in their bassinets or incubators while quietly resting or sleeping (although sleep state was not actively monitored) [Liao et al., 2010].

For this study, we used our custom-built high-density DOT system with an optode array consisting of 18 sources and 16 detectors (Fig. 6.2a). The cap consisted of flexible optical fiber bundles embedded in a silicone array. This soft pad was held against the head using neoprene straps and Velcro. The array was placed just above the inion, in order to scan the occipital (visual) cortex (Fig. 6.2b).

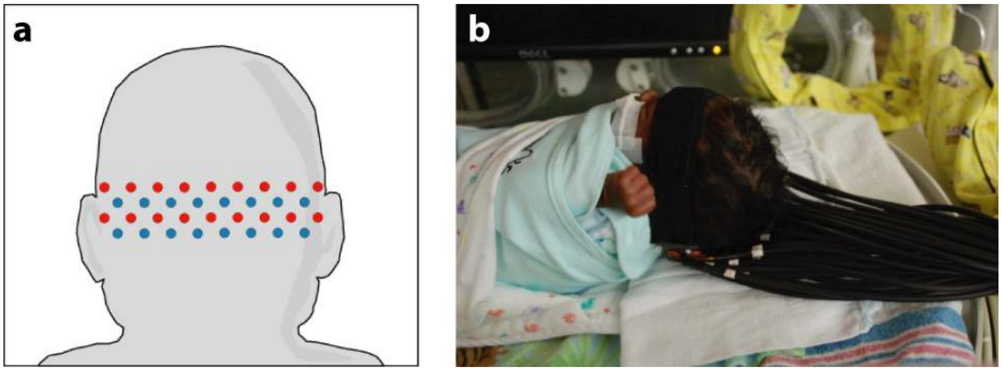

Figure 6.2: Bedside imaging of infants with DOT. (a) Schematic of the visual cortex imaging pad, with 18 sources (red) and 16 detectors (blue) placed over the occipital cortex of an infant. (b) Photograph of the optical probe on a premature infant in its NICU bassinet.

6.2.2 Functional Connectivity Data Processing

All data was processed as in Chapters 2 and 5. I analyzed resting-state brain function in two manners. First, regions of interest (ROIs) in the visual cortex were chosen based on the position of the pad relative to the anatomic landmarks. From these 1 cm^3 ROI positions, seed time traces were extracted for each of the three hemodynamic contrasts. These time courses were then correlated with every other pixel within the field-of-view to generate correlation (r) maps.

Second, I performed independent component analysis (ICA). After the imaging described above, I used FastICA to perform temporal ICA on the sequence on images, with the same preprocessing steps and non-linearity function as were used in our previous study of adult visual activations [Markham et al., 2009]. For each data set, I extracted 5 independent components, from which components corresponding to the visual resting-state network were chosen by visual inspection. This methodology is similar to that used in fcMRI studies using ICA [Damoiseaux et al., 2006] except that a smaller number of independent components were estimated due to our smaller field-of-view.

6.2.3 Low Frequency Power

The measurement of resting-state networks (using either seed-based of ICA methods) could be a powerful method for determining whether functional connections are developing normally. But, I also wondered whether we could see if a particular region of interest had an appropriate level of brain activity. Thus, I simply measured the variance of the hemoglobin time traces within each pixel over time (again, filtered to the 0.009 to 0.08 Hz frequency band associated with resting brain activity). Maps of variance should give us a measure of intrinsic brain activity within each voxel. Methods similar to this have recently been developed for examining brain aging with fMRI [Garrett et al., 2010].

6.3 Results

Data from the healthy term infants showed strong correlations between the two visual seeds in all three hemodynamic contrasts (Table 6.1). When the seed was placed in the left visual cortex, maps of correlation coefficients for each seed showed ipsilateral correlations as well as correlations with the contralateral visual hemisphere (Fig. 6.3a). Symmetric patterns were seen with the seed in the right visual hemisphere (Fig. 6.3b) Similar bilateral correlation patterns were seen in the visual cortices of other healthy term and premature infants (Fig. 6.3c-d).

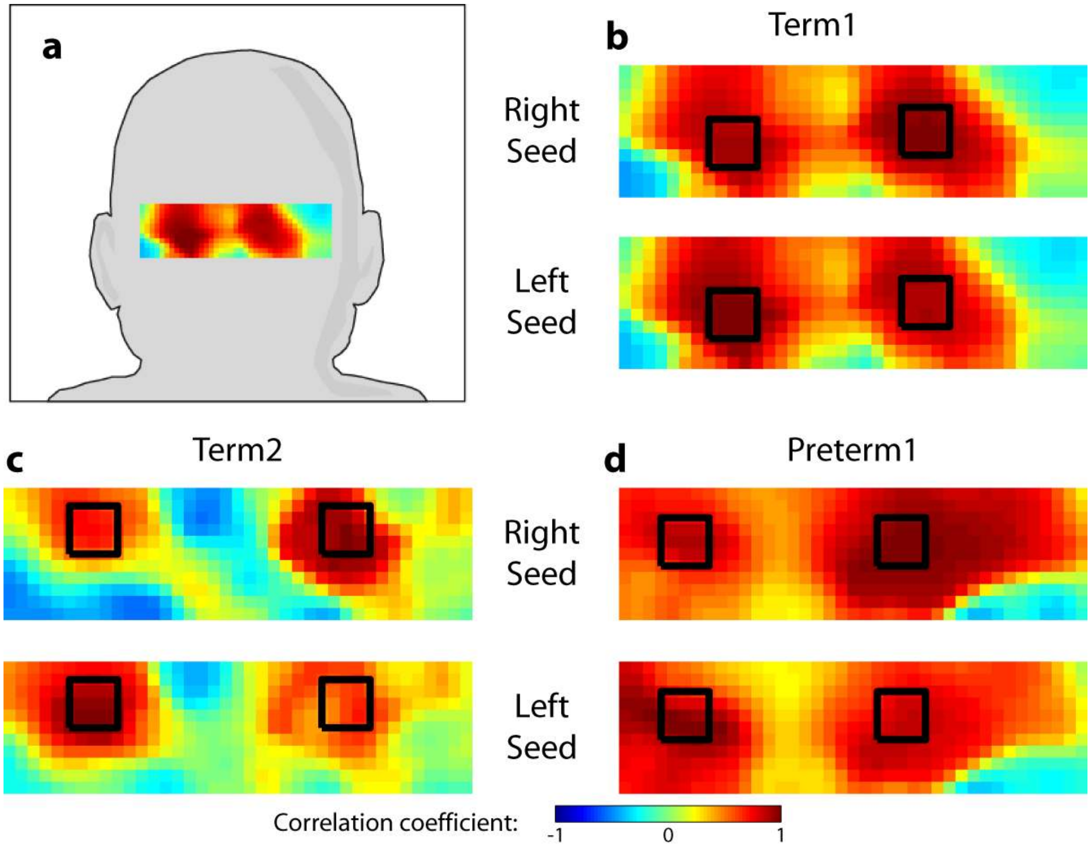

Figure 6.3: Neonatal fcDOT using correlation analysis in the visual cortex (HbO_2). (a) An fcDOT map placed over the occipital cortex of an infant head to show the field- and direction-of-view. (b-c) Correlation maps using seeds placed in the two visual hemispheres in healthy term infants. Note the strong ipsilateral and contralateral correlations. (All correlation images are scaled from $r = -1$ to 1.) (d) Correlation maps in the visual cortex of a healthy preterm infant, which also show strong bilateral correlation patterns.

Table 6.1: Inter-hemispheric visual correlation values (r) in infants.

Subject	HBO_2	HbR	HbT
Term1	0.92	0.90	0.89
Term2	0.64	0.57	0.63
Term3	0.75	0.88	0.63
Preterm1	0.85	0.85	0.74
Preterm2	0.66	0.55	0.78
Preterm3	0.60	0.49	0.89
Preterm 4 (Non-Neuronal Injury)	0.91	0.93	0.81
Preterm 5 (Occipital Stroke)	-0.04	0.00	-0.06

In addition to healthy infants, we also scanned two premature infants with complicated clinical courses. One had a large left hemisphere occipital stroke (Fig. 6.4a). In this infant, seeds placed in either the right visual cortex or on the left side of the imaging domain (where an operator naïve of the stroke would expect the left visual cortex) generated only unilateral correlation patterns (Fig. 6.4b). In all three contrasts the two seeds were uncorrelated (Table 6.1). This result shows that fcDOT is sensitive to neuronal injury, but we also desire a marker of disease that is specific. It would be less useful if functional connectivity maps were affected by non-neuronal, systemic injury. Thus, we also performed fcDOT on an infant that had a complicated clinical course, but with only minimal neurological sequelae. This analysis showed similar connectivity patterns to those in healthy infants (Fig. 6.5) and strong inter-hemispheric correlation coefficients (Table 6.1). A comparison of correlation values for all infant groups is shown in Fig. 6.6.

The seed-based method allows us to measure specific correlations, but can be sensitive to the exact placement of the seed location. So, I decided to also attempt to find the visual resting-state network using ICA. This method also showed bilateral components in both healthy term (Fig. 6.7a) and preterm infants (Fig. 6.7b). For some

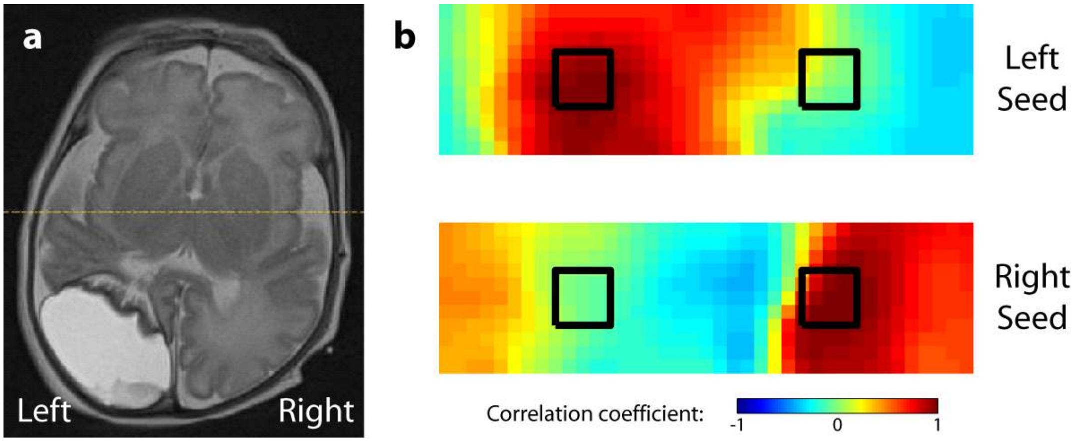

Figure 6.4: Neonatal fcDOT in a preterm infant with an occipital stroke (HbO_2). (a) An axial slice (neurological orientation) of a T2-weighted MRI of this infant showing the stroke. (b) Correlation maps using seeds placed where the left and right visual cortices are expected to be. In both cases, we see only unilateral correlations (all correlation images are scaled from $r = -1$ to 1).

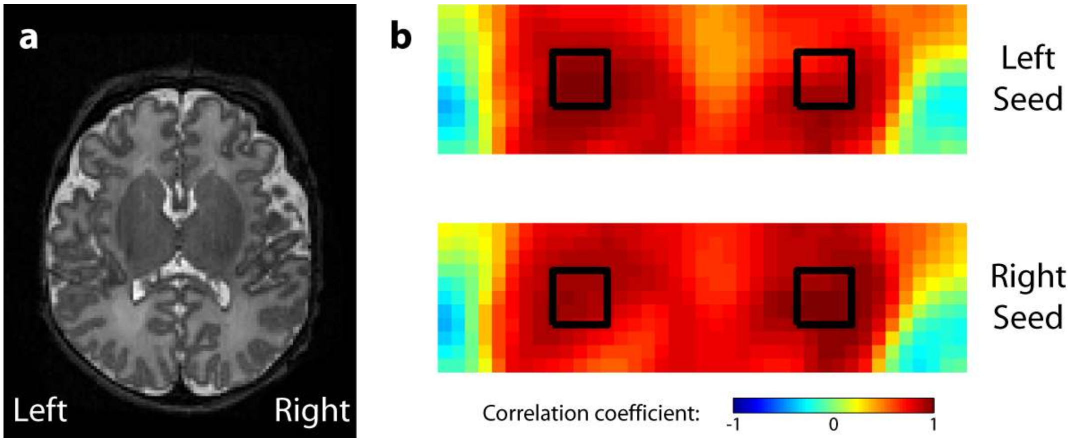

Figure 6.5: Neonatal fcDOT in a preterm infant with non-neuronal injury (HbO_2). (a) An axial slice (neurological orientation) of a T2-weighted MRI of this infant. (b) Correlation maps using seeds placed in the left and right visual cortices. We see the bilateral correlation patterns of a healthy visual cortex (all correlation images are scaled from $r = -1$ to 1).

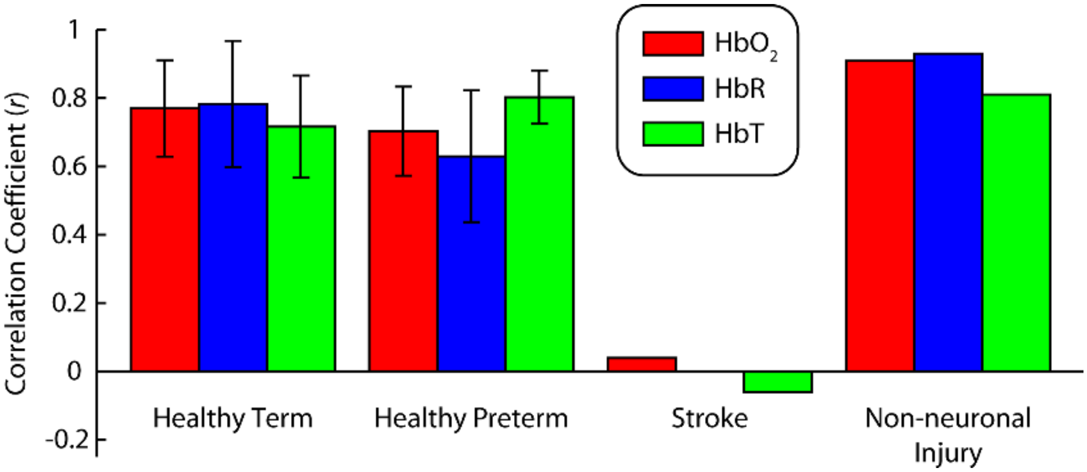

Figure 6.6: Average inter-hemispheric correlation coefficients for all population groups and all three contrasts, Error bars show standard deviation over subjects (except for groups with only one subject).

infants, ICA performs qualitatively better at localizing the visual cortex; perhaps, in this case, it did a better job of separating global artifacts. However, some infants showed less localized ICA (e.g., Preterm1, Fig. 6.7b); in this case, ICA perhaps picked a component that involved signal from the superior sagittal sinus. ICA of the images from the preterm infant with the occipital stroke showed a component with only unilateral coverage in the healthy hemisphere (Fig. 6.7c).

Both ICA and seed-based methods are able to find functional connectivity networks, in theory measuring the integrity of long-distance brain connections. I also wanted to know whether I could identify areas with appropriate brain function in a seed-independent manner. Examination of the power spectra of resting-state time traces of the left and right seeds showed that, in a healthy infant, the pattern of a $1/f$ curve (< 0.1 Hz), a respiration peak ($0.5 - 1.0$ Hz), and a pulse peak ($2 - 3$ Hz) is almost identical in both hemispheres (Fig. 6.8a). However, in the infant with the unilateral stroke, pulse and respiration were seen in both hemispheres, but the low frequency content was lower in the affected hemisphere (Fig. 6.8).

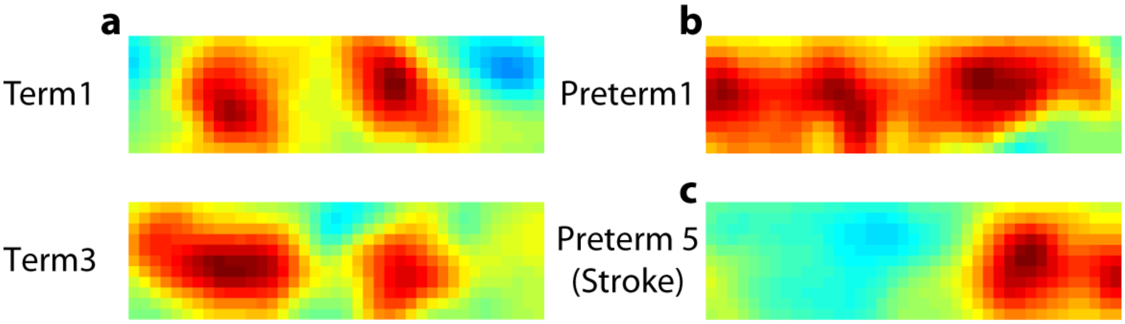

Figure 6.7: fcDOT of neonates using ICA (HbO_2). (a) Independent components in two term infants corresponding to a bilateral resting-state network (similar to Fig. 6.3b-c). (b) An independent component corresponding to the resting-state network in a healthy preterm infant (compare to Fig. 6.3d). (c) An independent component in the infant with the unilateral occipital stroke; ICA sees activity only in the healthy hemisphere (compare to Fig. 6.4c). (All components are scaled to their maximum, keeping zero at the center of the color scale, and the sign convention is that the strong "correlations" are positive; since ICA is unique only up to a multiplicative constant.)

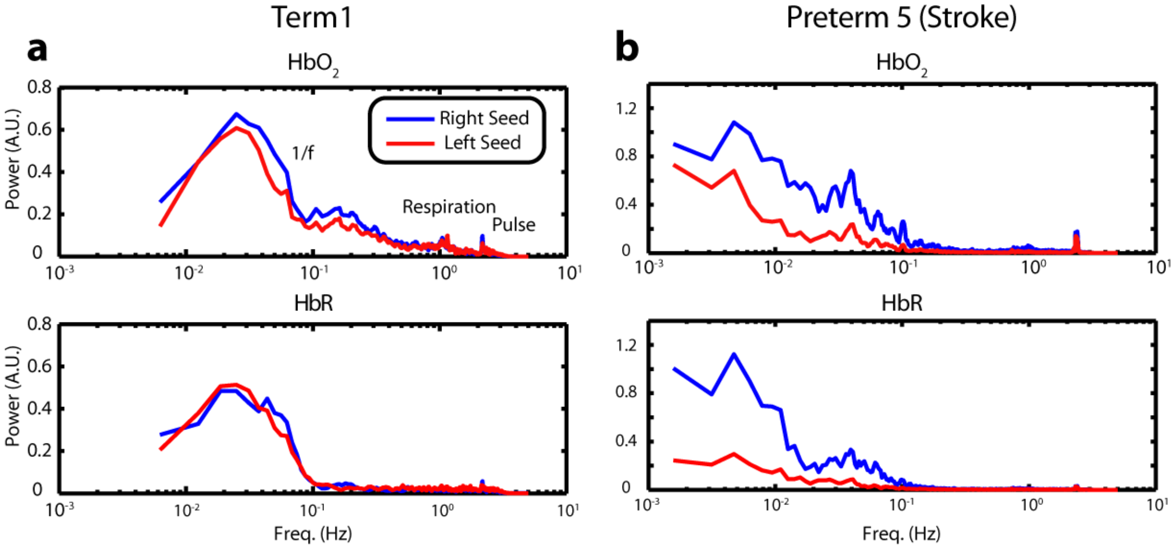

Figure 6.8: Resting-state DOT power spectra in neonates (HbO_2 and HbR). (a) In the healthy term infant we can see a $1/f$ curve as well as respiration and pulse peaks in both visual hemispheres. (b) In the infant with a left hemispherical stroke, we can still see systemic physiology in the affected hemisphere (pulse, respiration, and some $1/f$ fluctuations), but low frequency power is markedly lower, an indication of the lack of brain activity.

I hypothesized that decreased low frequency power was due to lower intrinsic brain activity. (As there are global physiological processes that also have $1/f$ spectra, we would not expect low frequency power to be completely abolished in the affected area.) So, I created maps where each pixel's value represents it's relative power in the frequency band corresponding to resting-state brain activity (0.009 – 0.08 Hz). With this analysis, we see high bilateral patterns of resting-state brain activity in the healthy term (Fig. 6.9a) and preterm infants (Fig. 6.9b) as well as the infant with non-neuronal injury (Fig. 6.9c). However, in the infant with the stroke, there is an asymmetric pattern with attenuated power in the stroke area (Fig. 6.9d).

6.4 Discussion

In this chapter, I have shown how functional connectivity can be acquired at the bedside in the nursery and neonatal intensive care unit with diffuse optical tomography. The networks that I have found extend our preclinical work in healthy adults and represent the first optical imaging of resting-state networks in infants. I demonstrated the presence of a bilateral visual resting-state network using both seed-based and ICA methods. This network appears in both preterm and term infants. This result is in agreement with previous fcMRI literature of infants [Fransson et al., 2007, 2009, Smyser et al., 2010], where although there is controversy about unilateral sensorimotor networks, the visual network is always reported as bilateral. These results serve to validate neonatal fcDOT in a well-studied network against the gold standard of fcMRI.

In contrast, in an fcNIRS study of infants [Homae et al., 2010], the authors only found a bilateral visual network develop at 3 months of age. It might be that their study did not see a visual network due to contamination from superficial artifacts,

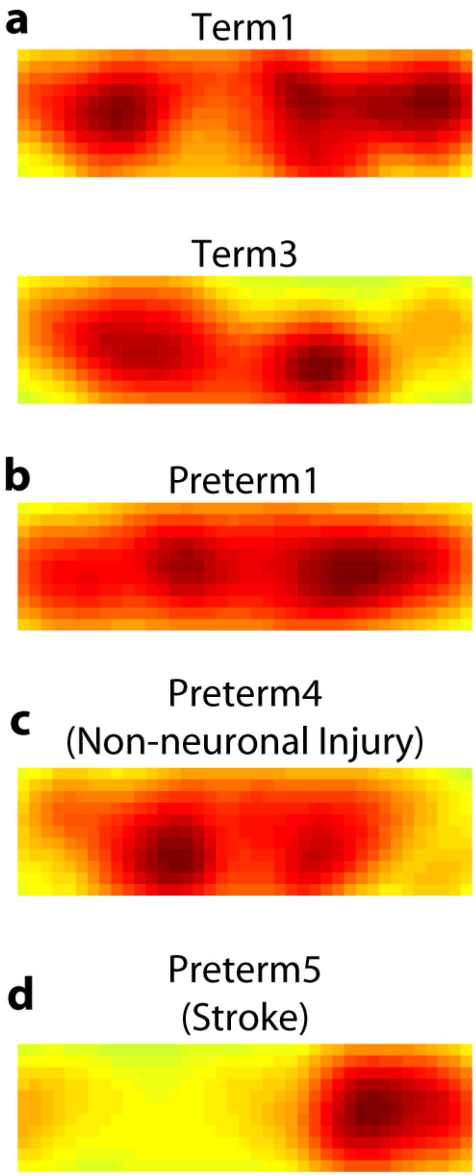

Figure 6.9: Mapping low frequency DOT power in neonates (HbR). (a) Maps of low frequency power in healthy term neonates. Note the bilateral pattern. (b,c) A similar bilateral power is seen in healthy preterm infants, and in the infant with non-neuronal injury. (d) In the low frequency power map in the infant, power is only seen in the healthy hemisphere.

which are of major concern in NIRS studies and can lead to spurious reporting of hemodynamic signals (see Section 2.3.2) [Boden et al., 2007, Gregg et al., 2010, Liao et al., 2010, Saager and Berger, 2008]. Within the context of functional connectivity, in our earlier study of adults, we did see that networks could be hidden by artifacts from both superficial/systemic contaminants and noise from optode motion (Chapter 5, specifically Fig. 5.9). It was in order to eliminate the artifacts of NIRS methods, that we chose to concentrate our measurements in a relatively small cortical area, achieving tomographic imaging with high signal quality (i.e., DOT). By doing so, we sacrifice the large spatial extent that can be covered by sparse NIRS arrays using an equivalent number of sources and detectors [Franceschini et al., 2006, Homae et al., 2010]. Future DOT systems will involve greater numbers of optodes, and thus be able to combine high quality imaging with large lateral fields-of-view.

Although, the visual cortex was a good starting point, it is not a cortical area that is especially vulnerable to injury in premature infants. Thus, in our future work we hope to extend our imaging to brain regions that are more clinically relevant, especially the motor network (of relevance to cerebral palsy) and the default mode network (which has seen growing interest in cognitive neuroscience). Despite the limitations of the visual cortex, the results shown here do show promise for the clinical utility of fcDOT. The bilateral correlation pattern seen in healthy infants is disrupted specifically by occipital cortex injury. This injury was observed both using seed-based methods and ICA. Here, the two methods played complementary roles. With the seed-based method, while we were able to see that the normal correlation pattern had been disrupted, we were unable to tell where the injury was located. With ICA we could see only a component corresponding to the right hemisphere with no corresponding component in the left hemisphere.

Although, in the case of the occipital stroke, the stroke is immediately obvious from a structural MRI, relying on structural MRI for diagnosis is not an ideal clinical scenario. First, it would be extremely difficult to predict when injury would occur. Thus, a method which can offer imaging at multiple time points at the bedside holds more promise for detecting potential indicators of developing injury. With longitudinal imaging, pre-injury conditions might be able to be detected before they have progressed to such an irreversible stage, thus allowing early intervention. Additionally, functional connectivity measurements might be able to detect more subtle injury, such as lower correlations due to white matter injury that could progress to cognitive deficits, but are not noticeable on anatomic imaging until far advanced.

In addition to functional connectivity, I also studied the possible role of maps of low frequency power. I hypothesized that such a measure would be a metric of each cortical area's function and could detect regions of injury independent of seed placement and without resorting to the more complicated algorithms of ICA. With this metric, we also saw bilateral patterns in healthy infants. In the infant with the occipital stroke, low frequency was present only in the healthy hemisphere. We expect that this technique could be a helpful clinical tool alongside more common functional connectivity measures. Low frequency power can be measured more continuously in all cortical locations without need for user input. More detailed measures of functional connectivity, checking for the integrity of networks, could be performed at various longitudinal time points or when deficits in intrinsic brain activity are suspected from the power maps.

In summary, I have shown that imaging of functional connectivity of both term and preterm neonates is possible within the clinical environment. Such tools could provide important diagnostic and prognostic information, allowing clinicians to assess brain function and track functional development at the bedside. Thus, the effects of various clinical interventions (such as ventilation strategies, nutrition, and pharmacological therapies) and perinatal risk factors (e.g. infections) on neural function can be monitored during hospitalization. Additionally, it might be possible to detect intracranial hemorrhage and white matter injury before damage has become too extensive. In these ways, fcDOT can complement the high-powered research potential of fcMRI with longitudinal bedside imaging.

Chapter 7

Conclusion

Despite optical brain imaging's unique capabilities and advantages, widespread acceptance in the neuroimaging and clinical communities has been hampered by low spatial resolution and image localization errors. I have shown that the recent technical developments in DOT provide a substantial advancement in neuroimaging capability. In particular, this higher performance approach enables the critical milestones of phase-encoded retinotopic mapping and resting-state network analysis. fcDOT methodology matches well with the goal of providing bedside, clinical neuroimaging. We are now moving forward with clinical applications of this technique and expect future fcDOT methods to longitudinally monitor brain function, to detect functional deficits, to follow brain maturation, and to provide prognostic information on future development. Such a DOT system would represent fundamental shift away from previous optical methods and would become an important imaging tool in the ICU and for preterm infants.

Appendix A

Functional Connectivity Optical Intrinsic Signal Imaging

A.1 Introduction

The development of functional neuroimaging techniques, particularly functional magnetic resonance imaging (fMRI) has revolutionized human cognitive neuroscience. However, while these advances have transformed the way that researchers study human brain function, they have also widened the divide between cognitive neuroscience and cellular neuroscience, which is often conducted in mouse models. This divergence stems from the difficulty in translating advances from one field to the other, in either direction. Performing fMRI in mice is almost prohibitively difficult due to poor signal-to-noise and low spatial resolution. Additionally, small animal MR scanners have to have very magnetic high field strength, which in turn leads to extremely high cost. Conversely, it is difficult to know how to look for fMRI correlates of key genes and proteins discovered from cellular research. These problems in bridging the two fields might remain unimportant while neuroimaging research is focused on normal human cognitive processing, however, they become more acute as the neuroimaging field moves towards the study of disease and clinical functional imaging.

A promising avenue to connect neuroimaging, clinical patients, and disease models is the measurement of intrinsic brain activity through resting-state functional connectivity [Biswal et al., 1995, Fox and Raichle, 2007]. The discovery that functionally-related areas have correlated neural and hemodynamic activity even in the absence of tasks means that brain networks can be studied even in brain-injury [Boly et al., 2009, Vanhaudenhuyse et al., 2010], under anesthesia [Vincent et al., 2007], or in neonates [Fransson et al., 2007, Smyser et al., 2010]. For example, recent studies by Buckner et al. [2009] and Seeley et al. [2009] have highlighted both the promises and difficulties of clinical functional connectivity MRI (fcMRI). Both studies showed evidence of the spatial relationships between the brain regions affected by dementia and resting-state networks. However, evidence for the connection remains circumstantial since patients can not be followed prospectively before the development of disease, and human genes can clearly not be modified to test hypotheses.

fcMRI has recently been extended to non-human primates [Vincent et al., 2007] and rats [Pawela et al., 2008, Zhao et al., 2008, Hutchinson et al., 2010]. While initial studies have shown promising results in clinical models [Pawela et al., 2010], the difficulty in conducting small animal MRI has prevented more such studies. Furthermore, to our knowledge, fcMRI methods have not been extended to mice, which are the primary genetic model of disease.

An alternative method for functional neuroimaging in small animals is optical intrinsic signal imaging (OIS) [Grinvald et al., 1986, Ts'o et al., 1990, Woolsey et al., 1996, Dunn et al., 2005, Martin et al., 2006]. OIS works by shining light onto the surface of the brain; changes in reflected light intensity are due to changes in local hemoglobin concentrations. Thus, neural activity can be measured through the neurovascular response in much the same way as in fMRI. Such systems have demonstrated high spatial resolution [Kalatsky and Stryker, 2003], spectroscopic sophistication [Dunn et al., 2003], and high speed [Bouchard et al., 2009]. Most OIS studies have focused on studying neurovascular coupling [Lindauer et al., 2001, Devor et al., 2003, 2005] and cortical columns [Bonhoeffer and Grinvald, 1991, Kenet et al., 2003]. To our knowledge, no one has attempted large field-of-view imaging of the entire superior surface of the mouse cerebral convexity, despite the fact that the mouse brain is unfolded, allowing a large surface to be viewed from above. Additionally, large field-of-view imaging does not require the high spatial resolution needed for columnar studies, removing the need for invasive skull thinning, removal, or replacement with cover slip windows.

In this chapter, I propose a new method for functional imaging of mice: functional connectivity optical intrinsic signal imaging (fcOIS). This method relies on simple and inexpensive camera-based equipment and requires only the reflection of the scalp, making it minimally invasive. Using OIS, I demonstrate the first functional connectivity maps in mice covering almost the entirety of the convexity (from the olfactory bulb anteriorly to the superior colliculus posteriorly and laterally to the edge of primary somatosensory cortex). Additionally, I show the power of the method through the use of functional connectivity data to parcellate the mouse cortex, mapping the spatial extent of multiple functional networks. We expect that these methods will be a widely useful tool, allowing the combination of genetic and surgical models in mice with the power of functional neuroimaging.

A.2 Methods

A.2.1 Animal Preparation

All procedures were approved by the Washington University School of Medicine Animal Studies Committee. A male ND4 Swiss Webster mouse (8-10 weeks of age, 25-30 g, Harlan Laboratories, Indiana) was anesthetized with a Ketamine/Xylazine mixture (100 μL/20 g) and allowed 30 min for anesthetic transition. The anesthetic dose was typical of those used in OIS studies of functional responses, maintaining blood gases within normal ranges. Anesthetic effect was verified by ensuring that the animal was not responsive to a hind paw pinch. Once induced, the animal's head was secured in a stereotactic frame using a nose cone and ear bars. Prior to surgery the fur on the head was removed with clippers and hair removal gel. A midline incision was made along the top of the head an the scalp was reflected, exposing approximately 1 cm^2 of the skull. This cranial window was kept moist with an application of water.

A.2.2 Imaging System

Sequential illumination was provided at four wavelengths by a ring of light emitting diodes (478 nm, 588 nm, 610 nm, and 625 nm; RLS-5B475-S, B5B-4343-TY, B5B435-30S, and OSCR5111A-WY, respectively, Roithner Lasertechnik) held at about 10 cm above the mouse's head. For image detection, we used a cooled EMCCD camera (Andor Technologies) set to an external trigger. The LED ring and the camera were controlled via computer using custom-written software. In order to acquire images at well above the heart and respiration rates ($\approx$ 10 and 2.5 Hz, respectively), we used a full frame rate of 30 Hz, which, with four temporally encoded wavelengths, required a camera frame rate of 120 Hz. In order to prevent specular reflection, crossed linear polarizers were placed just in front of the LEDs and the camera lens. A diagram of the system is shown in Figure A.1.

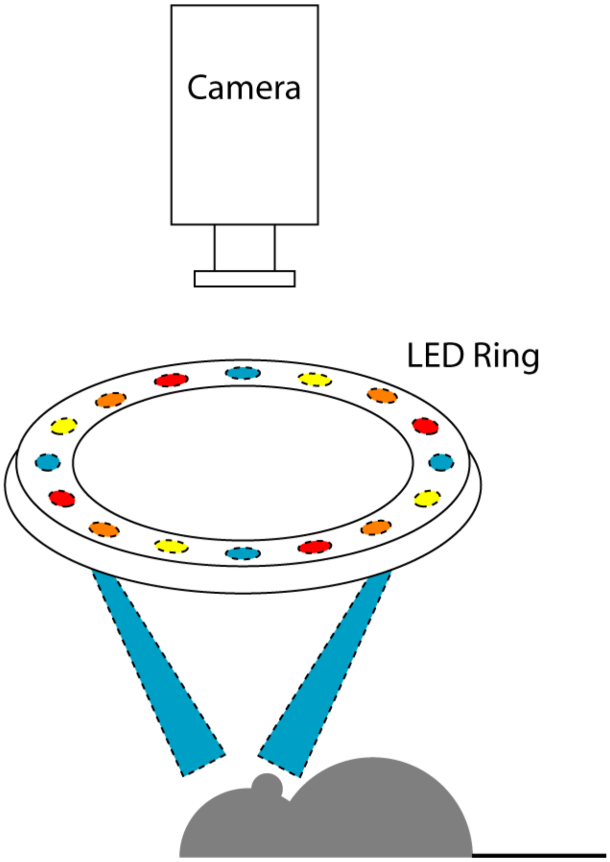

Figure A.1: System for functional connectivity optical intrinsic signal imaging. Illumination is from sequentially flashing LEDs in four different colors arranged in a ring for even light coverage. Detection is by an EMCCD camera at 120 Hz (30 Hz after decoding of wavelengths). Crossed linear polarizers prevent artifacts from specular reflection off the skull.

The mouse was placed at the focal plane of both the camera and the LED ring and held in place with a stereotactic holder. The field-of-view was adjusted to be approximately 8 mm square. This results in a field-of-view that covers the majority of the convexity of the cerebral cortex with anterior-posterior from the olfactory bulb to the superior colliculus (Fig. A.2a). Achieving the 120 Hz data rate was made possible by 4 × 4 pixel on-camera binning (reducing the output image from 512 × 512 pixels to 128 × 128 pixels) and spooling the data directly to disc (a 5 min scan at 120 Hz produces 1.2 GB of data).

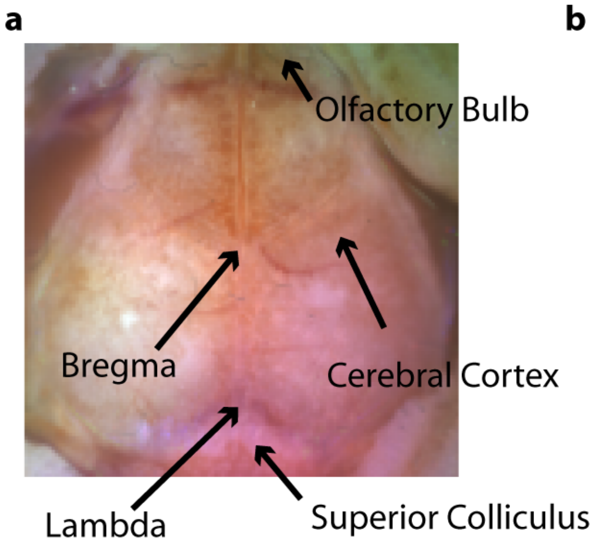

Figure A.2: The mouse cortex viewed with OIS. (a) A false color image of the mouse cortex. The first images from the red (625 nm), yellow (588 nm), and blue (478 nm) LED channels have been normalized to a maximum value of one and then stored in the red, green, and blue channels of the image, resulting in a false "white light" image of the camera's field-of-view. The cerebral cortex is visible through the skull from the olfactory bulb to the superior colliculus and far laterally on the convexity. In the corners, one can see the reflected skin flaps. (b) Using Photoshop, the image in (a) was manually segmented into brain (red) and not brain (blue). Functional connectivity processing was only performed on the brain region.

A.2.3 Image Processing

Images series were first converted to differential measurements as in Eq. 2.21. As OIS uses planar illumination, there are no discrete sources and DOT reconstructions are not performed. Instead, all image resolution comes from the camera lens, as in standard light microscopy. In order to correct for the different distances that each wavelength travels through tissue, every image was divided by a path length factor:

$$\Delta\Phi'_{\lambda_i} = \frac{\Delta\Phi_{\lambda_i}}{D_{\lambda_i}} \tag{A.1}$$

This path length factor was calculated using the analytical formula in Arridge et al. [1992] (Eq. 34 in that reference).

Data was then filtered to the functional connectivity band ($0.009 - 0.08$ Hz). I then converted absorption coefficient data to hemoglobin concentration changes using the same spectroscopy approaches detailed above (Eq. 2.54). Except now that I am using data at four wavelengths to find two hemoglobin species concentrations. Thus, the problem is over-determined, an **E** is inverted using a pseudo-inverse to find the least-squares solution. Each pixel's time series was resampled from 30 Hz to 1 Hz for further analysis. Images in each contrast were smoothed with a Gaussian filter (5×5 pixel box with a 1.3 pixel standard deviation).

To create a false color "white light" image of the mouse brain, the first images from the red (625 nm), yellow (588 nm), and blue (478 nm) LED channels were normalized to a maximum value of one and then stored in the red, green, and blue channels of an RGB image (Fig. A.2a). This image was viewed in Adobe Photoshop and all areas not corresponding to brain were manually painted white. The image was loaded back into MATLAB and was used to create a brain mask (Fig. A.2b). All further analysis was performed only on those pixels labeled as brain.

The time trace of every pixel defined as brain was averaged to create a global brain signal. This global signal was regressed form every pixel's time trace to remove global sources of variance.

A.2.4 Atlas Construction

An atlas of the locations of cortical locations in a superior projection of the convexity was constructed using a histological atlas [Franklin and Paxinos, 2008]. In every coronal slice, the lateral extent of every cortical area viewable from above was written down, and these coordinates were used to construct polygons for every cortical region. This procedure was repeated using the sagittal slices. From these two sets of polygons, a smoothed "consensus" atlas segmentation was produced (Fig. A.3).

In the atlas, I also noted the position of the junction between the olfactory bulb and cerebrum along the midline and the position of the fissure between the superior colliculus and the cerebrum along the midline (which is also the position of the lambda). These two points were also found in the "white light" mouse brain images. I could then easily find an affine transform from pixel space in the brain to positions in the atlas. I only allowed one stretch component; so the anterior-posterior stretch (determined by the above to landmarks) also was used for the medial-lateral stretch. Then, every pixel in the mouse brain could be assigned to segmented cortical polygons from the atlas (Fig. A.4). Note, gaps were purposely left in the atlas segmentation between regions, so that brain regions would be smooth. So, not every pixel in the OIS image is assigned a putative cortical region. Also, this assignment procedure was only performed for pixels previously defined as brain.

A.2.5 Functional Connectivity

Seed-Based Analysis

Using the atlas as a reference, seed locations were chosen at coordinates expected to correspond to the left and right visual, motor, somatosensory, frontal, cingulate, and retrosplenial cortices as well as the right and left superior colliculi and olfactory

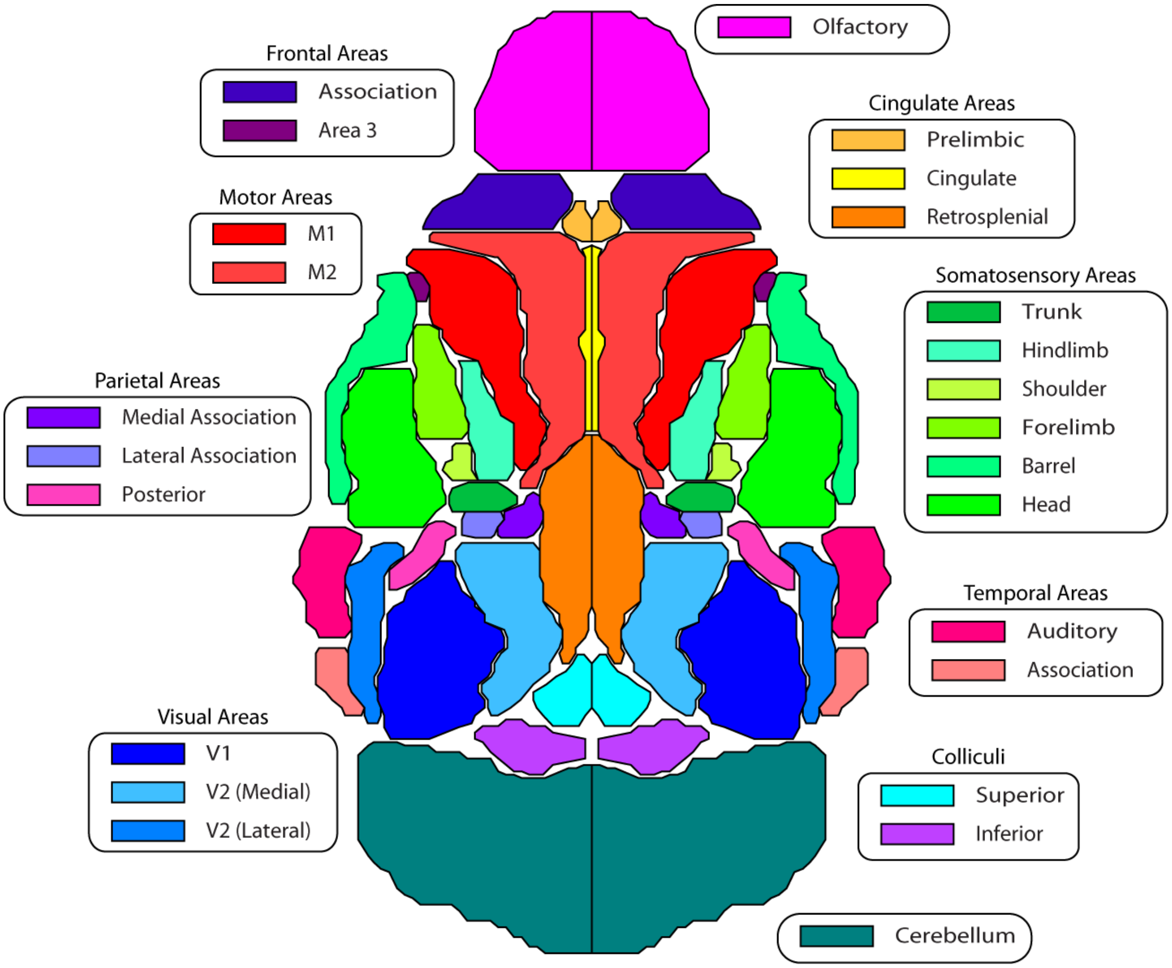

Figure A.3: Superior projection of the cortical convexity of the Paxinos atlas. Both the coronal and sagittal atlases were segmented to create polygons for each functional region. These two atlases were combined and smoothed to create this "consensus" atlas, which is a superior view of the mouse brain (anterior on top). Regions are color-coded and grouped by functional identity.

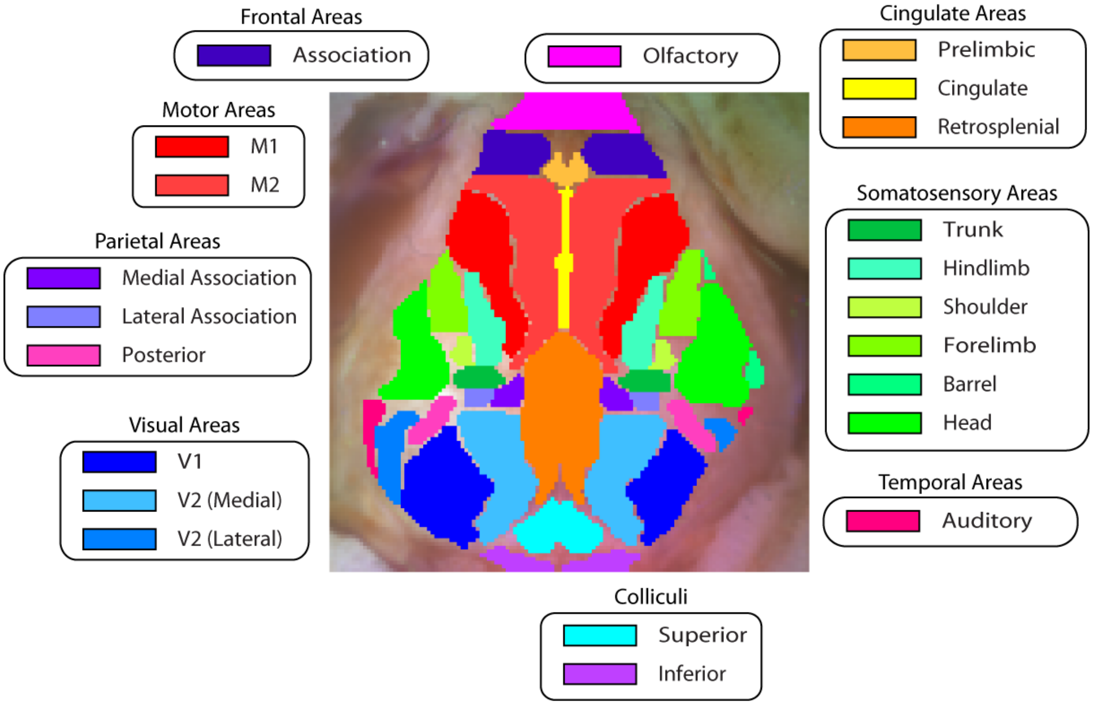

Figure A.4: Paxinos segmentation applied to an OIS “white light” frame. The atlas segmentation was applied to the image (Fig. A.2a) by using the landmark fissures at the midline. Regions that were previously labeled brain (Fig. A.2b) were assigned a cortical region if they fell within an affine-transformed atlas polygon. Note that since the skin retraction was not perfectly symmetrical, the lateral borders assigned are not symmetric.

bulbs. A 0.5 mm diameter circle are each seed location was averaged to create a seed time trace. These seed traces were correlated against every other brain pixel to create functional connectivity maps.

Singular Value Decomposition

Since seed-based methods are dependent on the seed location, I also used seed-independent methods for determining connectivity patterns. The time traces in every pixel were correlated against every other pixel to create an $N \times N$ connectivity matrix (where N is the number of pixels defined as brain). This matrix contains all the functional connectivity information that could be gained from seed-based analysis, but has too much data to examine all at once. Taking the SVD of this matrix will yield modes that most explain the patterns in the correlation maps. These spatial modes thus demonstrate the most important connectivity patterns.

Iterative Methods

In order to demonstrate the power of fcOIS, I decided to attempt to use the resting-state brain signal to divide the brain into functional regions, hopefully regenerating the atlas divisions in a data-driven way. While, I could simply correlate every pixel against every seed we defined above and assign each pixel to the functional region with which it has the highest correlation value, this procedure is limited in its power. It can be refined with an iterative method consisting of three steps: (1) seed time traces are made, (2) every seed is correlated with every pixel to create a connectivity matrix, and (3) every pixel is assigned to the seed time trace with which it correlated most highly. Then, the time traces from every pixel in the regions in step (3) can be averaged to create new seed time traces, repeating step (1). This cycle is iterated until no pixel changes regions in a loop.

This iterative method will work for any initial seed definitions. I considered three such seedings. First, I used the seeds defined above for the seed-based maps that were chosen from expected anatomy. Second, I took the ten singular modes of the connectivity matrix that had the highest singular values. These maps have areas of both positive and negative "correlations", so every map was inverted to create twenty spatial mode maps. Every pixel was then assigned to whichever map it had the highest coefficient with. Third, the 128×128 pixel map was divided into 20×20 pixel squares. Areas outside of the brain were then eliminated from these regions. These squares were then used as initial seed regions. These latter two methods are thus completely data-driven.

Once I had stable parcellations, I wanted to know the networks that these regions corresponded to (especially as for the data-driven methods the numerical labels assigned to each region are completely arbitrary). Thus, I correlated every seed region against every other seed region to create a seed-to-seed correlation matrix. Clustering was then performed using MATLAB's `linkage` function with the distance between any two regions defined as $1 - r$ (where r is the correlation coefficient). These clusters were then used to define functional connectivity networks and assign putative functional borders.

A.3 Results

A.3.1 Functional Connectivity in the Mouse Brain

The examination of correlation maps in optical intrinsic images show bilateral functional connectivity patterns (Fig. A.5). All seed locations show correlations with adjacent cortex as well as homotopic contralateral cortex. Since the seeds were chosen manually, they are not always exactly in corresponding contralateral locations. Thus, the "right" and "left" maps aren't always exactly symmetric. For example, the motor seeds seem to indicate that there are medial and lateral portions to the network.

Additionally, we see some larger-scale structure. There are very strong correlations between olfactory, frontal, and cingulate cortices. The cingulate cortex also shows correlations with putative medial motor areas. In between the visual and somatosensory seeds, there are regions that show correlations with both seeds. The retrosplenial cortex also shows very strong bilateral correlations and a very sharp delineation from adjacent cortical areas. We also see anticorrelations. The frontal/cingulate network shows strong anticorrelations with the somatosensory network. And, the retrosplenial is anticorrelated with the motor seeds.

Similar patterns are seen with the singular value decomposition of the full correlation matrix. The first singular component shows the very strong frontal/cingulate network and its anticorrelation with bilateral sensory areas (Fig. A.6a). The second component shows putative lateral motor areas as well as sensory areas and their anticorrelations with the bilateral retrosplenial cortex (Fig. A.6b). Further components show visual areas and the superior colliculus (Fig. A.6c) and more medial motor areas (Fig. A.6d).

A.3.2 Parcellation

The automated parcellation schemes recreate the earlier patterns that we saw, while eliminating the details that come from the exact seed position. First, I performed iterative parcellation using the seed locations chosen above. The resulting parcels (Fig. A.7a) divide up the cerebral convexity into functional areas that look similar

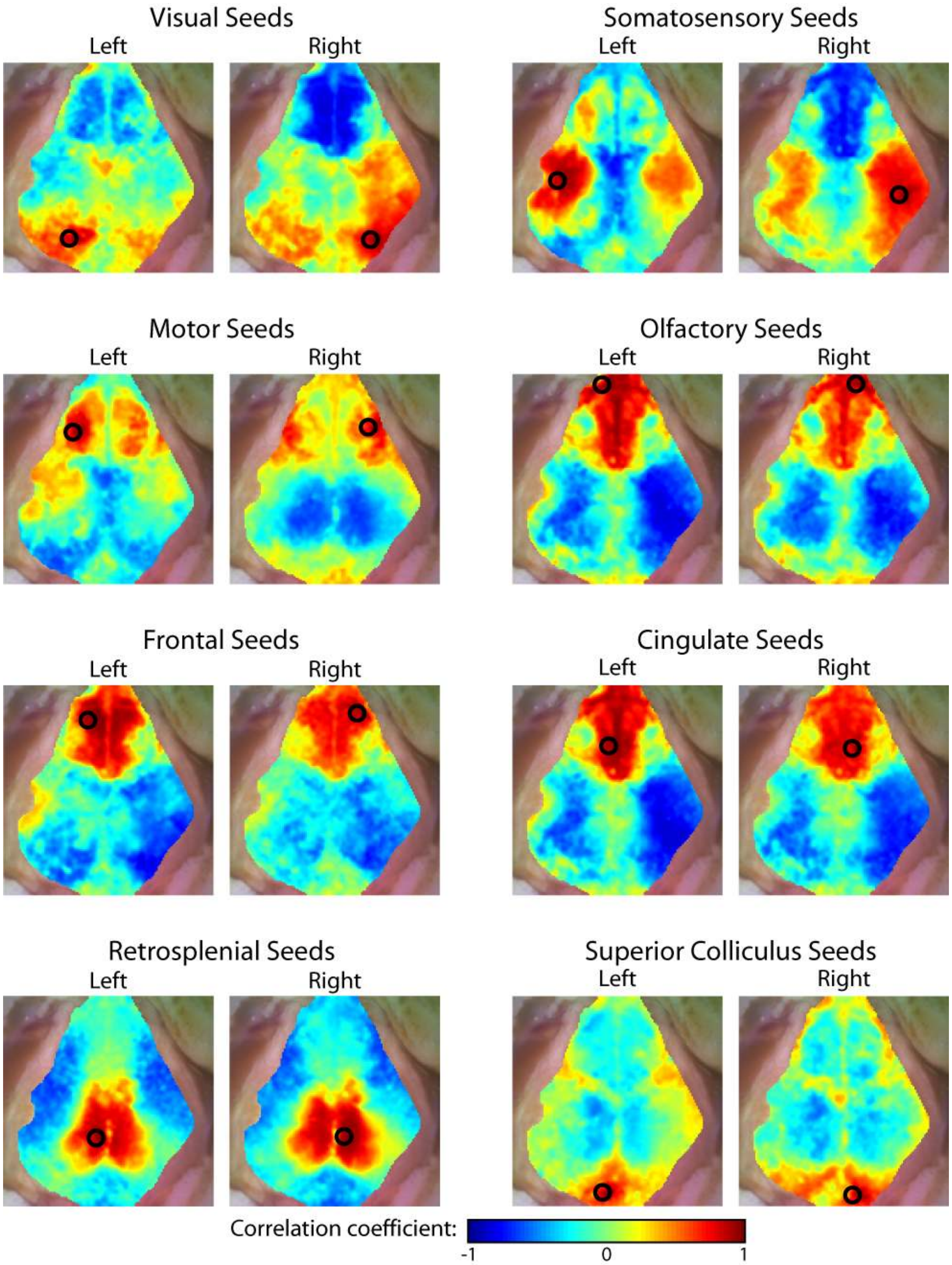

Visual Seeds

Somatosensory Seeds

Motor Seeds

Olfactory Seeds

Frontal Seeds

Cingulate Seeds

Retrosplenial Seeds

Superior Colliculus Seeds

Figure A.5: Seed-based functional connectivity with OIS. Correlation maps for seeds chosen manually using the expected cortical positions of various functional areas. Seed positions and sizes are shown with black circles. All correlation maps are scaled from $r = -1$ to 1. Note the bilateral patterns. Maps are shown overlaid on the "white light" image of the field-of-view.

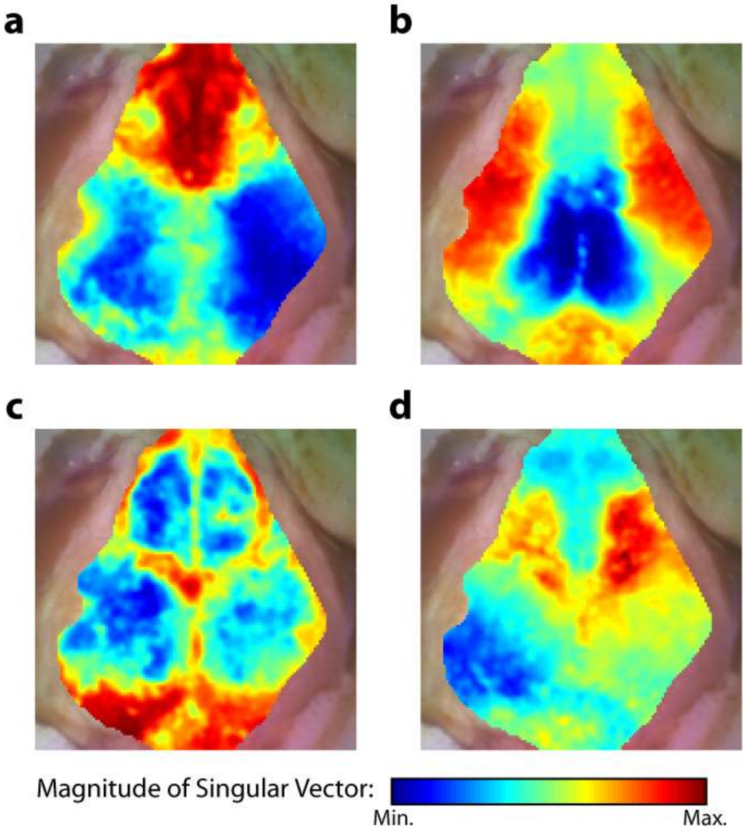

Figure A.6: Singular modes of the mouse connectivity matrix (the four singular vectors with the highest singular values). (a) This component shows the strong correlations with the frontal, olfactory, and cingulate cortices and the anticorrelations with bilateral sensory areas. (b) A component with lateral motor and somatosensory areas anticorrelated with retrosplenial cortex. (c) Component showing correlations with visual cortex and the superior colliculus. This component also shows some correlations with the veinous system along the sutures. (d) Bilateral correlation within putative medial motor cortex.

to those from the atlas segmentation (Fig. A.7b). Clustering of these parcels based on their seed-to-seed correlations gives us similar functional networks to what we expected from our seed-based correlation maps and SVD analysis (Fig. A.7c, parcels are named based on their anatomical location, their putative homologue in the atlas, and their connectivity). These networks are then easily seen in the correlation matrix (Fig. A.8). There is a frontal/cingulate/olfactory network, which correlates highly with what (based on their anatomic area) are presumably medial motor areas. These medial motor areas, in turn, correlate with each other and with more lateral motor areas. There is also a visual network (with the superior colliculus), a somatosensory network, and a retrosplenial network. The right visual seed correlated so highly with adjacent somatosensory areas, that it's parcel now takes up a very large region encompassing somatosensory areas on both sides of the brain. Thus, with this initial distribution of seeds, we were not able to do a very good job of parcellating the occipital part of the cortex.

Iterative parcellation using the SVD components yields a similar result. However, as the initial condition had a more even distribution of starting parcels that were more equally distributed throughout the volume, the resulting final parcels are able to do a better job of finding the boundaries between different functional areas (Fig. A.9a,b), especially in the occipital cortex. We see the cortex divided into the same main networks. First, on the left of the dendrogram (Fig. A.9c), we see the retrosplenial network, distinct from everything else. Then, there is the frontal/olfactory/cingulate network that closely correlates with medial motor areas, which in turn correlate with lateral motor areas. While the motor areas more closely correspond to their contralateral homologue than adjacent areas, the somatosensory areas closely correspond to other ipsilateral somatosensory regions. Additionally, the right somatosensory regions closely correlate with right visual regions. Finally, we see a left visual and superior

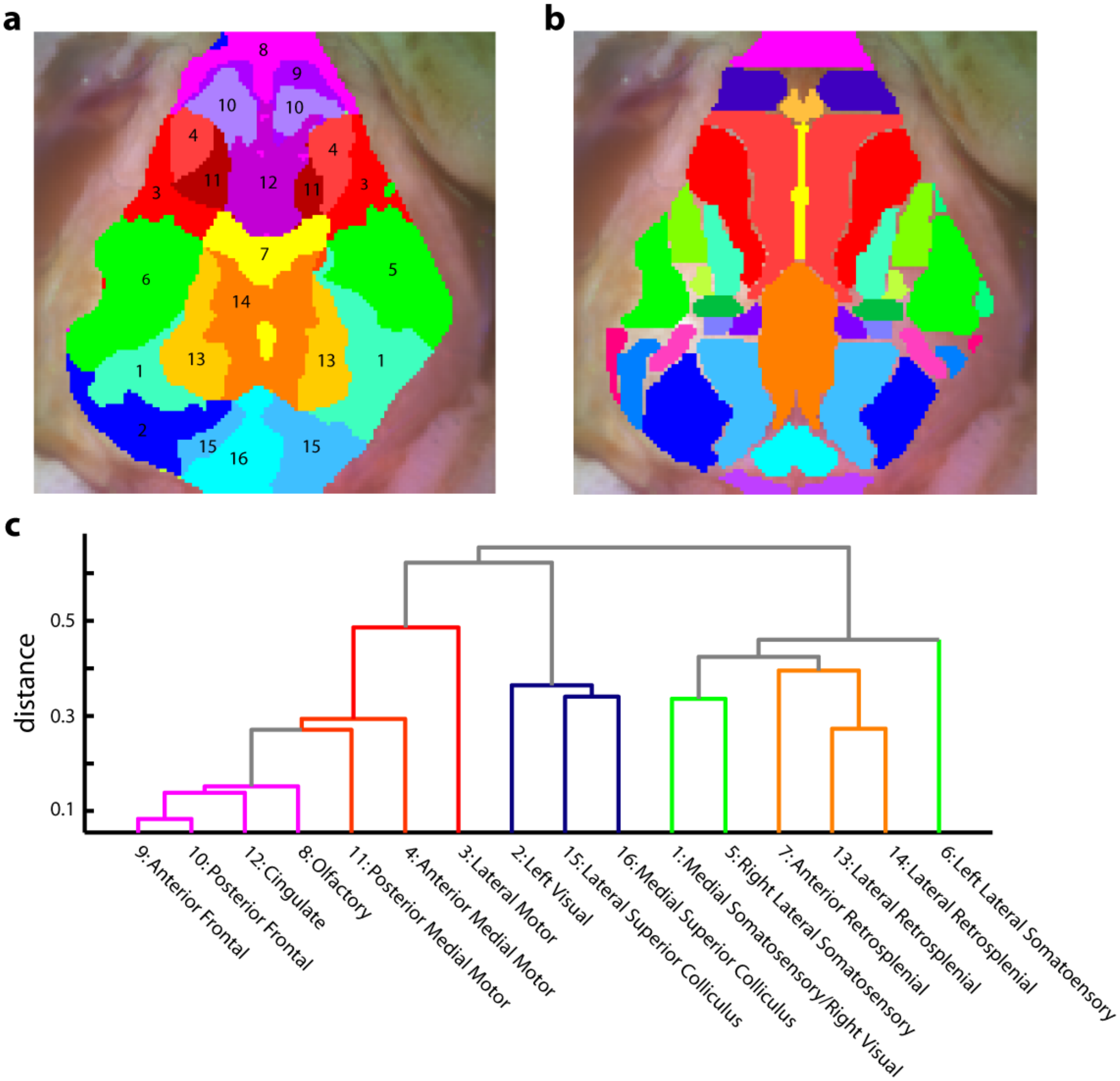

Figure A.7: Iterative parcellation with manual seeding. (a) The results of iterative parcellation using the manually chosen seeds as an initial condition. We see clear delineation of a frontal/olfactory/cingulate network, a motor network, and a somatosensory network. In the visual cortex, the left side and the colliculus are defined, but the right visual cortex gets pulled into the somatosensory network due to it's close correlations and the sparse initial seeding. (b) The Paxinos atlas applied to the mouse brain for comparison. (c) Clustering of the parcels from their parcel-to-parcel correlations. Branches are color-coded based on their functional assignments. Note the tight correlations in the frontal network connecting to first medial and the lateral motor areas, as well as, main branches for most of the main networks we expect.

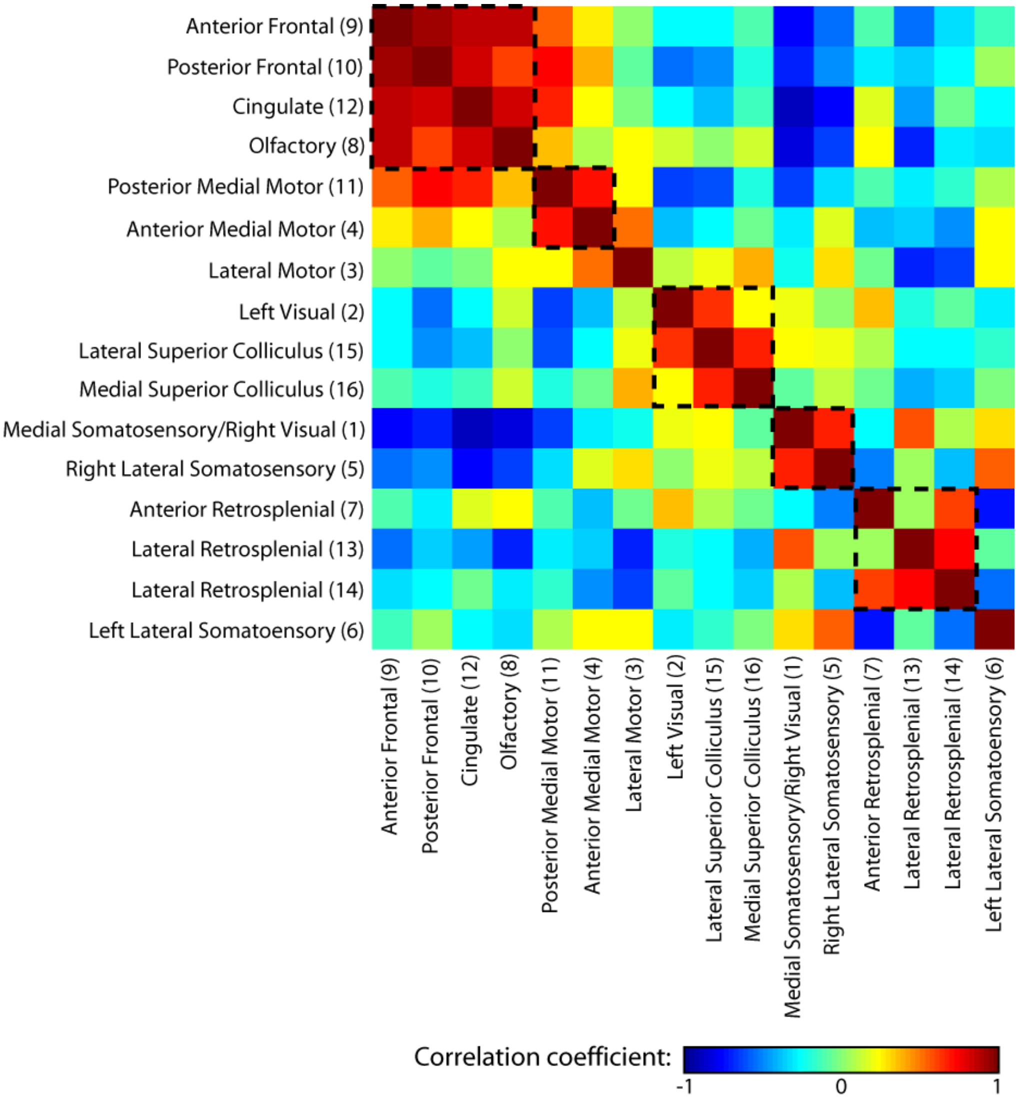

Figure A.8: Correlation matrix after iterative seed-based parcellation. We see a block-diagonal pattern showing how the clustering has arranged the parcels into networks (dashed boxes shown for added visualization). Note the anticorrelations between frontal and somatosensory and between retrosplenial and motor. The left somatosensory, although ordered on it's own, correlates most strongly with the right somatosensory cortex.

colliculus network, and a left parietal region in between somatosensory and visual.

These networks are clear in the correlation matrix (Fig. A.10) where we also see strong anticorrelations between retrosplenial and motor and between cingulate and somatosensory areas. We also see strong correlations between left and right somatosensory areas. Interestingly, the highest correlation for a somatosensory parcel is with its putative homologue. For example, the region labeled Right Anterior Somatosensory correlates most highly in the left brain with the region labeled Left Anterior Somatosensory. We also see that the parietal areas between visual and motor correlate highly with both.

As an additional data-driven parcellation, I started by tiling the mouse brain with 20 × 20 pixel boxes and letting this pattern iteratively evolve. This procedure resulted in 35 parcels, so the clustering results are harder to visualize. Additionally, sometimes when the parcels get too fine, they end up correlating with local noise sources, possibly vascular. However, the same patterns are still visible (Fig. A.12). The same networks are shown in the correlation matrix (Fig. A.12).

A.4 Discussion

I have shown the first results using optical intrinsic signal imaging to measure functional connectivity and also the first resting-state networks described in mice. Our fcOIS system has a frame rate high enough to exclude spurious physiology, a field-of-view over most of the mouse convexity, and signal-to-noise enabling us to image through the intact skull. In order to guide my initial seed placement, I made a superior view segmentation of the mouse brain using the Paxinos atlas [Franklin and Paxinos, 2008]. Using these coordinates as a guide, seeds were placed in the visual, somatosensory, motor, frontal, cingulate, and retrosplenial cortices as well as the olfactory bulb

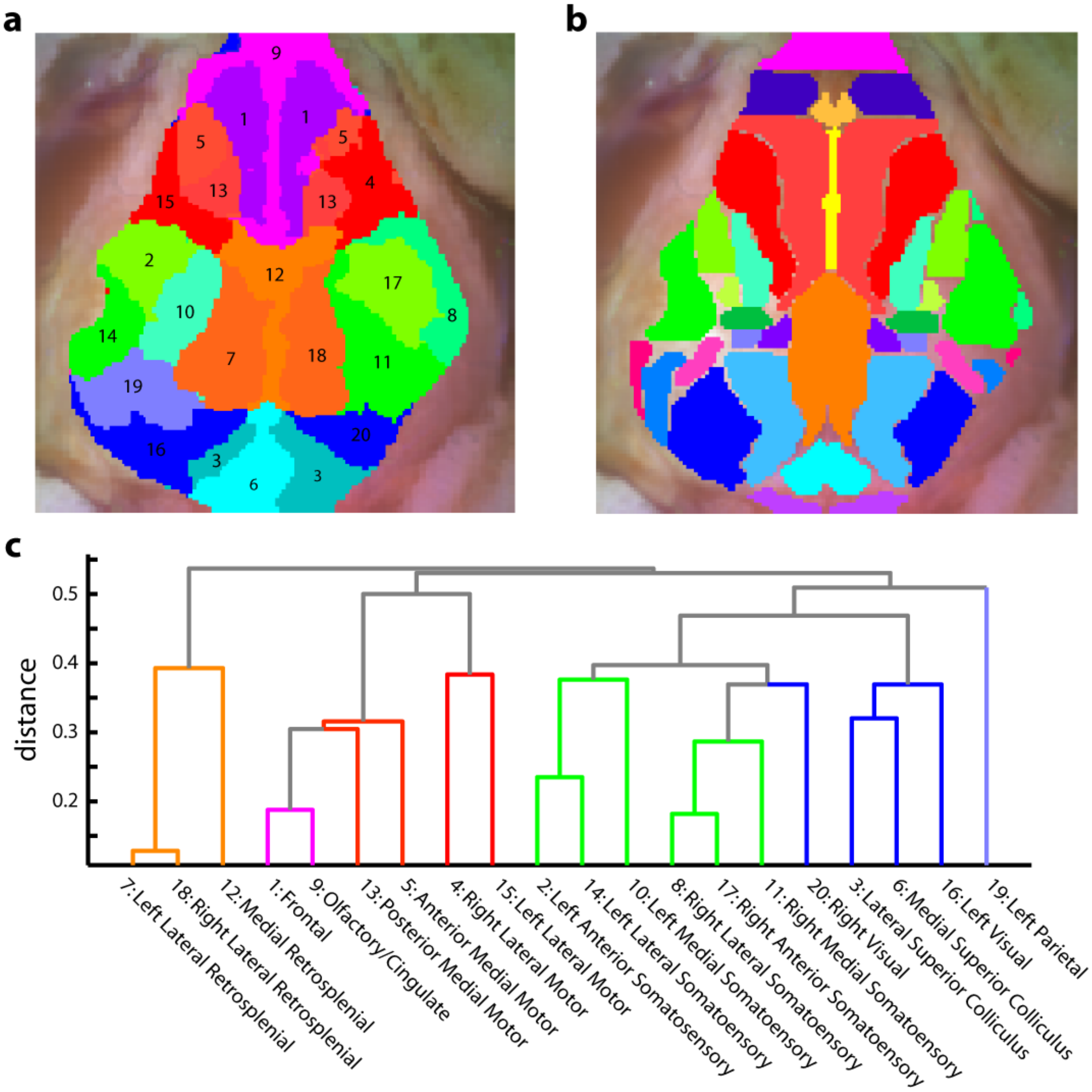

Figure A.9: Iterative parcellation with SVD seeding. (a) The results of iterative parcellation using the SVD components are initial seeds. We see the same networks as previously, although with better differentiation of visual and somatosensory cortex with the distinction of a putative left parietal area. (b) The Paxinos atlas applied to the mouse brain for comparison. (c) Clustering of the parcels from their parcel-to-parcel correlations. Branches are color-coded based on their functional assignments. Similar connections are noted as before, with better differentiation of somatosensory and visual cortices.

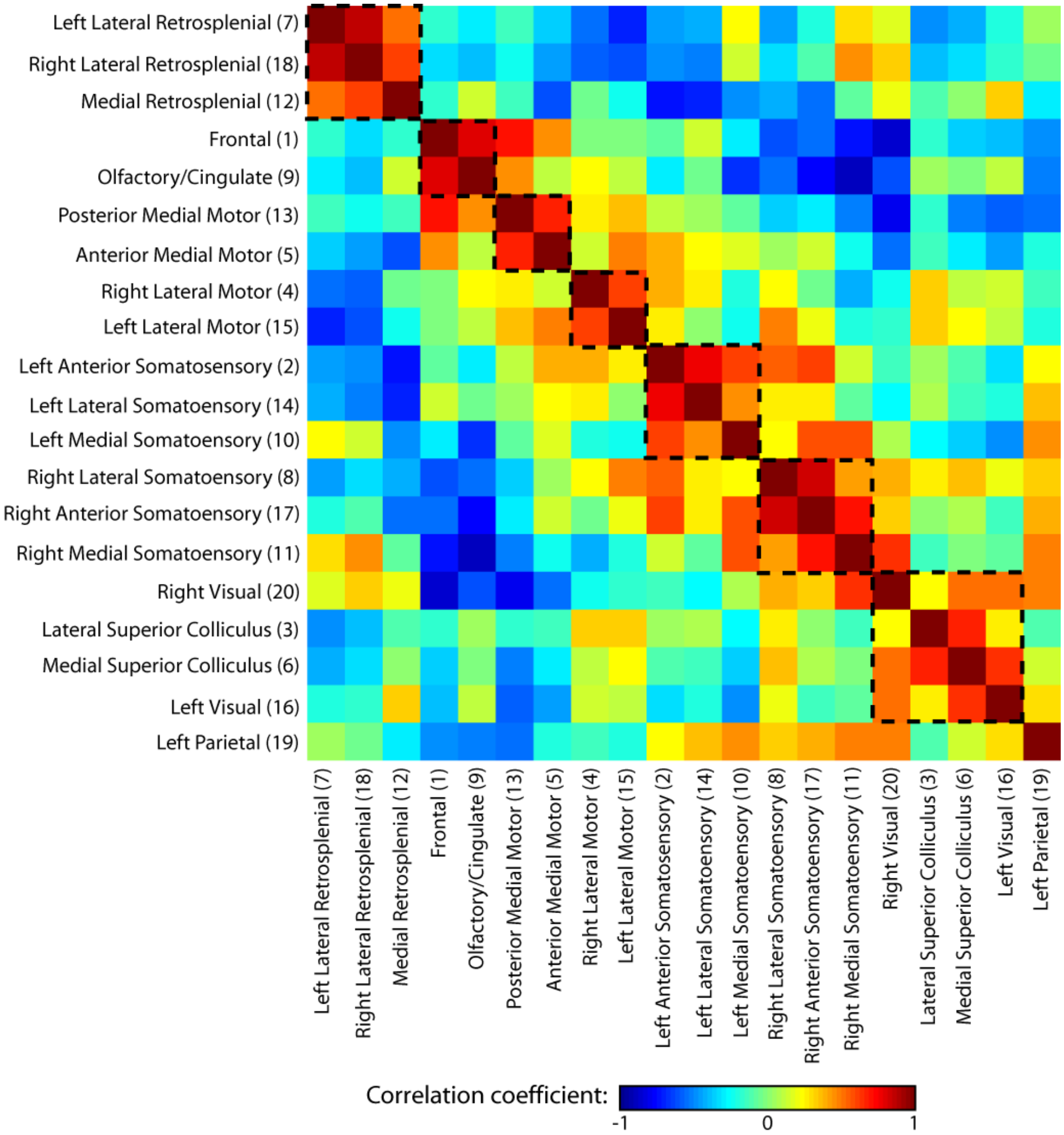

Figure A.10: Correlation matrix after iterative SVD parcellation. We see a block-diagonal pattern showing how the clustering has arranged the parcels into networks (dashed boxes shown for added visualization). Note the anticorrelations between frontal and somatosensory and between retrosplenial and motor. The left parietal region correlates with both visual and somatosensory regions. Also note how each somatosensory parcel correlates most highly with its similarly named homologue in the opposite hemisphere.

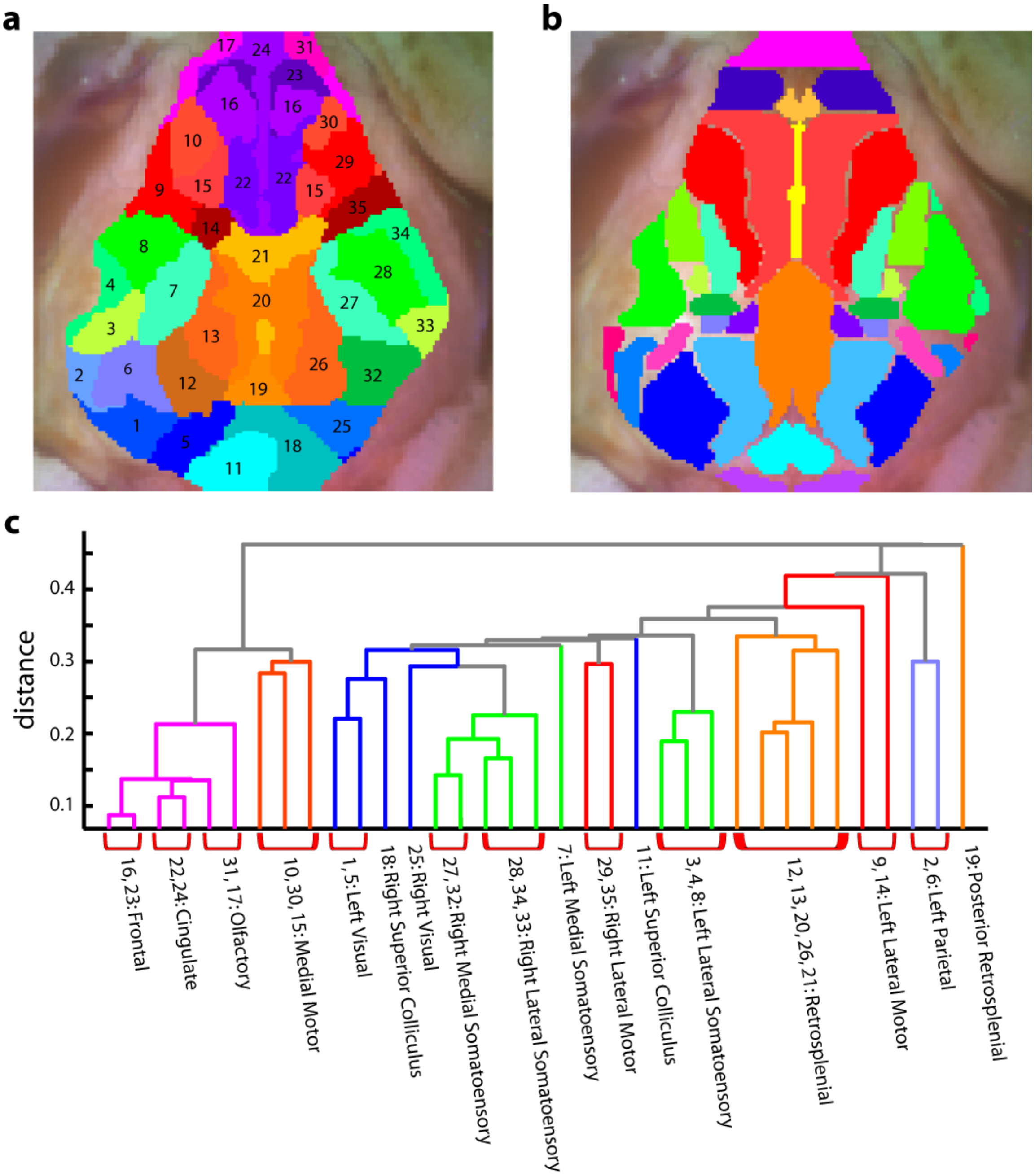

Figure A.11: Iterative parcellation with square tile seeding. (a) The results of iterative parcellation using 20 × 20 pixel boxes as initial seeds. Although, the parcels are smaller, we can add them together to see the same networks as previously. (b) The Paxinos atlas applied to the mouse brain for comparison. (c) Clustering of the parcels from their parcel-to-parcel correlations. Branches are color-coded based on their functional assignments. The same general clustering patterns are noted. Perhaps since smaller parcels lead to some seed time traces having significant local vascular noise, some regions do not cluster as well, but most functional regions remains tightly grouped.

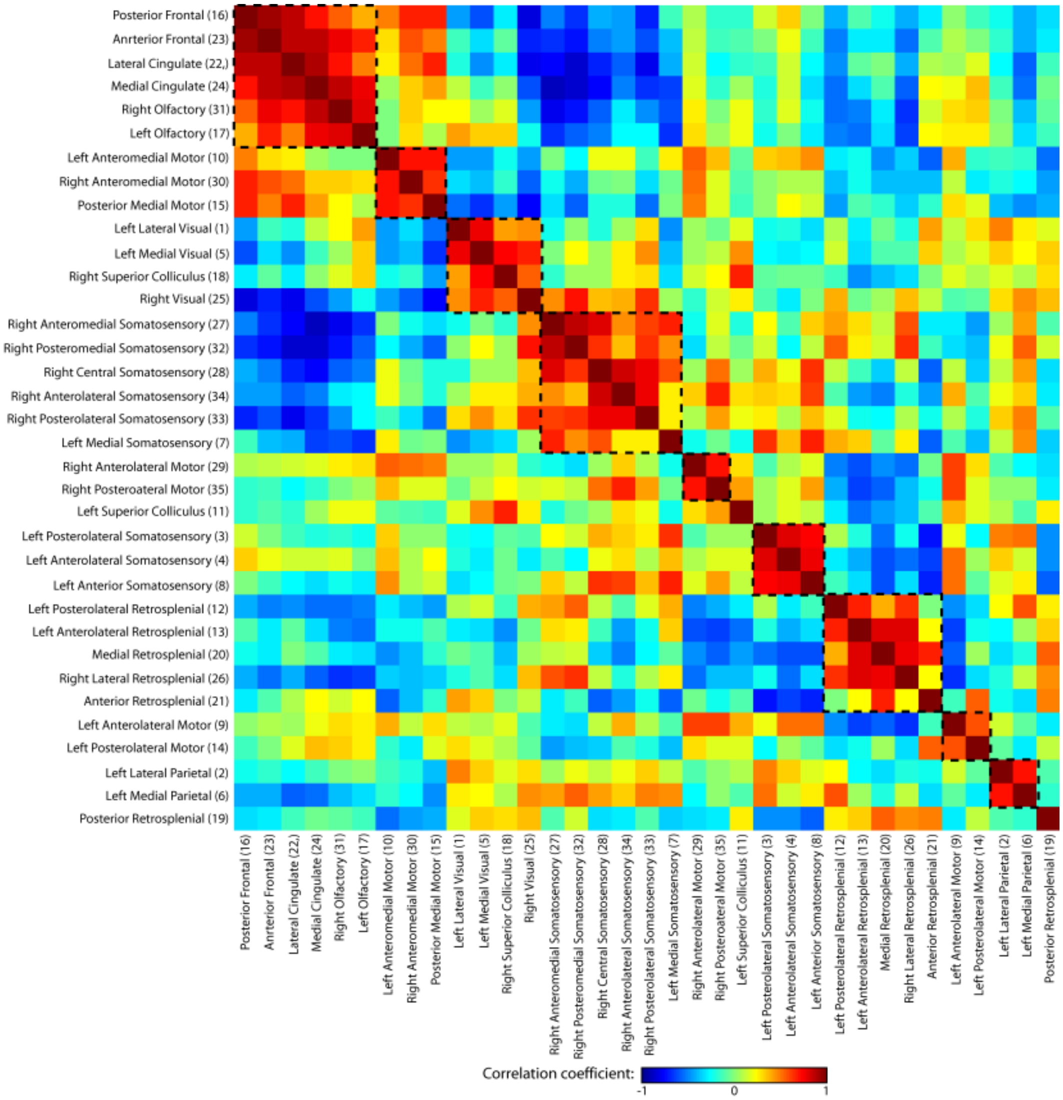

Figure A.12: Correlation matrix after iterative square parcellation. Again, we see a block-diagonal pattern showing how the clustering has arranged the parcels into networks (dashed boxes shown for added visualization), with the anticorrelations between frontal and somatosensory and between retrosplenial and motor.

and the superior colliculus (these being all of the major cortical areas within our field-of-view). Functional connectivity maps made with all of these seeds show bilateral correlation patterns delineating ipsilateral regions and homotopic functional regions. While we do not find large, disjoint anterior-posterior connectivity patterns as can be found in the human (most likely due to the fact that such large-scale, integrative functional processing is unlikely to occur in the mouse), we do see some adjacent regions form into networks. The frontal, olfactory, and cingulate seeds are all highly correlated with each other. And the visual cortices are correlated with the superior colliculus. Similar network patterns are found with the SVD analysis.

This division of the cortex into regions is made more explicit with the iterative parcellation routines followed by clustering. Seeding with different initial conditions (the manually chosen seeds, the SVD components, or square tilings) yields a different number of parcels, but these can be assembled into the same main functional regions (a comparison of the parcellations is shown in Fig. A.13). The first feature to notice is that the cingulate extends more laterally in the functional data than was expected by the atlas. This difference is most likely due to the way the atlas was constructed. On the surface, the cingulate has very little area visible from the superior view. However, due the brain's curvature, the cingulate cell bodies lie beneath the surface layers of M2. If one accounts for the photons' penetration depth, the cingulate segmentation in the atlas should have been wider, which will be corrected in a future version of our atlasing. Another difference that we see is that the visual areas do not extend as far anteriorly in the functional data as the atlas would suggest. However, the general pattern is very similar to the atlas and reproducible across methods.

It is interesting to note that when the parcellation results in multiple somatosensory areas (as in the SVD parcellation), these areas correlate highly with their putative homologue in the other cortex. For example medial left somatosensory cortex corre-

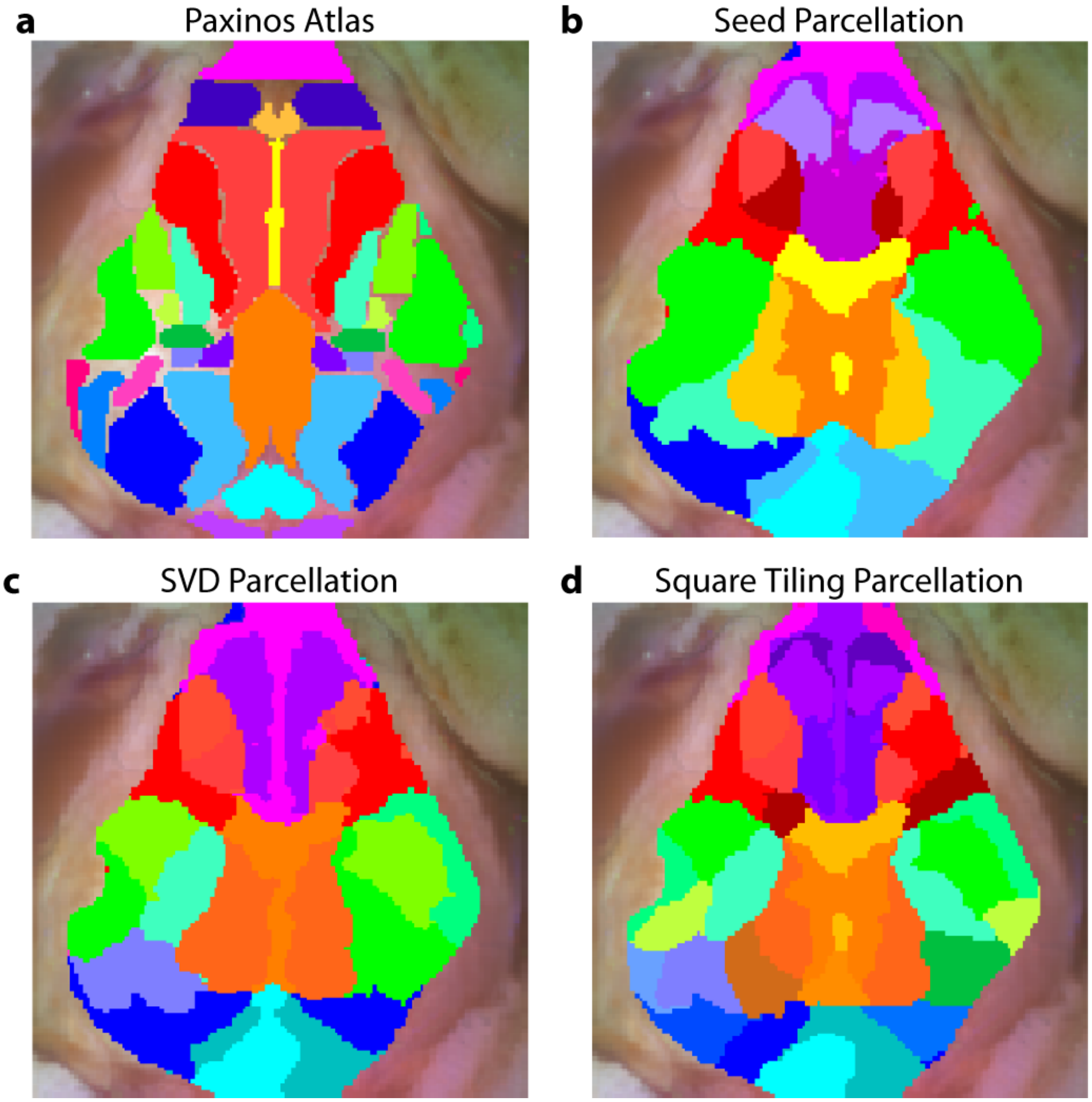

Figure A.13: Comparison of different parcellations with the Paxinos atlas. (a) Segmentation from the superior view of the Paxinos atlas for comparison. (b-d) Parcellations from various methods (Fig. A.7a, Fig. A.9a, and Fig. A.11a) shown together to enable side-by-side comparison. Note that despite the differential initiation conditions, the iterative parcellation scheme always converges to a very similar functional division of the cortex.

lates most highly in the other hemisphere with medial right somatosensory cortex. Thus, while here we have grouped parcels into large functional networks, it might be possible to use fcOIS to subparcellate cortical regions after regression of shared variance. A “murunculus” that could be found through stimulation studies might be able to be reproduced solely with resting-state data. We have not yet performed activation studies, but we expect to do so in the near future.

These parcellations reproduce what we might expect from mouse systems neuroscience. The functional connectivity network of olfactory, frontal, and cingulate cortices is most likely a limbic network controlling approach and threat avoidance. This role could explain it’s close connections with motor planning regions in the medial motor cortex. In contrast, these frontal regions show clear distinction from the functional connectivity maps of the retrosplenial cortex along the posterior midline. This region is most likely the mouse equivalent of the default network, as is the center of the default network in humans. Although the mouse seemingly lacks the default-mode components in anterior cingulate and lateral parietal, this smaller default network is not unexpected, as these other connections are hypothesized to be later evolutionary additions. As in humans, this default mode network shows strong anti-correlations with motor cortex regions. In between somatosensory cortex and visual cortex are a number of regions that are only difficultly parceled[a], which most likely are parietal regions involved in sensory integration between somatosensory and visual stimuli. These parietal regions are much smaller in the mouse than in the human (as expected), although we see a larger region given to them in the parcellation than might be expected from the atlas.

---

[a] The seed-based parcellation does the poorest job due to the poor sampling allowed by the small number of seeds. The SVD and tiling parcellations create a separate network on the left closely coupled to both somatosensory and visual, while on the right these regions are clustered with somatosensory although they are also highly correlated with the right visual cortex.

Also, note that near the midline, the parcels mostly are divided along anterior-posterior axes. For example, we always see medial and lateral retrosplenial as well as medial and lateral cingulate/frontal components. However, as we move more lateral in the mouse cortex the division run more medial-lateral resulting in stripes of functional areas (M2, M1, somatosensory, parietal, and visual as we move anterior to posterior). These orientations seem to mirror the manner in which the cortex devlops and evolves, first extending outwards from the allocortex with the neocortex filling in between later. This result provides further validation of the neuronal content of our signals.

These results, in total, show the success of functional connectivity mapping with OIS. The parcellation is both an interesting neuroscience result and a demonstration of the method's power. This ability to map the mouse cortex is complemented by the method's ease of use. All of the results here were obtained without any thinning of the skull, and the anesthetic was a simple intraperitoneal injection. The system hardware was inexpensive and relatively easy to assemble and use. Thus, fcOIS could be duplicated by many laboratories pursuing neuroscience research with mouse models, thereby decoupling neuroimaging from bulky and expensive MRI scanners. We expect that fcOIS could be a useful tool to connect the intriguing neuroimaging results of human disease obtained through fcMRI with advances in mouse models (both with genetic modifications and with surgical interventions not possible in people). The ability to perform longitudinal scanning at low cost could allow insight into the progression of diseases such as Alzheimer's.

Appendix B

Captions for Videos

- **Video 3.1**: Point-spread functions of targets placed at every location in the field-of-view for the sparse and high-density grids. (upper left) Simulated targets ($2\times2\times10$ mm) to be measured and reconstructed by the different arrays. (lower left) The response reconstructed with the high-density array. Note that the response tracks the movement of the target and that there is minimal blurring. (upper right) The response reconstructed with the square sparse array. The response jumps to the high sensitivity underneath the nearest source-detector pair, causing mislocalization and large response sizes. (lower right) The response reconstructed with the triangular sparse array. While the array can localize the target well horizontally, it has only two major positions vertically.
- **Video 4.1**: Example of activations due to a counter-clockwise rotating wedge stimulus, shown at 10× actual speed. (left frame) The counter-clockwise rotating wedge checkerboard stimulus. For simplicity, the couter-phase flickering is not shown. (right frame) Activations in subject 1 (session 1) due to this stimulus. In order to match the stimulus and response for this figure, we have user our measured 6 s lag between stimulation and maximal response. Note

that the hemodynamic response is always in the maximal in the opposite visual quadrant from the stimulus.

- **Video 4.2**: Example of activations due to the expanding ring stimulus, shown at 10× actual speed. (left frame) The expanding ring checkerboard stimulus. For simplicity, the flickering is not shown. (right frame) Activations in subject 4 (session 1) due to this stimulus. In order to match the stimulus and response for this figure, we have used our measured 6 s lag between stimulation and maximal response. Note that the hemodynamic response moves bilaterally upward in the visual field as the stimulus moves outward.

- **Video 4.3**: *In vivo* comparison of a phase-encoded mapping study of visual angle with NIRS and DOT. (left) The stimulus is a counterclockwise rotating, counter-phase flickering wedge. In order to line up stimuli and activations, we used our measured 6 s neurovascular lag. Here, the stimulus is shown without flicker and at 10× actual presentation speed. (upper right) Activations from these stimuli reconstructed with the triangular sparse array. Note the poor localization (especially in the lower half of the field-of-view) and strange activation shapes. (lower right) Reconstructions using the high-density array. Activations are correctly placed with reasonable sizes. The videos have been thresholded such that changes in hemoglobin concentration below baseline are not shown.

- **Video 4.4**: *In vivo* comparison of a phase-encoded mapping study of visual eccentricity with NIRS and DOT. (left) The stimulus is an expanding counter-phase flickering ring. In order to line up stimuli and activations, we used our measured 6 s neurovascular lag. Here, the stimulus is shown without flicker and at 10× actual presentation speed. (upper right) Activations from these stimuli reconstructed with the triangular sparse array. Note the poor localization, especially when the activation passes beneath the source line, and the inability to always locate activations in both hemispheres. (lower right) Reconstructions using the high-density array. Activations are correctly placed with reasonable sizes. The movies have been thresholded such that changes in hemoglobin concentration below baseline are not shown.

- **Video 4.5**: Simulations of activations similar to those from phase-encoded mapping of visual angle. The stimulus is of 1 cm radius and moves in an elliptical pattern, with the center of the ellipse displaced from the center of the field-of-view. There are a total of 36 activations in the entire rotation series. (upper left) The video of 36 targets. (lower left) Reconstructions using the high-density array. Activations are correctly placed with the correct size. (upper right) Activations reconstructed with the square sparse array. The activations are displaced to the nearest measurement location. (lower right) Reconstructions using the triangular sparse array. The activations are located correctly horizontally but jump from above the source line to below it.

- **Video 4.6**: Simulations of activations similar to those from phase-encoded mapping of eccentricity. The stimulus is two 1.4 cm-tall rectangles moving upward in the field-of-view. There are a total of 18 activations in the entire rotation series. (upper left) The video of 18 targets. (lower left) Reconstructions using the high-density array. Activations are correctly placed with the correct size. (upper right) Activations reconstructed with the square sparse array. The activations are displaced to the nearest measurement location, often resulting in squeezing in the horizontal direction. (lower right) Reconstructions using the triangular sparse array. Activations under the source planes are unconstrained vertically due to the pads symmetry.

Appendix C

The NeuroDOT MATLAB Toolbox

All of the programs written by me to perform the DOT analysis described in this paper have released as an open-source MATLAB toolbox under the Apache License. While designed to interact easily with the data acquisition software designed in-house for our DOT systems, the programs can easily be translated to data from other systems. In order to make such adaptation simpler, the programs are designed to be as modular as possible and to exist in multiple layers. At the highest level are easy-to-use programs to perform all of the analysis for a given experimental paradigm (e.g., retinotopy or functional connectivity). Thus, someone interested in performing neuroscience research doesn't have to worry much about the inner workings of the data processing. A second level of programs to perform pieces of the analysis (e.g., filtering and imaging) allow customization of processing for new experimental paradigms without worrying about algorithmic complexities. And, finally, the low-level programs are available to construct entirely image processing streams. Data visualization programs are also included, both to reproduce the figures shown in this paper and to check data integrity at various steps in the processing stream (e.g., raw data, filtered source-detector data, and imaged data).

Additional programs are included so that users can interface with our in-house DOT systems. It is now relatively straight-forward to change the optode arrangement or encoding scheme. Stimulus presentation has been standardized using PsychToolbox to allow easy control of many stimulus types through MATLAB, with more direct control of the stimulus than is possible with PsyScope. These stimulus programs are also designed to work with the fMRI stimulus computers, and any lab wishing to use them for that purpose should feel free to contact Prof. Culver or myself.

All of the programs are designed to have user-interfaces similar to those from built-in MATLAB functions, so that researchers familiar with MATLAB will not have to learn an entirely new syntax. Copies of the programs are available on request from the Culver Lab. An in-depth instruction manual for using the code is available on the internet at `roan4.wustl.edu/oicwiki` or by typing `help functionname` in the MATLAB command window.

Bibliography

M.C. Allen. Neurodevelopmental outcomes of preterm infants. *Curr Opin Neurol*, 21:123–128, 2008.

A.W. Anderson, R. Marois, E.R. Colson, B.S. Peterson, C.C. Duncan, R.A. Ehrenkranz, K.C. Schneider, J.C. Gore, and L.R. Ment. Neonatal auditory activation detected by functional magnetic resonance imaging. *Magn Reson Imaging*, 19(1):1–5, 2001.

S.R. Arridge. Optical tomography in medical imaging. *Inverse Probl*, 15(2):R41–R93, 1999.

S.R. Arridge, M. Cope, and D.T. Delpy. The theoretical basis for the determination of optical pathlengths in tissue: temporal and frequency analysis. *Phys Med Biol*, 37(7):1531–60, 1992.

J.W. Belliveau, D.N. Kennedy, R.C. McKinstry, B.R. Buchbinder, R.M. Weisskoff, M.S. Cohen, J.M. Vevea, T.J. Brady, and B.R. Rosen. Functional mapping of the human visual cortex by magnetic resonance imaging. *Science*, 254:716–719, 1991.

D.A. Benaron, S.R. Hintz, A. Villringer, D. Boas, A. Kleinschmidt, J. Frahm, C. Hirth, H. Obrig, J.C. van Houten, E.L. Kermit, W.F. Cheong, and D.K. Stevenson. Noninvasive functional imaging of human brain using light. *J Cereb Blood Flow Metab*, 20(3):469–477, 2000.

R.M. Birn, K. Murphy, and P.A. Bandettini. The effect of respiration variations on independent component analysis results of resting state functional connectivity. *Hum Brain Mapp*, 29:740–750, 2008.

B. Biswal, F.Z. Yetkin, V.M. Haughton, and J.S. Hyde. Functional connectivity in the motor cortex of resting human brain using echo-planar mri. *Magn Reson Med*, 34:537–541, 1995.

A.Y. Bluestone, G. Abdoulaev, C.H. Schmitz, R.L. Barbour, and A.H. Hielscher. Three-dimensional optical tomography of hemodynamics in the human head. *Opt Exp*, 9(6):272–286, 2001.

D.A. Boas, K. Chen, D. Grebert, and M.A. Franceschini. Improving the diffuse optical imaging spatial resolution of the cerebral hemodynamic response to brain activation in humans. *Opt Lett*, 29:1506–1508, 2004.

S. Boden, H. Obrig, C. Kohncke, H. Benav, S.P. Koch, and J. Steinbrink. The oxygenation response to functional stimulation: Is there a physiological meaning to the lag between parameters? *Neuroimage*, 36(1):100–107, 2007.

M. Boly, L. Tshibanda, A. Vanhaudenhuyse, Q. Noirhomme, C. Schnakers, D. Ledoux, P. Boveroux, C. Garweg, B. Lambermont, C. Phillips, A. Luxen, G. Moonen, C. Bassetti, P. Maquet, and S. Laureys. Functional connectivity in the default network during resting state is preserved in a vegetative but not in a brain dead patient. *Hum Brain Mapp*, 30(8):2393–2400, 2009.

T. Bonhoeffer and A. Grinvald. Iso-orientation domains in cat visual cortex are arranged in pinwheel-like patterns. *Nature*, 353:429–431, 1991.

P. Born, E. Rostrup, H.B.W. Larsson, H. Leth, M. Miranda, B. Peitersen, and H.C. Lou. Infant visual cortex function evaluated by fMRI. *Perception*, 26(6):758–759, 1997.

M.B. Bouchard, B.R. Chen, S.A. Burgess, and E.M.C. Hillman. Ultra-fast multispectral optical imaging of cortical oxygenation, blood flow, and intracellular calcium dynamics. *Opt Exp*, 17(18):15670–15678, 2009.

R.L. Buckner, J. Sepulcre, T. Talukdar, F.M. Krienen, H. Liu, T. Hedden, J.R. Andrews-Hanna, R.A. Sperling, and K.A. Johnson. Cortical hubs revealed by intrinsic functional connectivity: Mapping, assessment of stability, and relation to Alzheimer's disease. *J Neurosci*, 29(6):1860–1873, 2009.

V.D. Calhoun, P.K. Maciejewski, G.D. Pearlson, and K.A. Kiehl. Temporal lobe and "default" hemodynamic brain modes discriminate between schizophrenia and bipolar disorder. *Hum Brain Mapp*, 29:1265–1275, 2008.

J.A. Church, D.A. Fair, N.U.F. Dosenbach, A.L. Cohen, F.M. Miezin, S.E. Petersen, and B.L. Schlaggar. Control networks in paediatric Tourette syndrome show immature and anomalous patterns of functional connectivity. *Brain*, 132:225–238, 2009.

W. Colier, V. Quaresima, R. Wenzel, M. C. van der Sluijs, B. Oeseburg, M. Ferrari, and A. Villringer. Simultaneous near-infrared spectroscopy monitoring of left and right occipital areas reveals contra-lateral hemodynamic changes upon hemi-field paradigm. *Vision Res*, 41(1):97–102, 2001.

J.P. Culver, T. Durduran, D. Furuya, C. Cheung, J.H. Greenberg, and A.G. Yodh. Diffuse optical tomography of cerebral blood flow, oxygenation and metabolism in rat during focal ischemia. *J Cereb Blood Flow Metab*, 23:911–923, 2003.

J.P. Culver, A.M. Siegel, M.A. Franceschini, J.B. Mandeville, and D.A. Boas. Evidence that cerebral blood volume can provide brain activation maps with better spatial resolution than deoxygenated hemoglobin. *Neuroimage*, 27:947–959, 2005.

J.S. Damoiseaux, S.A.R.B. Rombouts, F. Barkhof, P. Scheltens, C.J. Stam, S.M. Smith, and C.F. Beckmann. Consistent resting-state networks across healthy subjects. *Proc Natl Acad Sci USA*, 103(37):13848–13853, 2006.

M. De Luca, C.F. Beckmann, N. De Stefano, P.M. Matthews, and S.M. Smith. fMRI resting state networks define distinct modes of long-distance interactions in the human brain. *Neuroimage*, 29:1359–1367, 2006.

H. Dehghani, B.W. Pogue, S.P. Poplack, and K.D. Paulsen. Multiwavelength three-dimensional near-infrared tomography of the breast: initial simulation, phantom, and clinical results. *Appl Opt*, 42:135–145, 2003.

H. Dehghani, B.R. White, B.W. Zeff, A. Tizzard, and J.P. Culver. Depth sensitivity and image reconstruction analysis of dense imaging arrays for mapping brain function with diffuse optical tomography. *Appl Opt*, 48:D137–D143, 2009.

M. D'Esposito, L. Y. Deouell, and A. Gazzaley. Alterations in the bold fMRI signal with ageing and disease: A challenge for neuroimaging. *Nat Rev Neurosci*, 4(11): 863–872, 2003.

A. Devor, A.K. Dunn, M.L. Andermann, I. Ulbert, D.A. Boas, and A.M. Dale. Coupling of total hemoglobin concentration, oxygenation, and neural activity in rat somatosensory cortex. *Neuron*, 39(2):353–9, 2003.

A. Devor, I. Ulbert, A.K. Dunn, S.N. Narayanan, S.R. Jones, M.L. Andermann, D.A. Boas, and A.M. Dale. Coulping of the cortical hemodynamic response to cortical and thalamic neuronal activity. *Proc Natl Acad Sci USA*, 102(10):3822–3827, 2005.

E.A. DeYoe, P. Bandettini, J. Neitz, D. Miller, and P. Winans. Functional magnetic resonance imaging (FMRI) of the human brain. *J Neurosci Methods*, 54:171–187, 1994.

E.A. DeYoe, G.J. Carman, P. Bandettini, S. Glickman, J. Wieser, R. Cox, D. Miller, and J. Neitz. Mapping striate and extrastriate visual areas in human cerebral cortex. *Proc Natl Acad Sci USA*, 93:2382–2386, 1996.

R.F. Dougherty, V.M. Koch, A.A. Brewer, B. Fischer, J. Modersitski, and B.A. Wandell. Visual field representations and locations of visual areas V1/2/3 in human visual cortex. *J Vision*, 3:586–598, 2003.

A.K. Dunn, A. Devor, H. Bolay, M.L. Andermann, M.A. Moskowitz, A.M. Dale, and D.A. Boas. Simultaneous imaging of total cerebral hemoglobin concentration, oxygenation, and blood flow during functional activation. *Opt Lett*, 28(1):28–30, 2003.

A.K. Dunn, A. Devor, A.M. Dale, and D.A. Boas. Spatial extent of oxygen metabolism and hemodynamic changes during functional activation of the rat somatosensory cortex. *Neuroimage*, 27:279–290, 2005.

C.E. Elwell, R. Springett, E. Hillman, and D.T. Delpy. Oscillations in cerebral haemodynamics - implications for functional activation studies. In A. Eke and D. Delpy, editors, *Oxygen Transport to Tissue XXI*, volume 471 of *Advances in Experimental Medicine and Biology*, pages 57–65. Kluwer Academic / Plenum Publishers, New York, 1999.

S.A. Engel, D.E. Rumelhart, B.A. Wandell, A.T. Lee, G.H. Glover, E.-J. Chichilnisky, and M.N. Shadlen. fMRI of human visual cortex. *Nature*, 369:525, 1994.

S.A. Engel, G.H. Glover, and B.A. Wandell. Retinotopic organization in human visual cortex and the spatial precision of functional MRI. *Cereb Cortex*, 7:181–192, 1997.

D.C. Van Essen, C.H. Anderson, and D.J. Felleman. Information processing in the primate visual system: an integrated systems perspective. *Science*, 255:419–423, 1992.

D.A. Fair, N.U.F. Dosenbach, J.A. Church, A.L. Cohen, S. Brahmbhatt, F.M. Miezin, D.M. Barch, M.E. Raichle, S.E. Petersen, and B.L. Schlaggar. Development of distinct control networks through segregation and integration. *Proc Natl Acad Sci USA*, 104(33):13507–13512, 2007.

D.A. Fair, A.L. Cohen, N.U.F. Dosenbach, J.A. Church, D.M. Miezin, F.M. Barch, M.E. Raichle, S.E. Petersen, and B.L. Schlaggar. The maturing architecture of the brain's default network. *Proc Natl Acad Sci USA*, 105(10):4028–4032, 2008.

M.D. Fox and M.E. Raichle. Spontaneous fluctuations in brain activity observed with functional magnetic resonance imaging. *Nat Rev Neurosci*, 8:700–711, 2007.

M.D. Fox, A.Z. Snyder, J.L. Vincent, M. Corbetta, D.C. Van Essen, and M.E. Raichle. The human brain is intrinsically organized into dynamic, anticorrelated functional networks. *Proc Natl Acad Sci USA*, 102(27):9673–9678, 2005.

P.T. Fox, F.M. Miezen, J.M. Allman, D.C. Van Essen, and M.E. Raichle. Retinotopic organization of the human visual cortex mapped with positron-emission tomography. *J Neurosci*, 7:913–922, 1987.

M.A. Franceschini, S. Fantini, J.J. Thompson, J.P. Culver, and D.A. Boas. Hemodynamic evoked response of the sensorimotor cortex measured non-invasively with near-infrared optical imaging. *Psychophysiology*, 40:548–560, 2003.

M.A. Franceschini, D.K. Joseph, T.J. Huppert, S.G. Diamond, and D.A. Boas. Diffuse optical imaging of the whole head. *J Biomed Opt*, 11(5):054007, 2006.

K.B.J. Franklin and G. Paxinos. *The Mouse Brain in Stereotactic Coordinates*. Academic Press, New York, Third edition, 2008.

P. Fransson, B. Skiold, S. Horsch, A. Nordell, M. Blennow, H. Lagercrantz, and U. Aden. Resting-state networks in the infant brain. *Proc Natl Acad Sci USA*, 104 (39):15531–15536, 2007.

P. Fransson, B. Skiöld, M. Engström, B. Hallberg, M. Mosskin, U. Åden, H. Lagercrantz, and M. Blennow. Spontaneous brain activity in the newborn brain during natural sleep–an fMRI study in infants born at full term. *Pediatr Res*, 66(3):301–305, 2009.

N. Fujiwara, K. Sakatani, Y. Katayama, Y. Murata, T. Hoshino, C. Fukaya, and T. Yamamoto. Evoked-cerebral blood oxygenation changes in false-negative activations in BOLD contrast functional MRI of patients with brain tumors. *Neuroimage*, 21(4):1464–1471, 2004.

D.D. Garrett, N. Kovacevic, A.R. McIntosh, and C.L. Grady. Blood oxygen level-dependent signal variability is more than just noise. *J Neurosci*, 30(14):4914–4921, 2010.

A.P. Gibson, T. Austin, N.L. Everdell, M. Schweiger, S.R. Arridge, J.H. Meek, J.S. Wyatt, D.T. Delpy, and J.C. Hebden. Three-dimensional whole-head optical tomography of passive motor evoked responses in the neonate. *Neuroimage*, 30(2): 521–528, 2006.

N.M. Gregg, B.R. White, B.W. Zeff, A.J. Berger, and J.P. Culver. Brain specificity of diffuse optical imaging: improvements from superficial signal regression and tomography. *Front Neuroenerg*, 2:14:1–8, 2010.

M.D. Greicius, G. Srivastava, A.L. Reiss, and V. Menon. Default-mode network activity distinguishes Alzheimer's disease from healthy aging: Evidence from functional MRI. *Proc Natl Acad Sci USA*, 101(13):4637–4642, 2004.

M.D. Greicius, B.H. Flores, V. Menon, G.H. Glover, H.B. Solvason, H. Kenna, A.L. Reiss, and A.F. Schatzberg. Resting-state functional connectivity in major depression: Abnormally increased contributions from subgenual cingulate cortex and thalamus. *Biol Psychiatry*, 62(5):426–437, 2007.

A. Grinvald, E. Lieke, R.D. Frostig, C.D. Gilbert, and T.N. Wiesel. Functional architecture of cortex revealed by optical imaging of intrinsic signals. *Nature*, 324 (6095):361–4, 1986.

B.J. He, A.Z. Snyder, J.M. Zempel, M.D. Smyth, and M.E. Raichle. Electrophysiological correlates of the brain's intrinsic large-scale functional architecture. *Proc Natl Acad Sci USA*, 105(41):16039–16044, 2008.

J.C. Hebden, A. Gibson, R.M. Yusof, N. Everdell, E.M.C. Hillman, D.T. Delpy, S.R. Arridge, T. Austin, J.H. Meek, and J.S. Wyatt. Three-dimensional optical tomography of the premature infant brain. *Phys Med Biol*, 47(23):4155–4166, 2002.

D.J. Heeger and D. Ress. What does fMRI tell us about neuronal activity? *Nat Rev Neurosci*, 3:142–151, 2002.

J. Heiskala, P. Hiltunen, and I. Nissila. Significance of background optical properties, time-resolved information and optode arrangement in diffuse optical imaging of term neonates. *Phys Med Biol*, 54:535–554, 2009.

F. Homae, H. Watanabe, T. Otobe, T. Nakano, T. Go, Y. Konishi, and G. Taga. Development of global cortical networks in early infancy. *J Neurosci*, 30(14):4877–4882, 2010.

R.M. Hutchinson, S.M. Mirasattari, C.K. Jones, J.S. Gati, and L.S. Leung. Functional networks in the anesthetized rat brain revealed by independent component analysis of resting-state fMRI. *J Neurophysiol*, 103:3398–3406, 2010.

G. Jasdzewski, G. Strangman, J. Wagner, K.K. Kwong, R.A. Poldrack, and D.A. Boas. Differences in the hemodynamic response to event-related motor and visual paradigms as measured by near-infrared spectroscopy. *Neuroimage*, 20(1):479–488, 2003.

F.F. Jöbsis. Nonivasive, infrared monitoring of cerebral and myocardial oxygen sufficiency and circulatory parameters. *Science*, 198:1264–1267, 1977.

D.K. Joseph, T.J. Huppert, M.A. Franceschini, and D.A. Boas. Diffuse optical tomography system to image brain activation with improved spatial resolution and validation with functional magnetic resonance imaging. *Appl Opt*, 45:8142–8151, 2006.

A.C. Kak and M. Slaney. *Principles of Computerized Tomographic Imaging.* IEEE Press, New York, 1988.

V.A. Kalatsky and M.P. Stryker. New paradigm for optical imaging: Temporally encoded maps of intrinsic signal. *Neuron*, 38:529–545, 2003.

H.C. Kang, E.D. Burgund, H.M. Lugar, S.E. Petersen, and B.L. Schlaggar. Comparison of functional activation foci in children and adults using a common stereotactic space. *Neuroimage*, 19:16–28, 2003.

T. Karen, G. Morren, D. Haensse, A.S. Bauschatz, H.U. Bucher, and M. Wolf. Hemodynamic response to visual stimulation in newborn infants using functional near-infrared spectroscopy. *Hum Brain Mapp*, 29:453–460, 2008.

T. Katura, N. Tanaka, A. Obata, H. Sato, and A. Maki. Quantitative evaluation of interrelations between spontaneous low-frequency oscillations in cerebral hemodynamics and systemic cardiovascular dynamics. *Neuroimage*, 31:1593–1600, 2006.

T. Kenet, D. Bibitchkov, M. Tsodyks, A. Grinvald, and A. Arieli. Spontaneously emerging cortical representation of visual attributes. *Nature*, 425:954–956, 2003.

V. Kiviniemi. Endogenous brain fluctuations and diagnostic imaging. *Hum Brain Mapp*, 29:810–817, 2008.

B. Larroque, P.-Y. Ancel, S. Marret, L. Marchand, M. André, C. Arnaud, V. Pierrat, J. Roz, J. Messer, G. Thiriez, A. Burguet, J.-C. Picaud, G. Bréart, and M. Kaminski. Neurodevelopmental disabilities and special care of 5-year-old children born before 33 weeks of gestation (the EPIPAGE study): a longitudinal cohort study. *Lancet*, 371:813–820, 2008.

B. Latal. Prediction of neurodevelopmental outcome after preterm birth. *Ped Neurol*, 10:413–419, 2009.

S.M. Liao, N.M. Gregg, B.R. White, B.W. Zeff, K.A. Bjerkaas, T.E. Inder, and J.P. Culver. Neonatal hemodynamic response to visual cortex activity: A high-density NIRS study. *J Biomedi Opt*, 15(2):026010, 2010.

U. Lindauer, G. Royl, C. Leithner, M. Kühl, L. Gold, J. Gethmann, M. Kohl-Bareis, A. Villringer, and U. Dirnagl. No evidence for early decrease in blood oxygenation in rat whisker cortex in response to functional activation. *Neuroimage*, 13(6), 2001.

M.J. Lowe, B.J. Mock, and J.A. Sorensonm. Functional connectivity in single and multislice echoplanar imaging using resting-state fluctuations. *Neuroimage*, 7:119–132, 1998.

T.E. Lund, K.H. Madsen, K. Sidaros, W.-L. Luo, and T.E. Nichols. Non-white noise in fMRI: Does modelling have an impact? *Neuroimage*, 29(1):54–66, 2006.

J. Markham, B.R. White, B.W. Zeff, and J.P. Culver. Blind identification of evoked human brain activity with independent component analysis of optical data. *Hum Brain Mapp*, 30(8):2382–2392, 2009.

N. Marlow, D. Wolke, M.A. Bracewell, and M. Samara. Neurologic and developmental disability at six years of age after extremely preterm birth. *N Eng J Med*, 352(1): 9–19, 2005.

C. Martin, J. Martindale, J. Berwick, and J. Mayhew. Investigating neural-hemodynamic coupling and the hemodynamic response function in the awake rat. *Neuroimage*, 32:33–48, 2006.

J.H. Meek, M. Firbank, C.E. Elwell, J. Atkinson, O. Braddick, and J.S. Wyatt. Regional hemodynamic responses to visual stimulation in awake infants. *Pediatr Res*, 43(6):840–3, 1998.

L.R. Ment, D. Hirtz, and P.S. Hüppi. Imaging biomarkers of outcome in the developing preterm brain. *Lancet Neurol*, 8:1042–1055, 2009.

T. Obata, T.T. Liu, K.L. Miller, W.M. Luh, E.C. Wong, L.R. Frank, and R.B. Buxton. Discrepancies between BOLD and flow dynamics in primary and supplementary motor areas: application of the balloon model to the interpretation of BOLD transients. *Neuroimage*, 21(1):144–153, 2004.

H. Obrig and A. Villringer. Beyond the visible–imaging the human brain with light. *J Cereb Blood Flow Metab*, 23(1):1–18, 2003.

H. Obrig, M. Neufang, R. Wenzel, M. Kohl, J. Steinbrink, K. Einhaupl, and A. Villringer. Spontaneous low frequency oscillations of cerebral hemodynamics and metabolism in human adults. *Neuroimage*, 12(6), 2000.

S. Ogawa, Lee T.M., A.S. Nayak, and Glenn P. Oxygenation-sensitive contrast in magnetic resonance imaging of rodent brain at high magnetic fields. *Magn Reson Med*, 14:68–78, 1990.

C.P. Pawela, B.B. Biswal, Y.R. Cho, D.S. Kao, R. Li, S.R. Jones, M.L. Schulte, H.S. Matloub, A.G. Hudetz, and J.S. Hyde. Resting-state functional connectivity of the rat brain. *Magn Reson Med*, 59:1021–1029, 2008.

C.P. Pawela, B.B. Biswal, A.G. Hudetz, R. Li, S.R. Jones, Y.R. Cho, H.S. Matloub, and J.S. Hyde. Interhemispheric neuroplasticity following limb deafferentiation detected by resting-state functional connectivity magnetic resonance imaging (fcMRI) and functional magnetic resonance imaging (fMRI). *Neuroimage*, 49:2467–2478, 2010.

M.M. Plichta, M.J. Herrmann, C.G. Baehne, A.-C. Ehlis, M.M. Richter, P. Pauli, and A.J. Fallgatter. Event-related functional near-infrared spectroscopy (fNIRS): Are the measurements reliable? *Neuroimage*, 31:116–124, 2006.

Y. Pole. Evolution of the pulse oximeter. *Int Congr Ser*, 1242:137–144, 2002.

M.E. Raichle and M.A. Mintun. Brain work and brain imaging. *Ann Rev of Neurosci*, 29:449–476, 2006.

M. Reinhard, E. Wehrle-Wieland, D. Grabiak, M. Roth, B. Guschlbauer, J. Timmer, C. Weiller, and A. Hetzel. Oscillatory cerebral hemodynamics–the macro- vs. the microvascular level. *J Neurol Sci*, 250(1-2):103–109, 2006.

A.B. Rowley, S.J. Payne, I. Tachtsidis, M.J. Ebden, J.P. Whiteley, D.J. Gavaghan, L. Tarassenko, M. Smith, C.E. Elwell, and T.D. Delpy. Synchronization between arterial blood pressure and cerebral oxyhaemoglobin concentration investigated by wavelet cross-correlation. *Physiol Meas*, 28:161–173, 2007.

R.B. Saager and A.J. Berger. Direct characterization and removal of interfering absorption trends in two-layer turbid media. *J Opt Soc Am A*, 22:1874–1882, 2005.

R.B. Saager and A.J. Berger. Measurement of layer-like hemodynamic trends in scalp and cortex: implications for physiological baseline suppression in functional near-infrared spectroscopy. *J Biomed Opt*, 13:034017, 2008.

M.L. Schroeter, M.M. Bucheler, K. Muller, K. Uludag, H. Obrig, G. Lohmann, M. Tittgemeyer, A. Villringer, and D.Y. von Cramon. Towards a standard analysis for functional near-infrared imaging. *Neuroimage*, 21(1):283–290, 2004.

M.L. Schroeter, M.M. Bucheler, C. Preul, R. Scheid, O. Schmiedel, T. Guthke, and D.Y. von Cramon. Spontaneous slow hemodynamic oscillations are impaired in cerebral microangiopathy. *J Cereb Blood Flow Metab*, 25:1675–1684, 2005.

W.W. Seeley, R.K. Crawford, J. Zhou, B.L. Miller, and M.D. Greicius. Neurodegenerative diseases target large-scale human brain networks. *Neuron*, 62:42–52, 2009.

J. Selb, M.A. Franceschini, A.G. Sorensen, and D.A. Boas. Improved sensitivity to cerebral hemodynamics during brain activation with a time-gated optical system: analytical model and experimental validation. *J Biomed Opt*, 10(1):011013, 2005.

M.I. Sereno, C.T. McDonald, and J.M. Allman. Analysis of retinotopic maps in extrastriate cortex. *Cereb Cortex*, 6:601–620, 1994.

M.I. Sereno, A.M. Dale, J.B. Reppas, K.K. Kwong, J.W. Belliveau, T.J. Brady, B.R. Rosen, and R.B.H. Tootell. Borders of multiple visual areas in humans revealed by functional magnetic-resonance-imaging. *Science*, 268(5212):889–893, 1995.

S.A. Sheth, M. Nemoto, M. Guiou, M. Walker, N. Pouratian, N. Hageman, and A.W. Toga. Columnar specificity of microvascular oxygenation and volume responses: Implications for functional brain mapping. *J Neurosci*, 24(3):634–641, 2004.

K. Shmueli, P. van Gelderen, J.A. de Zwart, S.G. Horovitz, M. Fukunaga, J.M. Jansma, and J.H. Duyn. Low-frequency fluctuations in the cardiac rate as a source of variance in the resting-state fMRI BOLD signal. *Neuroimage*, 38:306–320, 2007.

C.D. Smyser, T.E. Inder, J.S. Shimony, J.E. Hill, A.J. Degnan, A.Z. Snyder, and J.J. Neil. Longitudinal analysis of neural network development in preterm infants. *Cereb Cortex*, In Press, 2010.

J. Steinbrink, H. Wabnitz, H. Obrig, A. Villringer, and H. Rinneberg. Determining changes in NIR absorption using a layered model of the human head. *Phys Med Biol*, 46(3):879–896, 2001.

S.S. Stensaas, D.K. Eddington, and W.H. Dobelle. The topography and variability of the primary visual cortex in man. *J Neurosurg*, 40:747–755, 1974.

G. Strangman, M.A. Franceschini, and D.A. Boas. Factors affecting the accuracy of near-infrared spectroscopy concentration calculations for focal changes in oxygenation parameters. *Neuroimage*, 18:865879, 2003.

G. Taga, K. Asakawa, A. Maki, Y. Konishi, and H. Koizumi. Brain imaging in awake infants by near-infrared optical topography. *Proc Natl Acad Sci USA*, 100(19): 10722–10727, 2003.

R.B.H. Tootell and N.K. Hadjikhani. Where is 'dorsal V4' in human visual cortex? *Cereb Cortex*, 11:298–311, 2001.

R.B.H. Tootell, J.D. Mendola, N.K. Hadjikhani, P.J. Ledden, A.K. Liu, J.B. Reppas, M.I. Sereno, and A.M. Dale. Functional analysis of V3A and related areas in human visual cortex. *J Neurosci*, 17:7060–7078, 1997.

R.B.H. Tootell, N.K. Hadjikhani, W. Vanduffel, A.K. Liu, J.D. Mendola, M.I. Sereno, and A.M. Dale. Functional analysis of primary visual cortex (V1) in humans. *Proc Natl Acad Sci USA*, 95:811–817, 1998.

V.Y. Toronov, X. Zhang, and A.G. Webb. A spatial and temporal comparison of hemodynamic signals measured using optical and functional magnetic resonance imaging during activation in the human primary visual cortex. *Neuroimage*, 34: 1136–1148, 2007.

D.Y. Ts'o, R.D. Frostig, E.E. Lieke, and A. Grinvald. Functional organization of primate visual cortex revealed by high resolution optical imaging. *Science*, 249 (4967):417–20, 1990.

D.C. Van Essen, H.A. Drury, J. Dickson, J. Harwell, D. Hanlon, and C.H. Anderson. An integrated software suite for surface-based analyses of cerebral cortex. *J Am Med Inform Assoc*, 8(5):443–459, 2001.

A. Vanhaudenhuyse, Q. Noirhomme, L.J.-F. Tshibanda, M.-A. Bruno, P. Boveroux, C. Schnakers, A. Soddu, V. Perlbarg, D. Ledoux, J.F. Brichant, G. Moonen, P. Maquet, M.D. Greicius, S. Laureys, and M. Boly. Default network connectivity reflects the level of consciousness in non-communicative brain-damaged patients. *Brain*, 133:161–171, 2010.

A. Villringer, J. Planck, C. Hock, L. Schleinkofer, and U. Dirnagl. Near infrared spectroscopy (NIRS): A new tool to study hemodynamic changes during activation of brain function in human adults. *Neurosci Lett*, 154:101–104, 1993.

J.L. Vincent, G.H. Patel, M.D. Fox, A.Z. Snyder, J.T. Baker, D.C. Van Essen, J.M. Zempel, L.H. Synder, M. Corbetta, and M.E. Raichle. Intrinsic functional architecture in the anaesthetized monkey brain. *Nature*, 447:83–86, 2007.

B.A. Wandell and A.R. Wade. Functional imaging of the visual pathways. *Neurol Clin N Am*, 21:417–443, 2003.

B.A. Wandell, A.A. Brewer, and R.F. Dougherty. Visual field map clusters in human cortex. *Phil Trans R Soc B*, 360(1456):693–707, 2005.

L.V. Wang and W. Hsin-I. *Biomedical Optics: Principles and Imaging.* John Wiley & Sons, 2007.

J. Warnking, M. Dojat, A. Gurin-Dugu, C. Delon-Martin, S. Olympieff, N. Richard, A. Chhikian, and C. Segebarth. fMRI retinotopic mapping–step by step. *Neuroimage*, 17:1665–1683, 2002.

B.R. White and J.P. Culver. Phase-encoded retinotopy as an evaluation of diffuse optical neuroimaging. *Neuroimage*, 49:568–577, 2010a.

B.R. White and J.P. Culver. Quantitative evaluation of high-density diffuse optical tomography: *in vivo* resolution and mapping performance. *J Biomed Opt*, 15: 026006, 2010b.

B.R. White, A.Z. Snyder, A.L. Cohen, S.E. Petersen, M.E. Raichle, B.L. Schlaggar, and J.P. Culver. Resting-state functional connectivity in the human brain revealed with diffuse optical tomography. *Neuroimage*, 47:148–156, 2009.

M. Wolf, U. Wolf, V.Y. Toronov, A. Michalos, L.A. Paunescu, J.H. Choi, and E. Gratton. Different time evolution of oxyhemoglobin and deoxyhemoglobin concentration changes in the visual and motor cortices during functional stimulation: A near-infrared spectroscopy study. *Neuroimage*, 16(3):704–712, 2002.

T.A. Woolsey, C.M. Rovainen, S.B. Cox, M.H. Henegar, G.E. Liang, D. Liu, Y.E. Moskalenko, J. Sui, and L. Wei. Neuronal units linked to microvascular modules in cerebral cortex: response elements for imaging the brain. *Cereb Cortex*, 6(5): 647–60, 1996.

G.R. Wylie, H. Graber, G.T. Voelbel, A.D. Kohl, J. DeLuca, Y. Pei, Y. Xu, and R.L. Barbour. Using co-variation in the Hb signal to detect visual activation: A near infrared spectroscopy study. *Neuroimage*, 47:473–481, 2009.

A.G. Yodh and D.A. Boas. Functional imaging with diffusing light. In T. Vo-Dinh, editor, *Biomedical Photonics*, volume 21, pages 21–1 – 21–45. CRC Press, Boca Raton, FL, 2003.

B.W. Zeff, B.R. White, H. Dehghani, B.L. Schlaggar, and J.P. Culver. Retinotopic mapping of adult human visual cortex with high-density diffuse optical tomography. *Proc Natl Acad Sci USA*, 104:12169–9612174, 2007.

F. Zhao, T. Zhao, L. Zhou, Q. Wu, and X. Hu. BOLD study of stimulation-induced neural activity and resting-state connectivity in medetomidine-sedated rat. *Neuroimage*, 39:248–260, 2008.